



Electronic Properties of Graphene Functionalized with 2D Molecular Assemblies

Mali Zhao

► To cite this version:

Mali Zhao. Electronic Properties of Graphene Functionalized with 2D Molecular Assemblies. Chemical Physics [physics.chem-ph]. Université Paris Saclay (COmUE), 2017. English. NNT : 2017SACLS013 . tel-03527125

HAL Id: tel-03527125

<https://theses.hal.science/tel-03527125>

Submitted on 15 Jan 2022

HAL is a multi-disciplinary open access archive for the deposit and dissemination of scientific research documents, whether they are published or not. The documents may come from teaching and research institutions in France or abroad, or from public or private research centers.

L'archive ouverte pluridisciplinaire **HAL**, est destinée au dépôt et à la diffusion de documents scientifiques de niveau recherche, publiés ou non, émanant des établissements d'enseignement et de recherche français ou étrangers, des laboratoires publics ou privés.

NNT : 2017SACLS013

**THESE DE DOCTORAT
DE
L'UNIVERSITE PARIS-SACLAY
PREPAREE A
L'UNIVERSITE PARIS-SUD**

**ECOLE DOCTORALE N°572 : EDOM
Ecole Doctorale Ondes et Matière**

Nanophysique

Par

Mlle Mali Zhao

Electronic Properties of Graphene Functionalized with 2D Molecular Assemblies

Thèse présentée et soutenue à Orsay, le 13 Janvier 2017 :

Composition du Jury :

Mme Sophie Gueron	Directrice de Recherche, Laboratoire de Physique des Solides (LPS), Orsay	Présidente
M. Mathieu Abel	Professeur, Institut Materiaux Microélectronique Nanosciences de Provence (IM2NP), Marseille	Rapporteur
M. Xavier Bouju	Directeur de Recherche, Centre d'Élaboration de Matériaux et d'Etudes Structurales (CEMES/CNRS), Toulouse	Rapporteur
M. Olivier Pluchery	Maître de Conférence, Université Pierre et Marie Curie (UPMC), Paris	Examinateur
M. Andrew Mayne	Directeur de Recherche, Institut des Sciences Moléculaires d'Orsay (ISMO), Orsay	Directeur de thèse

Electronic Properties of Graphene Functionalized with 2D Molecular Assemblies

Abstract:

This thesis presents the investigation of the self-assembly of two-dimensional networks of organic molecules on graphene, as well as the electronic coupling between molecules and graphene by means of Scanning Tunneling Microscopy (STM), Scanning Tunneling Spectroscopy (STS), and Density Functional Theory (DFT) calculations.

The high electron mobility in graphene makes it an ideal material to transmit the injected spins in spin-field effect transistors. However, the spin-orbit interaction in graphene is too weak to control the spin precession from source to drain. To enhance the spin-orbit interaction in graphene, and induce a magnetic moment, organic molecules containing a metal ion (metal-porphyrins, metal-phthalocyanines) were proposed to functionalize the graphene; they have a robust structure, tunable charge and spin properties. A previous study showed that the magnetic moment could be induced by charge transfer between the molecules and graphene, therefore, it is crucial to study the electronic coupling between organic molecules and graphene.

In this thesis, both electron-doped and neutral graphene were prepared by sublimation of Si atoms from the Si-and C-terminated SiC substrates, respectively. Three molecules carrying different spin information were studied in an effort to functionalize graphene: Ni-phthalocyanine (NiPc), Pt-tetraphenylporphyrin ($\text{PtTPP}(\text{CO}_2\text{Me})_4$) and Fe-tetraphenylporphyrin chloride ($\text{Fe}(\text{TPP})\text{Cl}$). The results are summarized below:

On the Si-terminated SiC substrate, the number of graphene layers can be precisely controlled. The monolayer graphene shows a honeycomb lattice, while bilayer graphene exhibits a triangular lattice because of the Bernal stacking of the graphene planes. The buffer layer between the graphene and SiC substrate induces the electron-doping of graphene. On the C-terminated SiC substrate, multilayer graphene was grown and turbostratic growth behaviour was observed. Graphene terraces with different Moiré patterns are separated by folded sp₂ hybridized carbon pleats. The Moiré pattern comes from the azimuthal disorder of the top few graphene layers. The buffer layer does not exist between the graphene and SiC substrate, which maintains the graphene Dirac point at the Fermi level (Chapter 3).

The first molecule used in our experiment is NiPc. The Ni²⁺ ion has a 3d8 electron configuration, giving a spin-state of zero. The self-assembly and electronic properties of NiPc molecules on monolayer graphene/6H-SiC(0001) substrate were studied. The single layer of NiPc molecules formed a close-packed square lattice on graphene. In the STM topographies, each molecule is composed of four lobes with a depression in the center. The molecular orientations depend on the molecule-molecule interaction, while the molecular lattice direction relies on the graphene symmetry. In the STS measurements, the NiPc molecular orbitals shift with the variation of the tip-sample separation indicating the capacitance nature of the NiPc molecular layer/graphene interface. The DFT calculation confirms that the electronic coupling between NiPc molecules and neutral graphene occurs via the van der Waals force, and that the charge transfer is close to zero. For the molecules on n-doped graphene/ SiC (0001), there is a small charge transfer from graphene to NiPc molecules according to the energy level alignment at the molecule/graphene interface (Chapter 4).

The second molecule is PtTPP(CO₂Me)₄. The Pt²⁺ ion also shows a 5d8 electron configuration with a spin state of zero. However, the Pt atom is much heavier than Ni, which should increase the spin-orbit interaction. The topography and electronic properties of PtTPP(CO₂Me)₄ molecules were studied on both graphene/ SiC(0001)

and graphene/ SiC(000-1). Both single and double layer molecules form self-assembled almost square lattices on graphene. The lattice direction depends on the molecular symmetry, the graphene terrace direction, and the graphene symmetry. For the double-layer PtTPP(CO₂Me)₄ molecular network on graphene, the evolution of molecular conformations during thermal treatment indicates a weak out-of plane molecule-molecule interaction. At the molecule/ graphene interface, there is a small charge transfer from graphene (both neutral and n-doped graphene) to the PtTPP(CO₂Me)₄ molecular layer, indicating a stronger electronic coupling between PtTPP(CO₂Me)₄ molecules and graphene than that between NiPc and graphene (Chapter 5).

The third molecule is Fe(TPP)Cl. The Fe³⁺ in Fe(TPP)Cl is stable in a high spin state (S=5/2). The topography and electronic properties of molecules were studied on both graphene/ SiC(0001) and graphene/ SiC(000-1). After the deposition of Fe(TPP)Cl molecules on graphene at 195°C, the Fe(TPP)Cl molecules transformed to FeTPP molecules following the dissociation of the Cl atoms. FeTPP molecules also form a well-ordered almost square lattice on graphene. The double molecular layers show an offset face-to-face stacking mode, and the intermolecular interactions are dominated by the van der Waals force. Small aggregates containing four molecules were observed on top of the molecular network. These indicate that the in-plane molecule-molecule interaction is stronger than the out-of-plane intermolecular interaction. In addition, the adsorbed four-molecule aggregates are rotated 50 ° with respect to the molecular lattice directions, due to molecular polarization induced by the non-equivalent intermolecular interactions in the molecular aggregates compared to the molecular network. The STS measured HOMO-LUMO gap of FeTPP molecules on n-doped graphene lies between the HOMO-LUMO gaps of isolated FeTPP and isolated FeTPP⁻¹ molecules in the gas phase, suggesting a charge transfer from n-doped graphene to the FeTPP molecules. In addition, the stable FeTPP molecular domain and graphene terrace indicates that the electronic coupling between

the FeTPP molecules and graphene is stronger than that between PtTPP or NiPc molecules and graphene (Chapter 6).

The studies of the organic molecules with different spin information on the graphene shed some light on the electronic properties of organometallic molecules/graphene interfaces in future spintronic devices.

Propriétés Électroniques du Graphène Fonctionnalisé par des Assemblages Moléculaires Bidimensionnels

Résumé:

Cette thèse présente les études de l'auto-assemblage d'un réseau bidimensionnel de molécules organiques sur le graphène, ainsi que le couplage électronique entre les molécules et le graphène par Microscope à effet tunnel (STM), Spectroscopie par effet tunnel (STS) et calculs de théorie de la densité fonctionnelle (DFT).

En raison de la mobilité électronique élevée et de l'interaction spin-orbite faible, le graphène peut être utilisé dans le transistor à effet de champ de spin pour transmettre les spins injectés. Par contre, l'interaction spin-orbite dans le graphène est trop faible pour contrôler la précession de spin de la source au drain. Afin de renforcer l'interaction spin-orbite dans le graphène, et d'induire le moment magnétique, on a proposé de fonctionnaliser le graphène par molécules organiques avec un ion métallique (métal-porphyrine, métal-phtalocyanines) en raison de leur structure robuste ainsi que de la charge ajustable et de la quantité de spin propriétés. Une étude antérieure a indiqué que le moment magnétique pouvait être induit par le transfert de charge entre les molécules et le graphène, donc, il est très important d'étudier le couplage électrique entre les molécules organiques et le graphène.

Dans cette thèse, le graphène neutre ou dopé par des électrons a été préparé par la sublimation des atomes de Si des substrats de SiC terminés C ou Si, respectivement. Trois molécules portant différentes informations de spin ont été étudiées dans le but de fonctionnaliser le graphène: la Ni-Phtalocyanine (NiPc), la Pt-Tétraphénylporphyrine ($\text{PtTPP}(\text{CO}_2\text{Me})_4$) et le chlorure de Fe-Tétraphénolporphyrine (Fe (TPP) Cl). Les résultats sont résumés ci-dessous:

Sur le substrat de SiC terminé Si, le nombre de couches de graphène peut être contrôlé avec précision. La monocouche de graphène présente un réseau en nid d'abeille, alors que la bicouche de graphène présente un réseau triangulaire en raison de l'empilement Bernal entre les plans de graphène. La couche tampon entre le graphène et le substrat SiC induit le dopage électronique du graphène.

Sur le substrat de SiC terminé en C, le graphène multicouches a été fabriqué et un comportement de croissance turbostratique a été observé. Les terrasses de graphène à motifs de Moiré différents sont séparées par des plis de carbone hybrides sp₂ plissés. Le motif de Moiré provient du désordre azimuthal des couches de graphène supérieures. La couche tampon n'existe pas entre le graphène et le substrat de SiC, qui maintient le point de Dirac au graphène au niveau de Fermi (Chapitre 3).

La première molécule utilisée dans notre expérience est la NiPc. L'ion Ni²⁺ a une configuration électron 3d8, donnant un état de spin de zéro. L'auto-assemblage et les propriétés électroniques des molécules de NiPc en graphène monocouche/ substrat 6H-SiC(0001) ont été étudiés. La couche unique de molécules de NiPc forme un réseau compact sur le graphène et dans les topographies STM chaque molécule est composée de quatre lobes avec une dépression au centre. Les orientations moléculaires dépendent de l'interaction molécule-molécule, tandis que la direction du réseau moléculaire repose sur la symétrie du graphène. Dans les mesures STS, le déplacement des orbitales moléculaires de NiPc varie avec la séparation pointe-échantillon indiquant un comportement capacitif de l'interface couche de NiPc/graphène. Le calcul de DFT confirme que le couplage électronique entre les molécules NiPc et le graphène neutre s'opère via la force de van der Waals, et que le transfert de charge est proche de zéro. Pour les molécules sur graphène/ SiC(0001), il y a un petit transfert de charge du graphène vers les molécules de NiPc en fonction de l'alignement du niveau d'énergie à l'interface entre la molécule et le graphène (Chapitre 4).

La seconde molécule est la PtTPP(CO₂Me)₄. L'ion Pt²⁺ montre également une configuration électronique 5d8 avec un état de spin de zéro. Cependant, l'atome de Pt est beaucoup plus lourd que celui de Ni, ce qui devrait augmenter l'interaction spin-orbite. Les topographies STM et les propriétés électroniques des molécules de PtTPP(CO₂Me)₄ ont été étudiées à la fois sur le graphène/ SiC(0001) et le graphène/ SiC(000-1). Les molécules s'adsorbent en simple ou double couche et forment des réseaux quasi-carrés auto-assemblés sur du graphène. La direction du réseau dépend de la symétrie moléculaire, de la direction de la terrasse du graphène et de la symétrie du graphène. Pour le réseau moléculaire à double couche de PtTPP(CO₂Me)₄ sur le graphène, l'évolution des conformations moléculaires pendant le traitement thermique indique une faible interaction molécule-molécule hors plan. À l'interface molécule/graphène, il y a un petit transfert de charge à partir du graphène (graphène neutre et n-dopé) vers la couche moléculaire PtTPP(CO₂Me)₄, indiquant un couplage électronique plus fort entre les molécules PtTPP(CO₂Me)₄ et graphène que celui entre NiPc et graphène (Chapitre 5).

La troisième molécule est la Fe(TPP)Cl. Le Fe³⁺ dans Fe(TPP)Cl est stable avec un état de spin élevé ($S = 5/2$). Les topographies STM et les propriétés électroniques des molécules ont été étudiées à la fois sur le graphène/ SiC (0001) et le graphène/ SiC (000-1). Après le dépôt de molécules de Fe(TPP)Cl sur le graphène à 195 °C, les molécules de Fe(TPP)Cl se sont transformées en molécules de FeTPP suite à la dissociation des atomes de Cl. Les molécules de FeTPP forment également un réseau bien ordonné sur le graphène. Les couches doubles moléculaires montrent un mode d'empilement face à face décalé et les interactions intermoléculaires sont dominées par la force de van der Waals. Les agrégats adsorbés au-dessus du réseau moléculaire comportant quatre molécules indiquent que l'interaction molécule-molécule dans le plan est plus forte que l'interaction intermoléculaire hors plan. En outre, les agrégats à quatre molécules adsorbées ont un angle de rotation de 50 ° par rapport aux directions du réseau moléculaire, en raison de la polarisation moléculaire induite par les

interactions intermoléculaires non équivalentes dans les agrégats moléculaires et le réseau moléculaire. L'intervalle HOMO-LUMO mesuré par STS des molécules de FeTPP sur le graphène n-dopé se situe entre les intervalles HOMO-LUMO de FeTPP et de FeTPP^{-1} en phase gazeuse, ce qui suggère un transfert de charges à partir de graphène dopé n vers des molécules de FeTPP. De plus, la limite stable entre le domaine moléculaire de FeTPP et la terrasse de graphène indiquent que le couplage électronique entre les molécules de FeTPP et le graphène est plus fort que celui entre les molécules de PtTPP ou de NiPc et le graphène (Chapitre 6).

Les études des molécules organiques avec différentes informations de spin sur le graphène apportent de la lumière sur l'influence d'interfaces organométalliques / graphène dans des dispositifs spintroniques futurs.

Acknowledgments

I am really thankful to my supervisor, Dr. Andrew Mayne, for giving me the opportunity to work in the Molecular Nanoscience group and I really appreciate for his excellent supervision. He is very patient and conscientious, he taught me from the basic operations of the experimental set-up until I could complete the experiments independently. The discussion of the experimental results with him was always very inspiring, I understand more about the complex physics hide behind the results. He is also very nice and easygoing in daily life. It is the first time that I work and live aboard, the culture and language difference makes it difficult for me to adapt to the new life here in the first year. He helped me a lot on looking for the residence, completing the registration and so on, I can fit myself in the new atmosphere easily.

I want to express my gratitude to our collaborators, Prof. Philippe Sonnet (IS2M, Mulouse), Dr. Eric Duverger (FEMTO-ST, Besançon) and Dr. Yannick Dappe (CEA, Gif sur Yvette) for the DFT calculations.

I would especially like to thank Dr. Gérald Dujardin for the fruitful discussions of my experimental results. I also would like to thank Dr. Eric Le Moal, Dr. Séverine Le Moal, Prof. Hamid Oughaddou, Mlle Hanna Enriquez for their help on the operation of LT-STM. Their passion and serious attitude on research influence me greatly.

I am thankful to Prof. Damien Riedel for the help on the understanding of the physics. I also would like to thank Dr. Elizabeth Boer-Duchemin, and Dr. Georges Raseev, it is very pleasant to discuss science and I enjoy the talking with them in the lunch time.

I would like to thank all the members in my thesis committee: Dr. Xavier Bouju (CEMES-CNRS, Toulouse), Dr. Mathieu Abel (IM2NP, Marseille), Dr. Pluchery

Olivier (UPMC, Paris) and Dr. GUÉRON Sophie (LPS, Orsay) for kindly agreeing to be reporters and reviewers of this thesis.

All the students in the group are easygoing and get along with each other well. I like the international harmonious environment here. Especially, I want to thank Dr. Rachid Tchalala, he shared his research experience and many experimental skills with me, generously. I also want to thank Master student Faisal Almarzouqi, I will never forget the surprise birthday cake he prepared and the small but warm birthday party he organized for me in the group.

I want to take this opportunity to thank my dear parents and my brothers for their constant understanding and supporting. I am lucky to meet my boyfriend in romantic Paris, who fully understand me and support me unconditionally. We are also good friends, I cannot complete my thesis smoothly without him.

Last but not least, I would like to thank China Scholarship Council to provide the financial support for my three-year PhD thesis in France.

Table of Contents

Abstract.....	I
R ésum é.....	V
Acknowledgments	IX
Chapter 1 Introduction.....	1
1.1 The Development of Electronic Technology	2
1.2 The Development of Molecular Devices	2
1.3 Spin Field-Effect Transistor	4
1.3.1 Spin-FET based on Graphene	5
1.3.2 The Functionalization of Graphene	6
1.4 The Self-Assembled Organic Molecules on Surface	8
1.4.1 Molecular Self-Assembly	8
1.4.2 Energy Level Alignment at the Molecule/ Substrate Interface	9
1.5 The Project and My Subject	12
1.6 Bibliography.....	13
Chapter 2 Experimental Techniques and Methods.....	21
2.1 Scanning Tunneling Microscope (STM).....	22
2.1.1 Basic Theory of Tunneling.....	22
2.1.2 The Bardeen Theory of Tunneling	25
2.1.3 Tersoff and Hamann Approximation	26
2.1.4 Scanning Tunneling Spectroscopy (STS)	27

2.1.5 Experimental Set-up of RT-STM	30
2.2 Low Energy Electron Diffraction (LEED)	31
2.2.1 The Principle of LEED	31
2.2.2 The Basic Theory of LEED	32
2.3 Tungsten (W) Tip Preparation.....	36
2.3.1 Fabrication of Tungsten Tip by Alternating Current.....	37
2.3.2 The Thermal Treatment of Tungsten Tip	39
2.4 Bibliography	40
Chapter 3 Epitaxial Graphene Grown on 6H-SiC	43
3.1 Introduction	44
3.2 Experimental Procedure of Epitaxial Graphene Grown on 6H-SiC (0001).44	
3.3 Topography and Electronic Properties of Graphene on 6H-SiC (0001)	50
3.3.1 Topography and Electronic Properties of the Buffer Layer	50
3.3.2 Topography and Electronic Properties of Monolayer Graphene on 6H-SiC (0001)	55
3.3.3 Topography and Electronic Properties of Bilayer Graphene on 6H-SiC (0001)	57
3.4 Epitaxial Graphene Grown on 6H-SiC (000-1).....	61
3.4.1 Experimental Procedure to Grow Graphene on 6H-SiC (000-1).....	61
3.4.2 Topography of Graphene on 6H-SiC (000-1)	61
3.4.3 Electronic Properties of Graphene on 6H-SiC (000-1)	69
3.5 Conclusions	72
3.6 Bibliography	73

Chapter 4 Electronic Properties of Ni-Phthalocyanine Molecules on Graphene 79

4.1 Introduction	80
4.2 Experimental Procedure	81
4.3 Topography of Self-Assembled NiPc Molecules on Graphene/ 6H-SiC (0001)	82
4.3.1 Steps of NiPc Molecular Network on Monolayer Graphene	82
4.3.2 Atomic-Scale STM Images of NiPc Molecules on Graphene	86
4.4 Electronic Properties of NiPc Molecules on Graphene	90
4.5 DFT Calculations of NiPc Molecules on Graphene/SiC (0001)	92
4.5.1 Topography of NiPc Molecules on Graphene	92
4.5.2 Interpretation of Spectroscopy Results by DFT Calculation	98
4.6 Conclusions	104
4.7 Bibliography	104

Chapter 5 Electronic Properties of Pt-Tetraphenylporphyrin Molecules on Graphene..... 107

5.1 Introduction	108
5.2 Experimental Procedure	109
5.3 Self-Assembled PtTPP Molecules on Graphene	110
5.3.1 Self-Assembled PtTPP Molecules on Graphene/ SiC (0001)	110
5.3.2 Self-Assembled PtTPP Molecules on Graphene/6H-SiC (000-1)...	118
5.4 Scanning Tunneling Spectroscopy of PtTPP Molecules on Graphene	121
5.5 DFT Calculations of PtTPP Molecules on Graphene	124
5.5.1 PtTPP Molecular Network on Graphene	124
5.5.2 Topography and Electronic Properties of PtTPP on Graphene	126

5.5.3 Electronic Coupling between PtTPP Molecules and Graphene	131
5.6 Conclusions	135
5.7 Bibliography.....	136
Chapter 6 Electronic Properties of Fe -Tetraphenylporphyrin Molecules on Graphene.....	139
6.1 Introduction	140
6.2 Experimental Procedure	140
6.3 Self-Assembled FeTPP Molecules on Graphene/ SiC (0001)	142
6.3.1 Single-Layer FeTPP Molecular Network.....	142
6.3.2 Molecular Adsorbates on top of the Well-Ordered Molecular Network	144
6.4 Double-Layer FeTPP Molecular Network on Graphene/ SiC (0001).....	148
6.5 Self-Assembled FeTPP Molecules on Graphene/ SiC (000-1).....	155
6.6 STS of FeTPP Molecules on both Graphene/ SiC (0001) and Graphene/ SiC (000-1).....	158
6.7 Conclusions	167
6.8 Bibliography.....	168
Conclusions and Perspectives.....	171

Chapter 1

Introduction

Table of Contents

1.1 The Development of Electronic Technology.....	2
1.2 The Development of Molecular Devices.....	2
1.3 Spin Field-Effect Transistor.....	4
1.3.1 Spin-FET based on Graphene.....	5
1.3.2 The Functionalization of Graphene.....	6
1.4 The Self-Assembled Organic Molecules on Surface	8
1.4.1 Molecular Self-Assembly.....	8
1.4.2 Energy Level Alignment at the Molecule/ Substrate Interface	9
1.5 The Project and My Subject.....	12
1.6 Bibliography.....	13

1.1 The Development of Electronic Technology

Silicon-based electronic technology has achieved extraordinary advances over the past several decades. In the integrated circuit era, this progress has been achieved primarily through the scaling of the metal-oxide-semiconductor field-effect transistor (MOSFET) into smaller and smaller dimensions, therefore leading to both higher speed and device density[1]. However, it is now generally accepted that silicon devices will be reaching some fundamental scaling limits at the spatial scale below 10 nm. This realization has sparked an intense search for alternative technologies, an effort that involves searching for both new device principles and materials. In this search, scientists are guided by the experience gained during the decades of device research and by the performance standards set by the highly advanced silicon technology. It is critical to investigate logic systems, in which devices are always part of a large and complex system, that any future devices exhibit sufficient amplification so that signals can be referenced and restored to a reference voltage at each stage of a long chain of logical operations. Logical systems built without this amplification would be susceptible to noise from thermal fluctuations and external environmental disturbances as well as signal variations arising from the unavoidable manufacturing variations and aging of the devices themselves. One promising direction for the future electronic devices involves “molecular electronics” in which the active part of the device is composed of a single or a few molecules, because they can be prepared with the method of well-known and easily reproducible chemical synthesis[2, 3].

1.2 The Development of Molecular Devices

The first proposal of using molecular components in electronic devices was discussed in the United States Defense Department as a potentially promising subject in the late 1950s based on a visionary comment from Richard P. Feynman “there is plenty of

room at the bottom”[4]. In 1974, Ari Aviram and Mark A. Ratner (AR) proposed an electrical rectification by a single molecule with suitable electronic asymmetry and the conductivity of the organic molecules in electronic circuit was first detected[5]. From 1990s, the experimental realizations of molecular-scale devices made the dream of molecular devices a reality. Single-molecule junctions were studied to understand the electronic structure and function at interfaces, in and out of equilibrium, and in heterogeneous environments from a fundamental standpoint[6]. Bingqian Xu and Nongjian J. Tao measured single molecule conductance for several organic compounds between a gold scanning tunneling microscope (STM) tip and a gold surface in 2003[7]. Metal-porphyrin molecules were also used in single molecule break junction to study the charge transport (Zn-porphyrin) [8], optical effects (Mg-Porphyrin)[9], spin-dependent transport and the Kondo effect (CoPc[10], TbPc₂[11])[12]. In 2005, the use of an organic molecule as a single molecule transistor in which the current through the molecule was modulated by a gate potential applied at room temperature was reported by Bingqian Xu and Nongjian J. Tao [13]. In 2013, the electron transport mechanism in unimolecular amplifier with three-terminals were studied by Cormac Toher, et al[14]. However, this amplifier with three-terminals is not a Field Effect Transistor (FET) but rather a bipolar junction transistor. Molecular electronics have attracted tremendous interests in nanoscience, whereas, there is still a long way to go before they are paid attention by industry [15].

Carbon based nanomaterials[16], especially carbon nanotubes (CNT) and graphene, are strong candidates as building blocks for molecular electronics, because they have semiconductor properties and dimensions within the required physical limit to establish electrical connections[17]. CNTs are macromolecular systems with unique physical and chemical properties. Depending on their chirality, they can be metals or semiconductors. The small diameter and long length of single-walled carbon nanotubes (SWCNTs) lead to very large aspect ratios that make them almost ideal

one-dimensional (1D) systems[18]. It was reported the carbon nanotube-based field effect transistors have excellent operating characteristics that are as good as or better than state-of-the-art silicon devices[3].

Graphene is a ultra-thin two-dimensional sheet of covalently bonded carbon atoms with outstanding electronic properties, chemical stability and mechanical material properties[19-21]. It is considered to be a good electrode candidate for molecular junctions. Furthermore, large-area, conductive and flexible graphene films have been successfully synthesized, with the ability to be patterned or created in any desired size and shape of film[22]. For this reason, graphene films have the potential to play a crucial role as a conductive electrode for organic electronic devices[23]. For example, many studies have reported graphene electrodes in organic-based devices such as memories[24], field-effect transistors[25], and light-emitting diodes[26]. TbPc₂ single-molecule magnet spin transistor was reported [11, 27]. The graphene nanoribbon decorated with TbPc₂ magnetic molecules has potential to be used in the spin-filed effect transistor (Spin-FET)[28]. Spin-FET was first proposed in 1990 by Supriyo Datta and Biswajit Das[29] based on the requirements for the next generation electron devices; smaller size, higher efficiency and lower energy consumption, in which the charge carrier is replaced by spin. Grafting organic molecules to graphene might be a key step to transfer spin between the source and drain.

1.3 Spin Field-Effect Transistor

The model of the spin field effect transistor is shown in Figure 1.1. In spin-FET, the source and collector are ferromagnetic metals whose spin directions are parallel to each other. The spin-polarized electrons are injected from the source, and then transmitted to the drain by a nonmagnetic layer. A gate voltage is applied to control the precession of the spin polarized electrons. When the gate voltage is zero ($V_g=0$), the injected spins start to rotate and reach the collector with a different polarization

state, because of ‘Rashba Effect’¹. When a non-zero gate voltage is applied, $V_g \gg 0$, the rotation of the electron spin is controlled by the electric field, thereby allowing the spins to reach the collector (drain) with the same polarization. In spin-FET, it is crucial for the nonmagnetic layer to have a long spin-relaxation time and large spin diffusion length (weak spin-orbit interaction) when electrons travel from the source to the detector. Hence, it is crucial to look for potential candidates for the non-magnetic layer to make spin-FET come true.

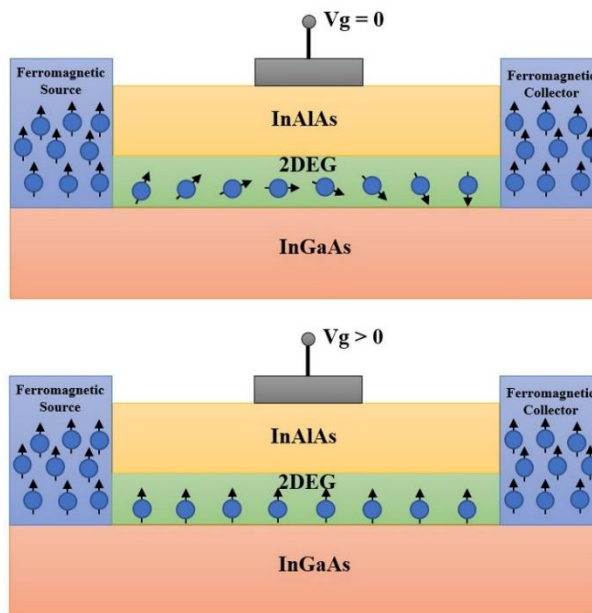


Figure 1.1 Spin polarized field effect transistor model proposed by Datta and Das. V_g is the applied gate voltage.

1.3.1 Spin-FET based on Graphene

Since graphene was first fabricated by Andre Geim and Konstantin Novoselov using the scotch tape method in 2004, it has attracted tremendous interest from researchers

¹ Rashba effect is the splitting of the bands caused by the spin-orbit interaction and structure inversion asymmetry.

in physics, chemistry and material science. Graphene is a one-atom-thick planar sheet of sp₂ bonded C atoms with honeycomb lattice structure. The linear band structure and zero band gap make the electrons and holes in graphene behave as Dirac fermions. Graphene holds a number of extraordinary properties: a remarkable electron mobility (15000 cm²/V/s), unique optical properties, strong mechanical properties, and so on, which makes graphene very promising to be used as a material in the future nano-electronics. It is particularly worth mentioning here, that graphene is claimed to be an ideal material for spintronics due to its small spin-orbit interaction and the near absence of nuclear magnetic moments in carbon. The spin coherence length in graphene is observed to be in excess of 1μm at room temperature[30] and the control of the spin current polarity with an electrical gate was detected at low temperature[31].

The spin-FET based on a graphene channel was first reported by Y. G. Semenov and K. W. Kim[32]. In which, the effective magnetic field caused by the Rashba effect is replaced by the exchange interaction between the graphene and ferromagnetic dielectric. If an external electric field is applied perpendicularly to the graphene sheet via the gate, the exchange interaction can be adjusted, which in turn will act on the spin rotation angle. The spin rotation induced by the Rashba effect requires a relatively strong spin-orbit coupling. However, for the graphene spin FET transistor, the great challenge is to harness the weak spin-orbit coupling.

1.3.2 The Functionalization of Graphene

In a spin-FET based on graphene, the functionalization of graphene to strengthen the spin-orbital interaction is the most urgent problem to be solved. Functionalization of graphene with organic molecules via noncovalent bonding can be a promising solution, since this can be performed by chemical methods and under vacuum. The electronic interactions between molecules and graphene via the van der Waals, electrostatic, dipole-dipole, or hydrogen bonding interactions are favorable to

preserve both the extraordinary electronic properties of graphene and the magnetic properties of organic molecules[33]. At the same time, the weak electronic coupling between molecules and graphene can lead to a small doping effect in graphene[34], open the graphene band gap[35, 36], or induce the magnetic moment[37] in a molecular layer.

Metal-coordinated organic molecules, in particular metal-phthalocyanine (MPc), metal-porphyrin (MP) and their derivatives have the potential to modify graphene, because of the π -conjugated electronic structure with tunable electronic and magnetic properties through the appropriate choice of the central metal ion. Specifically, the metal phthalocyanines are part of the most important groups of organic semi and photo-conductors. They are planar molecules and consist of four isoindole units joined together by four extracyclic nitrogens to form a compound with a 16-membered central ring with one metal atom in the center. The over-all symmetry of the molecule is D_{4h} with the four-fold axis of rotation passing through the metal atom and perpendicular to the plane of the molecule[38, 39]. Metal tetraphenylporphyrins have also received much attention because of their intrinsically interesting magnetic, spectroscopic and electrochemical properties. The porphyrin macrocyclic arrangement has four pyrrole rings connected by methine units and this is extraordinarily stable. The nitrogen atoms at the interior form a central pocket ideally positioned to firmly incorporate metal atoms in a tetradeятate ligand. These anionic centers represent coordinatively unsaturated units for charge transfer and ligation of adducts, which occurs with reversible changes of electronic configuration, for example oxidation or spin states. The structure also renders itself to possible modification-a large variety of substituents can be attached at pyrrolic β sites or linked to the meso-positions at the methine bridges[40, 41].

Functionalization graphene by metal-phthalocyanine and metal tetraphenylporphyrin molecules is a promising method to induce or keep the magnetic moments in the molecules, and increase the spin-orbit interaction in graphene, making them suitable

for use in spin-FET. Therefore, it is of fundamental significance to understand the electronic interaction at the molecule-graphene interface.

1.4 The Self-Assembled Organic Molecules on Surface

1.4.1 Molecular Self-Assembly

Molecular self-assembly is the spontaneously association of molecules via the non-covalent bonding into a stable and well-structured aggregates[42]. The goal of this discipline is to construct functional nanostructures by synthesizing molecular structural units with predetermined intermolecular binding properties [43-45]. The formation of surface structures is the core of future nanotechnology, and it has potential applications in areas, such as surface functionalization[46], biosensors[47], molecular electronics[48] and heterogeneous asymmetric catalysis[49].

In order to design and form the desired supramolecular structure, it is necessary to understand the interaction under self-assembly. The consequence of molecular self-assembly processes on surfaces usually depend on molecular and molecular-substrate interactions. Generally, molecular self-assembly is stabilized by relatively weak bonds, including van der Waals[50, 51], hydrogen bonds[52, 53] and aromatic interactions[54-56]. Among them, the heteromolecular hydrogen bond system typically utilizes donor-acceptor interactions to achieve the strong intermolecular binding[57, 58]. The van der Waals forces are usually less directional, so the resulting pattern usually depends on factors such as molecular geometrical[59] or stoichiometric factors, as observed in self-mixing structures consisting of subphthalocyanines and C₆₀ on Ag (111)[60]. In addition, molecules interacting through van der Waals interactions are often found to be closed and form a number of competing (metastable) molecular phases that differ only slightly in energy[61].

Likewise, metal-organic bonds[62], electrostatic[63] and substrate-mediated interactions[64, 65] can be the stabilizing forces in monolayer formation.

1.4.2 Energy Level Alignment at the Molecule/ Substrate Interface

All electronic circuits that rely on the use of semiconductors needs to deal with a physical challenging system: metal/ semiconductor interface. Nowadays, the metal and inorganic semiconductors are well-understood (band bending, interface states...). Whereas, the organic semiconductors have the different nature from their inorganic counterparts (the former are the molecular solids, while the latter are covalent/ partial ionic solids), the inorganic semiconductor theory does not work properly for them. To get a good performance in semiconductor electronic devices, the electron injected barrier must be as small as possible. It indicates the energy level alignment at the interfaces is very important.

Some molecules that form organic semiconductors are chemisorbed on metals. The work function change has been reported for a lot of chemisorbed molecules on metal. The charge transfer between metal and molecule creates a dipole layer between both systems, leading to a work function change. In addition, the charge redistribution due to the bond formation also leads to the change of work function. The charge transfer between metal and organic molecules has been reported on TCNQ/ Au, TPD/Au[66], and so on.

For the adsorption of organic molecules on metal via the physisorption with no charge transfer, the work function also might change. When we have a non-polar molecule, at a certain moment, a net dipole on the molecule can appear because of quantum fluctuations. The metal reacts with this dipole creating an image dipole. The interaction of these dipoles gives rise to van der Waals forces. However, this interaction of the net dipole with screening charge can give rise to a net displacement of the electron distribution in the adsorbates and create a potential drop at the interface[67, 68].

Other source of dipole is the “pillow” dipole. It is because of the Pauli exclusion principle. When a molecule is placed on a metal surface, wave functions of both the

metal and molecular atoms overlap. When we orthogonalize both wave functions, the electron metal tails are pushed back into the metal. This charge redistribution reduces the surface dipole, indicating the work function will be reduced whenever a molecule is placed on a metal surface, no matter if the molecule is an electron donor or acceptor. In the case of an electron acceptor the pillow dipole and the charge transfer dipole compete with each other. This effect should be more important in the cases where the surface contribution to work function dipole is more important[69].

Some molecules have an intrinsic dipole. When they are adsorbed on a metal surface, they have a non negligible component on the direction perpendicular to the surface. This intrinsic molecular dipole orientation gives rise to a potential drop at the interface[70].

The induced density of interface states (IDIS) model was created for the metal/inorganic semiconductor interfaces. It can be extended for metal/ organic interfaces[71]. The main idea of this model is that the physical/ chemical interaction between the first layer organic material and the metal induces a non-negligible DOS at the semiconducting gap. This DOS appears because of the formation of the hybrid metal/ organic states at the gap due to strong chemical interaction between molecules and metal at the interface, or due to the broadening of HOMO and LUMO levels because of interaction with the metal. Before introduce the details of IDIS model, it is necessary to define the main parameter in this model, the Charge Neutrality Level (CNL). The CNL can be regarded as a kind of effective Fermi level of the organic molecule. It can be calculated as the integral of the DOS projected on the interacting organic molecule up to charge neutrality conditions. Due to the interaction between organic molecules and metal, the peak-like DOS of the molecule is transformed to a continuous DOS, therefore, we can integrate it:

$$N = \int_{-\infty}^{CNL} \rho_{\text{interacting}}(E) dE \quad (1.1)$$

Although intuitively the CNL should be at the middle of the HOMO and LUMO levels, this is not true[72]. Usually, the DOS is higher around the HOMO than around the LUMO[73]. The relative position of the metal work function (ϕ_M) with respect to the organic CNL determines the direction of the charge transfer. If $CNL > \phi_M$, the electrons will flow from the organic layer to the metal, on the contrary, when $CNL < \phi_M$, the electrons transfer from the metal to the molecule. These charge transfer creates a dipole and induces a potential drop at the interface. The effect of this dipole is to move the final Fermi level and tend to pin it to the CNL. The potential drop that changes the interface Fermi level from ϕ_M to E_F can be related with the electrostatic dipole through the formula:

$$\Delta = \frac{4\pi D}{A} \quad (1.2)$$

Where, D is the electrostatic dipole, Δ is the potential drop at the interface and A is the surface area that belongs to each molecule.

This pinning of the Fermi level is governed by the screening parameter, S. If we consider that the CNL is always fixed with respect to the vacuum, and the level movement due to the dipole is only on metallic levels, the screening parameter can be written as:

$$S = \frac{CNL - E_F}{CNL - \phi_M} \quad (1.3)$$

Therefore, the S can be seen as the value that control the reduction of the $(CNL - \phi_M)$ distance to $CNL - E_F$. The lower the S parameter is, the greater the pinning of the final Fermi level to the CNL.

In the IDIS model we discussed above, the charge transfer is the unique source of the interface dipole. However, there are more sources, although smaller than the charge transfer dipole. They are the pillow dipole and the surface dipole. If take the pillow effect into account in the model, the effective metal work function will be:

$$\phi'_M = \phi_M + \Delta_0^P \quad (\Delta_0^P = \frac{4\pi D_{pillow}}{A}) \quad (1.4)$$

The total potential at the interface:

$$\Delta_{\text{total}} = E_F - \phi_M = E_F - \phi'_M + \Delta_0^P = (1 - S)(CNL - \phi'_M) + \Delta_0^P \quad (1.5)$$

It can be argued that the net potential is the sum of the pillow potential and the potential caused by the charge transfer. On the other hand, it can be regarded as:

$$\Delta_{\text{total}} = (1 - S)(CNL - \phi_M - \Delta_0^P) + \Delta_0^P = (1 - S)(CNL - \phi_M) + S\Delta_0^P = \Delta_{\text{IDIS}} + \Delta_P \quad (1.6)$$

In this case, the total potential is the sum of the IDIS potential due to charge transfer neglecting the pillow effect plus a screened pillow potential Δ_P .

1.5 The Project and My Subject

The project we are involved is ‘Magnetic Properties of Graphene Functionalized with 2D Molecular Assemblies (MAGMA)’, involving different organometallic complexes on graphene. This project is funded by the French National Research Agency (ANR). The general research objective is to investigate the magnetism and the spin-orbit interactions in graphene induced by molecular functionalization, while the ultimate goal is to produce a quantum spin Hall state. This project will be implemented by a collaboration of four research groups in France: Institut des Sciences Moléculaires d’Orsay (ISMO), Laboratoire de Physique des Solides (LPS) in Orsay, Commissariat à l’Énergie Atomique et aux Énergies Alternatives (CEA) in Saclay, and Institut Néel in Grenoble.

My subject is focused on the topography of the self-assembled molecular building blocks and the electronic interactions at the molecule/ graphene interface. Specifically, graphene was prepared by the sublimation of Si atoms from SiC substrate in the ultra-high vacuum (UHV). Three metal-coordinated organic molecules which carry different spin information (NiPc, PtTPP and FeTPP) were selected to functionalize graphene. The topography of the organic molecules is studied by Scanning Tunneling Microscopy (STM), the electronic coupling between molecules and graphene is detected by Scanning Tunneling Spectroscopy (STS). The DFT calculations are part

of an ongoing collaboration and were performed by Prof. Philippe Sonnet (IS2M, Mulhouse), Dr. Eric Duverger (FEMTO-ST, Besançon) and Dr Yannick Dappe (CEA, Gif sur Yvette) to help us provide a better interpretation of the physics hidden behind the experimental results.

In this thesis, the techniques and methods used in the experiment are introduced in Chapter 2, the detailed preparation procedures and electronic properties of graphene on both SiC (0001) and SiC (000-1) substrate are presented in Chapter 3. After that, the self-assembled molecular topography and electronic coupling regimes between three different organic molecules and graphene are discussed in Chapter 4 (NiPc molecule), Chapter 5 (PtTPP(CO₂Me)₄ molecule) and Chapter 6 (Fe(TPP)Cl molecule), respectively. Chapter 7 is the conclusion for the whole thesis and the perspectives for future work.

1.6 Bibliography

- [1] Y. Taur and T. H. Ning. Fundamentals of modern VLSI devices: second edition. United Kingdom: Cambridge University Press (2009).
- [2] C. Joachim, J. K. Gimzewski and A. Aviram. Electronics using hybrid-molecular and mono-molecular devices. *Nature*, 408: 541-548 (2000).
- [3] P. Avouris. Molecular electronics with carbon nanotubes. *Acc. Chem. Res.*, 35: 1026-1034 (2002).
- [4] R. P. Feynman. There's plenty of room at the bottom. *Eng. Sci.*, 23: 22-36 (1960).
- [5] A. Aviram and M. A. Ratner. Molecular rectifiers. *Chem. Phys. Lett.*, 29: 277-283 (1974).
- [6] M. Ratner. A brief history of molecular electronics. *Nature Nanotech.*, 8: 377-381 (2013).
- [7] B. Q. Xu and N. J. Tao. Measurement of single-molecule resistance by repeated formation of molecular junctions. *Science*, 301: 1221 (2003).

- [8] M. L. Perrin, C. A. Martin, *et al.* Charge transport in a Zn-porphyrin single molecule junction. *Beilstein J Nanotechnol.*, 2: 714-719 (2011).
- [9] S. W. Wu, G. V. Nazin andW. Ho. Intramolecular photon emission from a single molecule in a scanning tunneling microscope. *Phys. Rev. B.*, 77: 205430 (2008).
- [10] C. Iacobita, M. V. Rastei, *et al.* Visualizing the spin of individual cobalt-phthalocyanine molecules. *PRL.*, 101: 116602 (2008).
- [11] J. Schwöbel, Y. S. Fu, *et al.* Real-space observation of spin-split molecular orbitals of adsorbed single-molecule magnets. *Nat. Commun.*, 3: 953 (2012).
- [12] S. V. Aradhya and L. Venkataraman. Single-molecule junctions beyond electronic transport. *Nature Nanotech.*, 8: 399-410 (2013).
- [13] B. Q. Xu, X. Y. Xiao, *et al.* Large gate modulation in the current of a room temperature single molecule transistor. *J. Am. Chem. Soc.*, 127: 2386-2387 (2005).
- [14] C. Toher, D. Nozaki, *et al.* Unimolecular amplifier: principles of a three-terminal device with power gain. *Nanoscale.*, 5: 6975 (2013).
- [15] R. M. Metzger. Unimolecular electronics. *Chem. Rev.*, 115: 5056-5115 (2015).
- [16] T. Akasaka and F. W. S. Nagase. *Chemistry of nanocarbons*. Wiley (2010).
- [17] K. Sablon. Nanoelectrodes for molecular devices: A controllable fabrication. *Nanoscale Res Lett.*, 3: 268-270 (2008).
- [18] P. G. Collins and P. Avouris. Nanotubes for electronics. *Sci Am.*, 283: (2000).
- [19] K. S. Novoselov, A. K. Geim, *et al.* Electric Field Effect in Atomically Thin Carbon Films. *Science*, 306: 666-669 (2004).
- [20] I. Meric, M. Y. Han, *et al.* Current saturation in zero-bandgap, top-gated graphene field-effect transistors. *Nature Nanotech.*, 3: 654-659 (2008).
- [21] Y. B. Zhang, Y. W. Tan, *et al.* Experimental observation of the quantum Hall effect and Berry's phase in graphene. *Nano Lett.*, 438: 201-204 (2005).
- [22] A. Reina, X. T. Jia, *et al.* Large area, few-layer graphene films on arbitrary substrates by chemical vapor deposition. *Nano Lett.*, 9: 30-35 (2009).

- [23] G. Wang, Y. H. Kim, *et al.* A new approach for molecular electronic junctions with a multilayer graphene electrode. *Adv. Mater.*, 23: 755-760 (2011).
- [24] J. Q. Liu, Z. Y. Yin, *et al.* Bulk heterojunction polymer memory devices with reduced graphene oxide as electrodes. *ACS Nano.*, 4: 3987-3992 (2010).
- [25] C. A. Di, D. C. Wei, *et al.* Patterned graphene as source/ drain electrodes for bottom-contact organic field-effect transistors. *Adv. Mater.*, 20: 3289-3293 (2008).
- [26] G. Jo, M. Choe, *et al.* Large-scale patterned multi-layer graphene films as transparent conducting electrodes for GaN light-emitting diodes. *Nanotechnology.*, 21: 175201 (2010).
- [27] S. Thiele, R. Vincent, *et al.* Electrical readout of individual nuclear spin trajectories in a single-molecule magnet spin transistor. *PRL.*, 111: 037203 (2013).
- [28] A. Candini, S. Klyatskaya, *et al.* Graphene spintronic devices with molecular nanomagnets. *Nano Lett.*, 11: 2634-2639 (2011).
- [29] S. Datta and B. Das. Electronic analog of the electro-optic modulator. *Appl. Phys. Lett.*, 56: 665 (1990).
- [30] N. Tombros, C. Jozsa, *et al.* Electronic spin transport and spin precession in single graphene layers at room temperature. *Nature.*, 448: (2007).
- [31] S. Cho, Y. F. Chen andM. S. Fuhrer. Gate-tunable graphene spin valve *Appl. Phys. Lett.*, 91: 123105 (2007).
- [32] Y. G. Semenov, K. W. Kim andJ. M. Zavada. Spin field effect transistor with a graphene channel. *Appl. Phys. Lett.*, 91: 153105 (2007).
- [33] A. Ciesielski and P. Samori. Supramolecular approaches to graphene: From self-assembly to molecule-assisted liquid-phase exfoliation. *Adv Mater.*, 28: 6030-6051 (2016).
- [34] X. Y. Zhang, E. H. Huisman, *et al.* Supramolecular chemistry on graphene field-effect transistors. *Small.*, 10: 1735-1740 (2014).

- [35] A. J. Samuels and J. D. Carey. Molecular doping and band-gap opening of bilayer graphene. *ACS Nano.*, 7: 2790-2799 (2013).
- [36] Arramel, A. C. Gomez and B. J. v. Wees. Band gap opening of graphene by noncovalent π - π interaction with porphyrins. *Graphene.*, 2: 102-108 (2013).
- [37] C. Li, K. Komatsu, *et al.* Signature of gate-tunable magnetism in graphene grafted with Pt-porphyrins. *Phys. Rev. B.*, 93: 045403 (2016).
- [38] M. S. Liao and S. Scheiner. Electronic structure and bonding in metal phthalocyanines, Metal=Fe, Co, Ni, Cu, Zn, Mg. *J. Chem. Phys.*, 114: 9780-9791 (2001).
- [39] S. C. Mathur and J. Singh. Molecular electronic structure of metal phthalocyanines *Int. J. Quantum Chem.*, 1: 57-82 (1972).
- [40] W. Auwärter, D. Écija, *et al.* Porphyrins at interfaces. *Nature Chem.*, 7: 105-120 (2015).
- [41] M. S. Liao and S. Scheiner. Electronic structure and bonding in metal porphyrins, metal= Fe, Co, Ni, Cu, Zn. *J. Chem. Phys.*, 117: 205-219 (2002).
- [42] G. M. Whitesides, J. P. Mathias and C. T. Seto. Molecular self-assembly and nanochemistry: A chemical strategy for the synthesis of nanostructures. *Science.*, 254: 1312-1319 (1991).
- [43] G. M. Whitesides and B. Grzybowski. Self-assembly at all scales. *Sciene*, 295: 2418-2421 (2002).
- [44] J. V. Barth, G. Costantini and K. Kern. Engineering atomic and molecular nanostructures at surfaces. *Nature*, 437: 671-679 (2005).
- [45] S. D. Feyter and F. C. D. Schryver. Two-dimensional supramolecular self-assembly probed by scanning tunneling microscopy. *Chem. Soc. Rev.*, 32: 139-150 (2003).
- [46] P. B. Messersmith and M. Textor. Nanomaterials: Enzymes on nanotubes thwart fouling. *Nature Nanotechnology.*, 2: 138-139 (2007).

- [47] F. Davis and S. P. J. Higson. Structured thin films as functional components within biosensors. *Biosens. Bioelectron.*, 21: 1-20 (2005).
- [48] F. Rosei, M. Schunack, *et al.* Properties of large organic molecules on metal surfaces. *Prog. Surf. Sci.*, 71: 95-146 (2002).
- [49] C. J. Baddeley, T. E. Jones, *et al.* Fundamental investigations of enantioselective heterogeneous catalysis. *Top. Catal.*, 54: 1348-1356 (2011).
- [50] K. Tahara, S. Furukawa, *et al.* Two-dimensional porous molecular networks of dehydrobenzo(12) annulene derivatives via alkyl chain interdigitation. *J. Am. Chem. Soc.*, 128: 16613-16625 (2006).
- [51] S. Furukawa, H. Uji-i, *et al.* Molecular geometry directed kagomé and honeycomb networks: Toward two-dimensional crystal engineering. *J. Am. Chem. Soc.*, 128: 3502-3503 (2006).
- [52] M. Lackinger and W. M. Heckl. Carboxylic acids: versatile building blocks and mediators for two-dimensional supramolecular self-assembly. *Langmuir*, 25: 11307-11321 (2009).
- [53] S. B. Lei, C. Wang, *et al.* Surface porphyrin and phthalocyanine two-dimensional network connected by hydrogen bonds. *J. Phys. Chem. B.*, 105: 10838-10841 (2001).
- [54] S. Weigelt, C. Busse, *et al.* Influence of molecular geometry on the adsorption orientation for oligophenylene-ethynlenes on Au(111). *J. Phys. Chem. B.*, 111: 11342-11345 (2007).
- [55] H. Wang, T. E. Kaiser, *et al.* Perylene bisimide J-aggregates with absorption maxima in the NIR. *Chem. Commun.*, 1181-1183 (2008).
- [56] J. Reichert, A. Schiffelin, *et al.* L-Tyrosine on Ag(111): Universality of the amino acid 2D zwitterionic bonding scheme? *ACS Nano*, 4: 1218-1226 (2010).
- [57] J. A. Theobald, N. S. Oxtoby, *et al.* Controlling molecular deposition and layer structure with supramolecular surface assemblies. *Nature*, 424: 1029-1031 (2003).

- [58] J. Ma, B. L. Rogers, *et al.* Dianhydride-amine hydrogen bonded perylene tetracarboxylic dianhydride and tetraaminobenzene rows. *J Phys Chem B.*, 110: 12207-12210 (2006).
- [59] M. Schock, R. Otero, *et al.* Chiral close-packing of achiral star-shaped molecules on solid surfaces. *J. Phys. Chem. B.*, 110: 12835-12838 (2006).
- [60] M. d. Wild, S. Berner, *et al.* A novel route to molecular self-assembly: self-intermixed monolayer phases. *Chem phys chem.*, 3: 881-885 (2002).
- [61] L. Gross, F. Moresco, *et al.* Tailoring molecular self-organization by chemical synthesis: Hexaphenylbenzene, hexa-peri-hexabenzocoronene, and derivatives on Cu (111). *Phys. Rev. B.*, 71: 165428 (2005).
- [62] S. Stepanow, N. Lin and J. V. Barth. Modular assembly of low-dimensional coordination architectures on metal surfaces. *J Phys-Condens Mat.*, 20: 184002 (2008).
- [63] M. Böhringer, W. D. Schneider and R. Berndt. Real space observation of a chiral phase transition in a two-dimensional organic layer. *Angew. Chem.-Int. Edit.*, 39: (2000).
- [64] G. Pawin, K. G. Pawin, *et al.* A homomolecular porous network at a Cu(111) surface. *Science.*, 313: 961-962 (2006).
- [65] Y. Wang, X. Ge, *et al.* Supramolecular patterns controlled by electron interference and direct intermolecular interactions. *J. Am. Chem. Soc.*, 131: 10400-10402 (2009).
- [66] H. Ishii, K. Sugiyama, *et al.* Energy-level alignment at model interfaces of organic electroluminescent devices studied by UV photoemission: trend in the deviation from the traditional way of estimating the interfacial electronic structures. *IEEE J. Sel. Top. Quantum Electron.*, 4: 24 (1998).
- [67] N. D. Lang. Interaction between closed-shell systems and metal surfaces. *Phys. Rev. Lett.*, 46: 842 (1981).

- [68] N. D. Lang and A. R. Williams. Theory of local-work-function determination by photoemission from rare-gas adsorbates. *Phys. Rev. B*, 25: 2940 (1982).
- [69] Y. C. Chen, J. E. Cunningham and C. P. Flynn. Dependence of rare-gas-adsorbate dipole moment on substrate work function. *Phys. Rev. B.*, 30: 7317 (1984).
- [70] S. Yanagisawa and Y. Morikawa. Theoretical investigation of the electronic structure of the Alq₃/Mg interface. *J. Phys. Condens. Matter.*, 21: 64247 (2009).
- [71] H. Vazquez. Energy level alignment at organic semiconductor interfaces. PhD, Universidad Autónoma de Madrid (2006).
- [72] X. Crispin. Interface dipole at organic/ metal interfaces and organic solar cells. *Energy Mater. Sol. Cells.*, 83: 147-168 (2004).
- [73] E. Abad, Y. J. Dappe, *et al.* C₆H₆/Au(111): Interface dipoles, band alignment, charging energy, and van der Waals interaction. *J. Chem. Phys.*, 134: 044701 (2016).

Chapter 2

Experimental Techniques and Methods

Table of Contents

2.1 Scanning Tunneling Microscopy (STM).....	22
2.1.1 Basic Theory of Tunneling.....	22
2.1.2 The Bardeen Theory of Tunneling.....	25
2.1.3 Tersoff and Hamann Approximation.....	26
2.1.4 Scanning Tunneling Spectroscopy (STS).....	27
2.1.5 Experimental Set-up of RT-STM.....	30
2.2 Low Energy Electron Diffraction (LEED).....	31
2.2.1 The Principle of LEED.....	31
2.2.2 The Basic Theory of LEED.....	32
2.3 Tungsten (W) Tip Preparation.....	36
2.3.1 Fabrication of Tungsten Tip by Alternating Current.....	37
2.3.2 The Thermal Treatment of Tungsten Tip.....	39
2.4 Bibliography.....	40

2.1 Scanning Tunneling Microscope (STM)

The Scanning Tunneling Microscope (STM) is invented by Gerd Binnig and Heinrich Rohrer at IBM Zürich in 1981, they were awarded the Nobel Prize in Physics in 1986 for this invention[1]. The STM resolution can be 0.1 nm in lateral and 0.01 nm in the vertical direction[2], making the imaging and manipulation of surfaces and adsorbates at the atomic level a reality. The STM can be used at temperatures from near zero Kelvin to a several hundred degrees Celsius in different environments (Ultra-high vacuum, air, water, and diverse liquid or gas ambient)[3].

2.1.1 Basic Theory of Tunneling

The basic physical phenomenon underlying STM operation is quantum tunneling. The schematic electron tunnel junction composed of a rectangular barrier is shown in Figure 2.1[4]. According to the quantum theory, an electron has a non-zero probability to tunnel across a potential energy barrier. In the STM, a sharp conducting tip is brought close to a conducting or semi-conducting surface. The tip and sample are separated by a thin insulating medium, such as vacuum, air or liquid, which can be described as an energy barrier. From the perspective of quantum theory, the electrons can be associated to a wave function. If the tip and surface are close enough (distance of about 5 Å~ 10 Å), the wave function of the tip and sample can overlap. After the application of a bias voltage, the offset between the tip and sample Fermi levels gives rise to the tunneling current from one electrode to the other in the nanoampere range. The tunneling current direction (from the occupied state of the tip to the unoccupied state of the sample or vice-versa) depends on the polarity of the bias voltage.

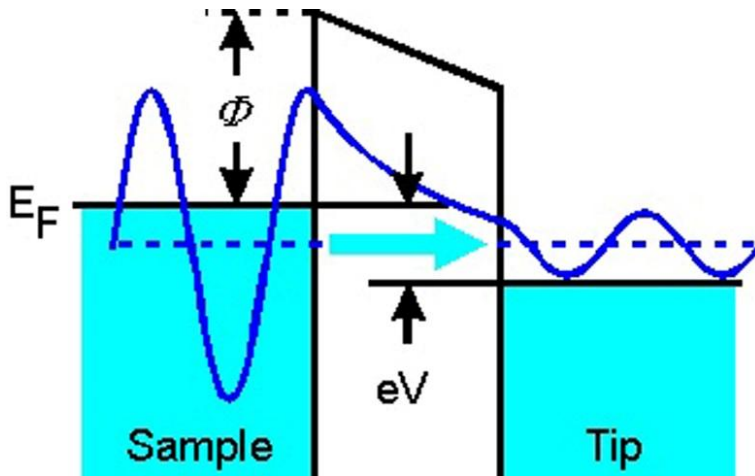


Figure 2.1 Energy level diagram for a tunnel junction: the tip and sample (two electrically conducting materials) are separated by a thin insulating layer (an energy barrier). If the width of the barrier is small enough, the wave functions of tip and sample overlap and the tunneling current can be generated by the application of a bias voltage (V).

Tunneling through a barrier between two conducting electrodes can be considered as a classical problem of a particle tunneling through a potential barrier, where the solution of the Schrödinger equation shows an exponential dependence with respect to the height of the potential barrier.

$$\Psi(x) = \Psi(0)e^{-kd} \quad (2.1)$$

Where, the wave vector is given by $k = \frac{\sqrt{2m_e\phi}}{\hbar}$, m_e is the electron mass, ϕ is the work function of the conducting electrode, d represents the width of the barrier.

The wave function probability density P through the potential barrier is proportional to the square of the wave function:

$$P \propto |\Psi(0)|^2 e^{-2kd} \quad (2.2)$$

The tunneling current depends exponentially on the width of the barrier d :

$$I \propto e^{-2kd} \quad (2.3)$$

From equation 2.3, one can deduce that the tunneling current is very sensitive to the variation of the tip-sample separation. A few angstroms variation in their separation cause a decrease of the tunneling current of one order of magnitude.

The schematic representation of the STM experiment is shown in Figure 2.2. The tip position in X, Y and Z axis are precisely controlled by piezo electric ceramic. There are two imaging modes in STM: constant current mode and constant height mode. In the constant current mode, the feedback loop controls the vertical position of the tip with the topography of the surface. The topographic image of the surface is generated by recording the vertical position of the tip. In our experiment, all the STM images were obtained in the constant current mode. For constant height mode, the tip position is kept constant with the feedback loop off. The current as a function of lateral position represents the surface image. This mode is only suitable for the flat surfaces, otherwise a tip crash would be inevitable. One of the advantages of constant height mode is that it can be used at high scanning frequencies (up to 10 kHz). In comparison, the scanning frequency in the constant current mode is about 1 image per second or even per several minutes. In addition, when the scanning tunneling spectroscopy (STS) is conducted, the feedback loop is cut off, the scanning mode transforms to constant height mode automatically.

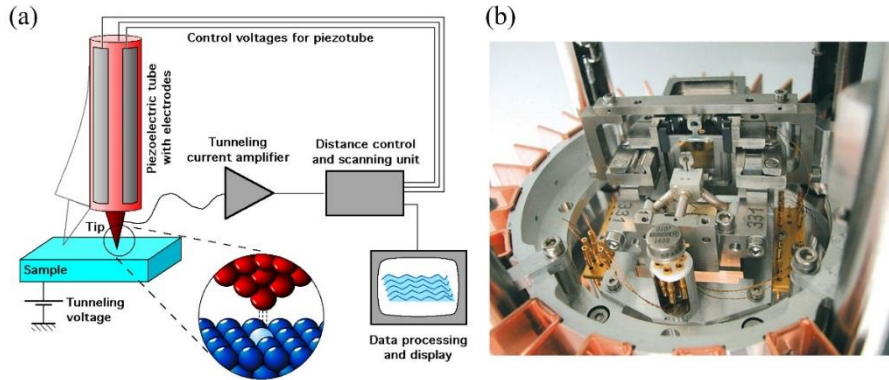


Figure 2.2 (a) The schematic representation of the STM experiment. The tip is scanned across the surface by the piezo driver. The tunneling current is kept constant by controlling the tip-sample separation using the feedback loop. After that, the tunneling current is amplified, recorded and displayed on the screen of the computer; (b) The Omicron Room-Temperature STM (RT-STM) scanner set-up used in the experiment.

2.1.2 The Bardeen Theory of Tunneling

The basic theory to describe the tunneling current in the STM is the first order perturbation theory proposed by Bardeen in 1961[5].The main idea is that the metal-insulator-metal system can be divided into two separated subsystems instead of solving the Schrödinger equation of the whole system. For STM, the tip-vacuum-surface is equivalent to the metal-insulator-metal system, therefore, the electronic states of each subsystem (tip and sample surface) are obtained by solving two stationary Schrödinger equations separately. The stationary Schrödinger equation for the tip (the first subsystem) is:

$$-\frac{\hbar^2}{2m} \frac{\partial^2 \Psi_{tip}}{\partial x^2} + V_{tip} \Psi_{tip} = E \Psi_{tip} \quad (2.4)$$

where, V_{tip} is the tip potential, Ψ_{tip} is the wave function of the tip,

The stationary Schrödinger equation for the sample (the second subsystem) is:

$$-\frac{\hbar^2}{2m} \frac{\partial^2 \Psi_{sam}}{\partial x^2} + V_{sam} \Psi_{sam} = E \Psi_{sam} \quad (2.5)$$

where, V_{sam} is the potential of the sample, Ψ_{sam} is the wave function of the sample.

In the system, the wave functions of the two subsystems are assumed to be orthogonal, therefore, the tunneling matrix can be set as:

$$M = \frac{\hbar^2}{2m} \int \left[\Psi \frac{\partial \chi^*}{\partial z} - \chi^* \frac{\partial \Psi}{\partial z} \right] ds \quad (2.6)$$

From this, we obtain the following expression for the tunneling current:

$$I = \frac{4\pi e}{\hbar} \int_0^{eV} \rho_s(E_F - eV - \varepsilon) \rho_T(E_F + \varepsilon) |M|^2 d\varepsilon \quad (2.7)$$

where, e is the charge of the electron, V is the applied bias voltage, ρ_s and ρ_T are the density of the states (DOSs) of the sample and tip, and M is the tunneling matrix of the tip-sample system[3]. It is obvious that the detailed knowledge of the electronic states of the tip and sample is a pre-requisite for the treatment of the tunneling process, whereas, the tip geometry is not considered at the atomic scale in Bardeen theory.

2.1.3 Tersoff and Hamann Approximation

With the development of scanning probe microscopy, theoretical modeling becomes essential for the correct interpretation of the STM results. In the real experiment, it is impossible either to know or to control the exact geometry of the tip apex, and its shape has a complicated multi atom structure. The consequence is that it is difficult to model the tip impact on the STM images. In 1985, Tersoff and Hamann proposed a STM tip model led on an s orbital which can be described by a spherical potential with a finite radius R , at the same time, the sample and tip subsystems can still be treated separately.

In Bardeen's theory, the tunneling current is given by the formula:

$$I = \frac{2\pi e}{\hbar} \sum_{\mu,\nu} f(E_\mu) [1 - f(E_\nu + eV)] |M_{\mu\nu}|^2 \delta(E_\mu - E_\nu) \quad (2.8)$$

where, V is the bias voltage, $f(E)$ is the Fermi function, $M_{\mu\nu}$ is the tunneling matrix, E_μ and E_ν are the energies of the sample and tip, respectively. Moreover, for

a metal tip, the local density of states (LDOS) can be considered to be uniform over the energy range from E_F to E_V . Thus, in the Tersoff and Hamann model, the tunneling current will just depend on the sample wave function at the position of the tip r_0 (r_0 is the center of the curvature of the tip apex), as below:

$$I \propto V e^{2kR} \rho_s(E_F, \vec{r}_0) \rho_t(E_F) \quad (2.9)$$

where, V is the bias voltage, $\rho_t(E_F)$ is the DOS of the tip at the Fermi level and $\rho_s(E_F, \vec{r}_0)$ is the DOS of the sample at the Fermi level evaluated at the center of the tip. Thus, the tunneling current is proportional to the surface LDOS. In other words, the STM image acquired in the constant current mode represents a contour map of the constant LDOS of the sample. It is important to remember this statement when we analyze the STM images. For instance, a dark defect with a lower LDOS can either be a real vacancy or an adsorbate with a reduced tunneling probability.

2.1.4 Scanning Tunneling Spectroscopy (STS)

According to the Bardeen theory, the tunneling current can be expressed as a convolution between the tip and the surface electronic states:

$$I \propto \int_0^{eV} \rho_s(E_F - eV + \varepsilon) \rho_T(E_F + \varepsilon) d\varepsilon \quad (2.10)$$

In other words, at any given bias voltage, the tunneling current is proportional to the LDOS of the tip and sample. Generally, the tip DOS is uniform compared with DOS of sample surface, therefore, the STM provides us with the local electronic structures of the sample, especially the electronic surface states. This enables the surface states to be probed using the method called scanning tunneling spectroscopy (STS). In STM imaging, the feedback loop is necessary to adjust the tip height to satisfy a certain set-point tunneling current (constant current mode). In STS measurement, the current (I)-voltage (V) curves are recorded on top of a given X, Y coordinate with the feedback loop off. The applied bias voltage varies continuously within the chosen limits from V_{set} to $-V_{\text{set}}$, and the resulting tunneling current is recorded. Thus, the

LDOS on a sample as a function of the electron energy is obtained, as shown in the Figure 2.3. When the sample bias voltage is ramped to a more positive value, the higher empty DOS could contribute to the tunneling process (e.g., the LUMO orbital), when the bias voltage is ramped to a more negative value, the lower energy filled states are addressed (e.g., the HOMO orbital)[6].

It is important to notice that the lateral thermal drift constantly influences the STM images. Hence, a STS measurement should be done in a shorter time than that of the tip drift over a distance equal to the radius of the studied object (a molecule or an atom). The thermal drift of the Omicron RT-STM is less than 1 nm/min. To guarantee the accuracy of the STS spectra, an average of many individual STS measurements should be made at room temperature. The drawback of the I-V curve is that it looks often rather smooth and featureless and does not reveal the involvement of the energy states at first sight. To probe the surface electronic properties, in particular the energy states of the adsorbates on the substrate, the differential conductance curve ($dI/dV-V$) is calculated, which is proportional to the surface LDOS. Sometimes, the normalized differential conductance $dI/dV/(I/V)-V$ or $dlnI/dlnV-V$ is measured. The peaks in the ($dI/dV-V$) curve are the consequence of the opening of a new conducting channel adding to the elastic tunneling process, they are correlated to the filled states (occupied molecular orbitals) and empty states (unoccupied molecular orbitals) of the surface (see Figure 2.3 (c))[7].

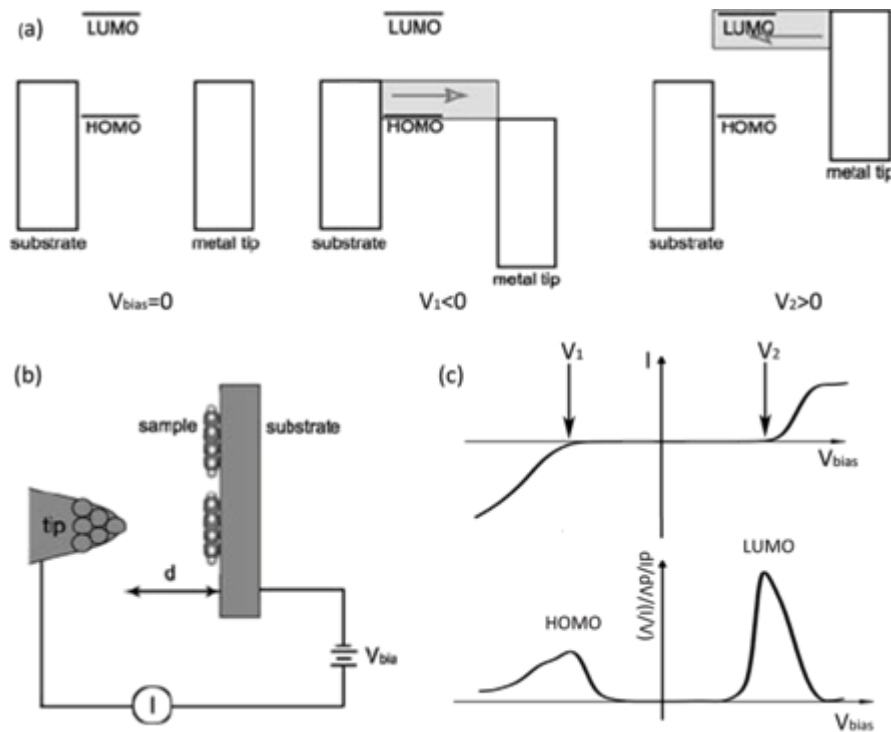


Figure 2.3 The schematic diagram of the STS measurement for the adsorbates on the substrate. When the sample bias voltage is ramped to a negative value, the occupied states (e.g., HOMO) of the adsorbates contribute to the tunneling process; when the sample bias voltage is ramped to a high positive value, the unoccupied states are addressed in the spectroscopy curve. The peaks in the dI/dV (I/V) curves are correlated to the inflection points in the I - V curve.

2.1.5 Experimental Set-up of RT-STM

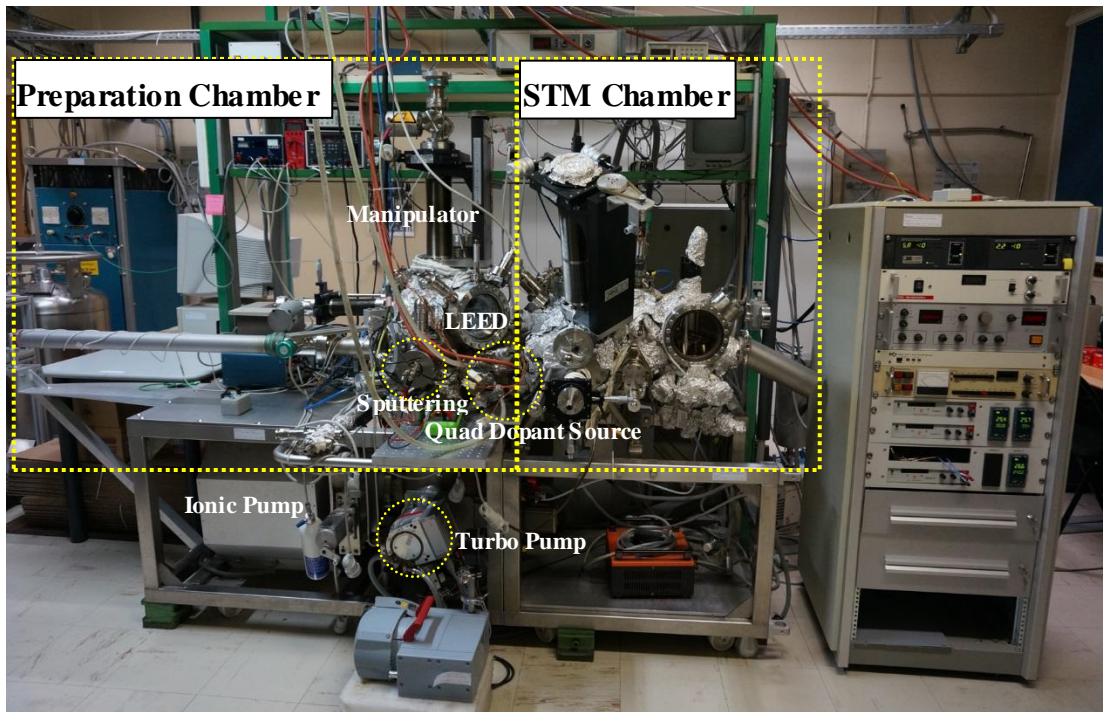


Figure 2.4 The experimental set-up of the RT-STM. The left part is the preparation chamber, the right part is the STM chamber.

In our experiments, the experimental set-up we used is the Omicron room temperature Ultra High Vacuum Scanning Tunneling Microscope (RT-STM). There are two UHV chambers: the preparation chamber and the STM chamber, separated by a gate valve (see Figure 2.4). A load-lock is connected to the preparation chamber, which allows the samples or tips to be inserted or removed. The preparation of each sample before imaging was conducted in the preparation chamber to maintain the best possible vacuum in the STM chamber. There are three methods to clean the tips or samples: electron bombardment, argon-ion sputtering and annealing. Electron bombardment is generally used to clean the tip, which will be discussed in section 2.3.2. The low temperature annealing (lower than 650 °C) for the sample is achieved by indirect heating via a ceramic heater situated in the vertical manipulator. The high temperature annealing can be obtained by direct resistive heating of the samples. For the

deposition of the molecules, a Quad Dopant Source from molecular beam epitaxy (MBE) Kompowerten with water cooling is used. The molecules in each of the four Knudsen cells were heated by a PID electronic controller and a thermal couple mounted inside the cell to precisely control the deposition temperature. The surface structure of the sample was systematically characterized by LEED. The base pressure in the preparation chamber is kept below 2×10^{-10} mbar.

After the preparation, the sample or tip can be transferred to the STM chamber. The STM chamber includes the STM head with the piezoelectric elements and a sample stage, as shown in Figure 2.2 (b). The pressure in the STM chamber is kept at about 5×10^{-11} torr.

The UHV in the preparation and STM chamber is initially obtained by a turbo pump followed by baking the whole chamber at the maximum temperature of 125°C. After that, the UHV is kept stable by ion pump and titanium sublimation pump (TSP) during the sample preparation.

2.2 Low Energy Electron Diffraction (LEED)

2.2.1 The Principle of LEED

To monitor the modification of the surface reconstruction during the graphene preparation on 6H-SiC substrate, low energy electron diffraction (LEED) was used in this experiment. The LEED optics are situated in the preparation chamber of the RT-STM, as shown in Figure 2.4 and Figure 2.5. LEED is a widely used technique to determine the surface structure of crystalline materials in surface science. In principle, a beam of electrons of a well-defined low energy (typically in the range 20 - 200 eV) is incident on the single crystal sample with a well-ordered structure. After that, the inelastically scattered electrons are screened out by the hemispherical concentric grids. Most electrons are elastically scattered (Bragg Scattering) by the atomic planes of the crystal and are accelerated to the phosphor screen where they appear as

diffraction spots. The diffraction pattern is a direct picture of the reciprocal lattice of the surface.

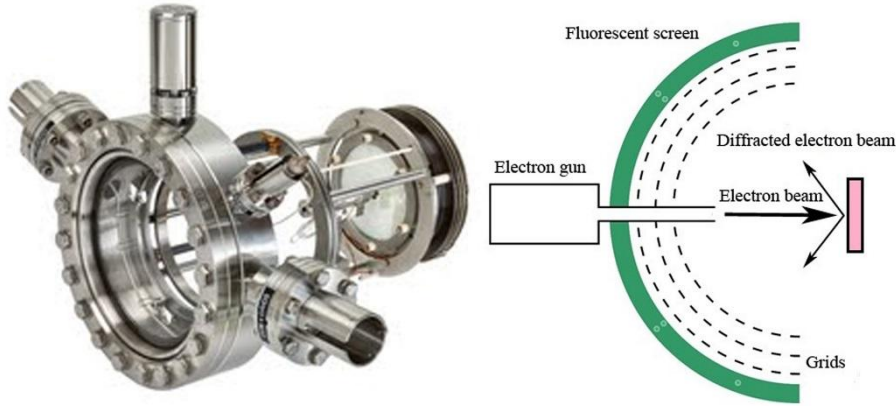


Figure 2.5 LEED set-up used in this experiment and the diagram of a LEED optics apparatus.

2.2.2 The Basic Theory of LEED

For low-energy electrons, the interaction between the solid and electrons is especially strong, giving rise to the high surface sensitivity of LEED. Upon penetrating the crystal, primary electrons will lose kinetic energy due to inelastic scattering processes such as electron-electron interactions as well as plasmon-phonon excitations. Because the detailed principle of the inelastic processes is insignificant in this case, they are commonly treated by assuming an exponential decay of the primary electron beam intensity, I_0 , in the propagation direction:

$$I_d = I_0 \times e^{-d/\Lambda_E} \quad (2.11)$$

Where, d is the penetration depth and Λ_E denotes the inelastic mean free path, defined as the distance an electron can travel before its intensity has decreased by the factor $1/e$. The electronic mean free path depend on the energy, it is relatively independent of the material. The mean free path turns out to be minimal ($5\text{--}10 \text{ \AA}$) in the energy range of low-energy electrons (20~200 eV). This effective attenuation means that

only a few atomic layers are sampled by the electron beam and as a consequence the contribution of deeper atoms to the diffraction progressively decreases. This is the reason that LEED is sensitive to the lattice structure on sample surface.

Kinematic diffraction is defined as the case where electrons impinging on the ordered crystal surfaces are elastically scattered only once by that surface. In this theory, the electron beam is considered to be a plane wave with a wavelength according to De Broglie's hypothesis:

$$\lambda = \frac{h}{\sqrt{2mE}} \quad (2.12)$$

Where, m is the mass of electron, h is the Planck constant, E is the electron kinetic energy. The simple model for the electrons scattering by the atoms in the topmost layer of a solid shown in Figure 2.6. In which, the electron beam incident normal to the surface from the vacuum above.

If it is considered that the backscattering from the wave front of two adjacent atoms forms a definite angle θ with the surface normal, it is clear that there is a "path difference" d in the distance, the radiation has to travel from the scattering centers to a detector (which is effectively at infinity)-this path difference is best illustrated by considering two "ray paths" such as the black traces in Figure 2.6.

The path difference is $a \sin \theta$ and it must be equal to an integral of the wavelength of the constructive interference that occurs when the scattered beams eventually encounter and interfere at the detector, i.e.

$$d = a \sin \theta = n\lambda \quad (2.13)$$

where, λ = wavelength, n = integer (...,-1,0,1,2,...)

For two isolated scattering centers, the diffracted intensity varies slowly between zero (complete destructive interference; $d = (n + \frac{1}{2})\lambda$) and its maximum value (complete constructive interference; $= n\lambda$) with a large periodic array of scatters. However, the

diffracted intensity is only meaningful when the Bragg condition $a \sin \theta = n\lambda$ is exactly satisfied.

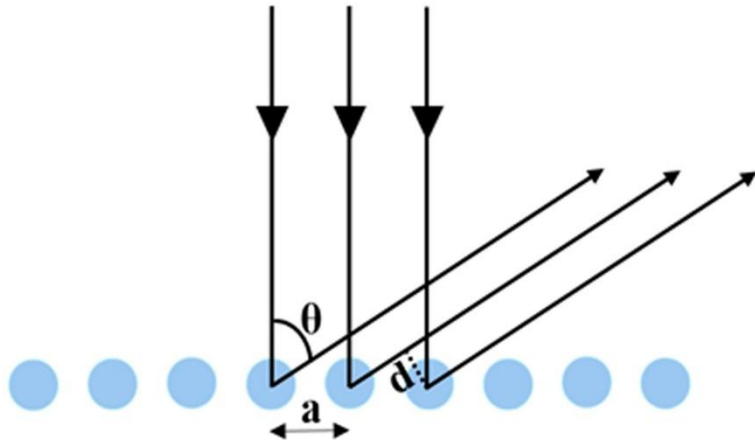


Figure 2.6 Model for the electron scattering by the atoms in the topmost layer of a solid.

The interaction between the scatters in the surface and the incident electrons is most conveniently described in reciprocal space. In three dimensions the original reciprocal lattice vectors are related to the real spatial lattice $\{\mathbf{a}, \mathbf{b}, \mathbf{c}\}$ in the following way[8]:

$$\mathbf{a}^* = \frac{2\pi \mathbf{b} \times \mathbf{c}}{\mathbf{a} \cdot (\mathbf{b} \times \mathbf{c})}; \quad \mathbf{b}^* = \frac{2\pi \mathbf{c} \times \mathbf{a}}{\mathbf{b} \cdot (\mathbf{c} \times \mathbf{a})}; \quad \mathbf{c}^* = \frac{2\pi \mathbf{a} \times \mathbf{b}}{\mathbf{c} \cdot (\mathbf{a} \times \mathbf{b})}.$$

For an incident electron with the wave vector $k_0 = 2\pi/\lambda_0$ and scattered wave vector $k = 2\pi/\lambda$, the constructive interference and diffraction condition of the scattered electron waves are determined by the Laue condition:

$$k - k_0 = G_{hkl} \quad (2.14)$$

where (hkl) is a set of integers and is a vector of the reciprocal lattice.

$$G_{hkl} = h\mathbf{a}^* + k\mathbf{b}^* + l\mathbf{c}^* \quad (2.15)$$

The magnitudes of the wave vectors are unvaried, i.e. $|k_0| = |k|$, because only elastic scattering is considered. The mean free path of the low-energy electrons in the crystal is only a few angstroms, therefore, only the first few atomic layers contribute to the diffraction.

This means that there are no diffraction conditions in the direction normal to the sample surface. As a consequence, the reciprocal lattice of a surface is a 2D lattice with rods extending perpendicular from each lattice point. The rod can be described as an area where the reciprocal lattice points are infinitely dense. Therefore, in the case of diffraction from a surface equation (2.14) reduces to the 2D form[9]:

$$k^{\parallel} - k_0^{\parallel} = G_{hk} = ha^* + hb^* \quad (2.16)$$

where a^* and b^* are the primitive translation vectors of the 2D reciprocal lattice of the surface, $k^{\parallel}, k_0^{\parallel}$ represent the components of the reflected and incident wave vector parallel to the sample surface, respectively. a^* and b^* are related to the real space surface lattice in the following way: $a^* = \frac{2\pi b \times n}{|a \times b|}$; $b^* = \frac{2\pi n \times a}{|a \times b|}$. The Laue condition equation (2.16) can readily be visualized using the Ewald sphere construction.

Figure 2.7 (a) shows a brief description of this principle: The wave vector k_0 of the incident electron beam is plotted such that it terminates at a reciprocal lattice point. The Ewald sphere is a sphere with radius $|k_0|$ and origin at the center of the incident wave vector. By construction, every wave vector centered at the origin and the end with the intersection between the rod and the sphere will satisfy the Laue condition and thus represent an allowable diffracted beam. A clear (1×1) diffraction pattern of the 6H-SiC (0001) substrate used in this experiment is shown in Figure 2.7(b). For the case of an overlaying superstructure on a substrate surface, if the LEED pattern of the underlying substrate surface is known, the spots due to the superstructure can be identified as the extra spots. Specifically, the LEED patterns of the superstructures in the process of graphene preparation on SiC will be shown in Chapter 3.

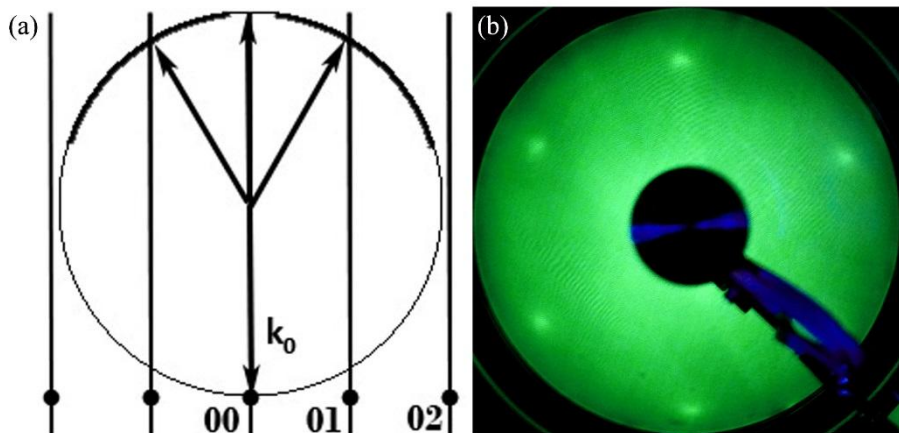


Figure 2.7 (a) Ewald's sphere construction for the case of normal incidence of the primary electron beam. The diffracted beams are indexed according to the values of h and l . (b) The LEED pattern of the clean 6H-SiC (0001) surface.

2.3 Tungsten (W) Tip Preparation

In the STM measurement, a good tip is a crucial prerequisite to obtain the high quality STM images and spectroscopic curves. Thus, the tip preparation is an essential experimental part in STM.

Different materials can be used to fabricate the STM tips. One of the popular materials is Pt/Ir, because Pt is slow to oxidise and a Pt/Ir tip is easily fabricated by simply cutting the wire with cutters or a pair of scissors. However, Pt/Ir tips are of limited use because of the low success rate to reach the atomic resolution and the unstable mechanical property due to the poorly structured tip apex. Tungsten is a commonly used material in STM because it is very hard and mechanically stable. More importantly, it has a high and smooth DOS[10]. Even though tungsten is an oxidizable material in air and it becomes superconducting below 10 mK, our experiment was conducted under UHV at room temperature, the tungsten tip reproducibly obtains atomic-scale images and precise spectroscopic data.

2.3.1 Fabrication of Tungsten Tip by Alternating Current

Generally, the tungsten tips are prepared by electrochemical etching and it involves a redox reaction between the solid tungsten and the hydroxide ion in solution. In practice, a tungsten wire is immersed in an aqueous solution of sodium hydroxide (Na^+ ; HO^-) or potassium (K^+ , HO^-) and acts as an anode. A second electrode, a platinum or nickel wire, is also immersed in this solution and an opposite potential is applied (see Figure 2.8).

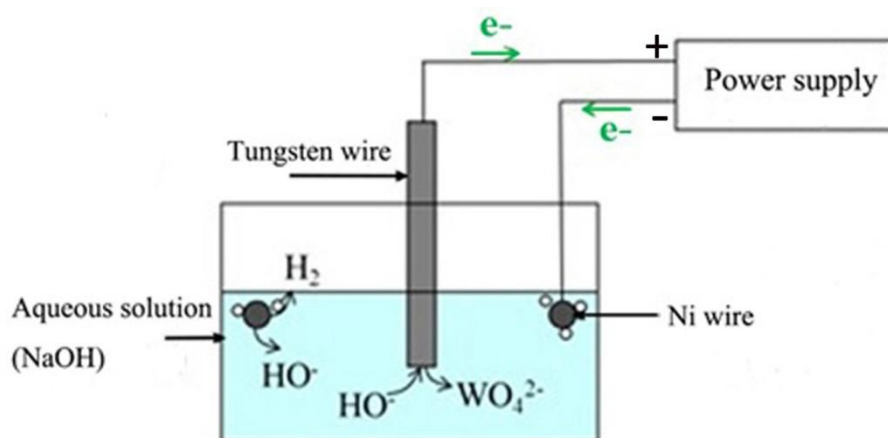
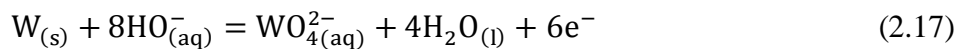


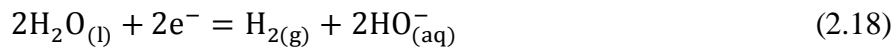
Figure 2.8 The schematic diagram of electrochemical etching tungsten tips. A tungsten wire is immersed in an aqueous solution of sodium hydroxide, to which is applied a positive potential. A ring-shaped nickel wire (cathode electrode) is used, allowing the more symmetrical etching possible.

The two reactions are as below:

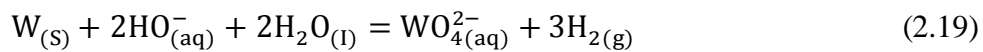
At the tungsten wire (anode):



Against at the nickel electrode (cathode):

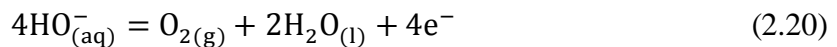


The complete redox reaction is:



As indicated by the equation (2.17), the tungsten metal becomes oxidized tungstates (VI) ions dissolving into the solution, which explains the etching phenomenon. At the nickle electrode, there is a formation of hydrogen gas, so that small bubbles will be generated subsequently. The etching rate determined by the distance between the nickle wire and the tungsten electrode and their respective orientations. To obtain a uniform etching speed around the tungsten wire, a nickel electrode ring is preferred than a straight wire, and it is better to place tungsten wire in the center of this ring.

It is possible to fabricate tungsten tip under both alternating current (AC) and direct current (DC) power supply. Etching under AC is traditionally used in my team, in which tungsten wire acts alternately as anode and cathode, as shown in Figure 2.9. At the beginning, a cylindrical tungsten wire of 0.25mm diameter is merged in an aqueous solution of sodium hydroxide, keeping a few millimeters of wire in the solution. After that, the tungsten wire is subjected to a positive pulse (Figure 2.9 (b)), the pulse duration is 0.6s. The tungsten reacts with hydroxide ion and tungstates ions are formed, according to reaction (2.17). Tungsten wire is being etched. At the nickel electrode, water reduces and hydrogen gas is generated. After that, a negative pulse is subjected (Figure 2.9 (d)), water reduces and hydrogen gas forms around the tungsten wire. These dihydrogen bubbles will rise to the surface and explode. The bubbles generate convection currents in the solution near the tungsten wire, which promotes the dispersion and renewal of tungstates ions created during the etching, therefore allowing a homogeneous etching of the immersed tungsten wire. While at nickle electrode, hydroxide ions are consumed and oxygen gas is produced (see equation (2.20))[11].



The interval between two pulses is 2.5s and no chemical reactions take place. The pulse cycle is repeated many times until the power is manually turned off. This point is determined by the residual current ~10mA for a 0.25 mm diameter tungsten wire

and corresponds to $\sim 0.5\text{ mm}$ of conical W wire in the solution. On average, the tip etching lasts about 45 minutes. After that, the tip is washed in distilled water, the length and shape of the tip is checked by an optical microscope.

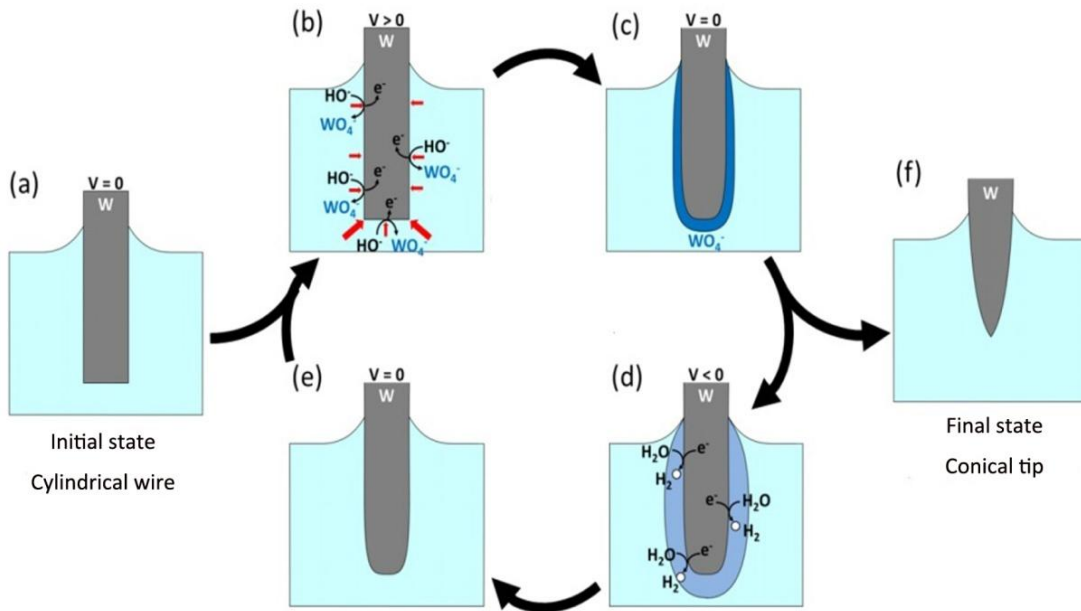


Figure 2.9 The principle of etching tungsten by AC pulse. (a) A tungsten wire is dipped in a sodium hydroxide solution; (b) When a positive potential is applied to the wire, the hydroxide ions oxidize the tungsten into water-soluble tungstates. The etching rate is faster at the angular points than on the flat surfaces; (c) Tungstate ions are produced near the wire; (d) The potential applied to the wire becomes negative. The water is then reduced into hydrogen gas that disperses tungstate ions; (e) Ideal tungsten wire is in contact with the sodium hydroxide solution. This cycle is repeated many times until the power is manually turned off; (f) A conically shaped tip is obtained.

2.3.2 The Thermal Treatment of Tungsten Tip

When the etched tungsten tip is placed in UHV in the preparation chamber, it is degassed by indirect heating at about 500°C for several hours to remove the contamination that cannot be removed by rinsing in water or ethanol. After that, the tip was further heated at higher temperature by electron bombardment. The aim is to remove the compounds left on the tip from the etching solution and oxide layer

(WO₃) formed during the etching. In the process of electron bombardment, the filament of an electron gun is placed about 1mm away from the tip. The electrons generated by the filament are accelerated by the high voltage applied to the tip. The effective heating of electron bombardment makes the high temperature available for less than one second. Thus, the electron bombardment time should be very short (about 30s) to avoid making the tip apex blunt[12]. After electron bombardment, the tip can be transferred to the STM chamber and used to image the sample surface.

2.4 Bibliography

- [1] G. Binnig and H. Rohrer. Scanning tunneling microscopy. IBM J Res Dev., 30: 355 (1986).
- [2] B. Chunli. Scanning tunneling microscopy and its application. New York: Springer-Verlag Berlin Heidelberg (2000).
- [3] C. J. Chen. Introduction to scanning tunneling microscopy. New York: Oxford University Press (1993).
- [4] Available from www2.fkf.mpg.de.
- [5] J. Bardeen. Tunnelling from a many-particle point of view. Phys. Rev. Lett., 6: 57 (1961).
- [6] S. B. Lei and S. D. Feyter. STM, STS and bias-dependent imaging on organic monolayers at the solid-liquid interface, in STM and AFM Studies on (Bio)molecular Systems: Unravelling the Nanoworld. Springer Berlin Heidelberg: 269-312 (2008).
- [7] J. A. Kubby and J. J. Boland. Scanning tunneling microscopy of semiconductor surfaces. Surf. Sci. Rep., 26: 61-204 (1996).
- [8] C. Kittel. Introduction to solid state physics. US: John Wiley (2005).
- [9] M. A. V. Hove, W. H. Weinberg and C. M. Chan. Low-energy electron diffraction. New York: Springer Berlin Heidelberg (1986).

- [10] H. Ness and F. Gautier. The electronic structure and stability of transition metal nanotips. *I. J. Phys.: Condens. Matter.*, 7: 6625-6640 (1995).
- [11] B. Rogez. Excitation électrique locale de nanostructures plasmoniques par la pointe d'un microscope à effet tunnel. PhD, Université Paris Sud -Paris XI (2014).
- [12] A. S. Lucier. Preparation and characterization of tungsten tips suitable for molecular electronics studies. Master of Science, McGill University (2004).

Chapter 3

Epitaxial Graphene Grown on 6H-SiC

Table of Contents

3.1 Introduction.....	44
3.2 Experimental Procedure of Epitaxial Graphene Grown on 6H-SiC(0001)...	44
3.3 Topography and Electronic Properties of Graphene on 6H-SiC(0001).....	50
3.3.1 Topography and Electronic Properties of the Buffer Layer.....	50
3.3.2 Topography and Electronic Properties of Monolayer Graphene on 6H-SiC (0001).....	55
3.3.3 Topography and Electronic Properties of Bilayer Graphene on 6H-SiC (0001).....	57
3.4 Epitaxial Graphene Grown on 6H-SiC(000-1).....	61
3.4.1 Experimental Procedure to Grow Graphene on 6H-SiC (000-1).....	61
3.4.2 Topography of Graphene on 6H-SiC (000-1).....	61
3.4.3 Electronic Properties of Graphene on 6H-SiC (000-1).....	69
3.5 Conclusions.....	72
3.6 Bibliography.....	73

3.1 Introduction

Since graphene was first prepared by the scotch tape method in 2004[1], its extraordinary two-dimensional gas phase properties, and promising applications in next-generation nano-scaled electronics have attracted tremendous interest from the researchers[2-4]. At present, graphene can be fabricated in a variety of mechanical, chemical, and physical ways. For example, chemically synthesis[5-7], reduction of graphene oxide[8], chemical vapor deposition (CVD) on a Ni surface[9], cutting a carbon nanotube[10, 11], epitaxial growth on the hexagonal SiC surface[12], and so on. Different methods have their own advantages and disadvantages. Among them, hexagonal SiC has the same crystal symmetry as graphene and it is easier to obtain a large area clean graphene sheet in ultra high vacuum (UHV)[13]. Both the Si-terminated face and C-terminated face of SiC were used to prepare graphene. Graphene grows on the Si face with layer-by-layer growth mode[13], so that this method can precisely control the number of graphene layers; while on C face, it is facile to fabricate a number of graphene layers at once, however, large area of monolayer graphene is difficult to achieve, because on C face, the Si sublimation is much more rapidly than that on Si face, and a 3-dimensional growth mode of graphene is preferred[14]. In our study, single-layer graphene on buffer layer are more favorable to explore its interactions with organic molecules. Graphene on the C face of SiC was also grown to make a comparison with the result of graphene on the Si face. In this chapter, the detailed process of epitaxial graphene growth on SiC, and its electronic properties will be described.

3.2 Experimental Procedure of Epitaxial Graphene Grown on 6H-SiC (0001)

In my experiment, graphene was prepared by sublimating Si atoms from the rich Si surface of 6H-SiC (0001) at high temperature in UHV. Low Energy Electron

Diffraction (LEED) was used to observe the surface structure during the whole process.

First, a piece of 6H-SiC (0001) wafer ($9\text{mm} \times 4\text{mm}$) was flashed at 1100°C for a few minutes until a clear (1×1) LEED pattern was obtained (see Figure 3.1 (a) and (b)). If a clean surface is not obtained immediately, depositing Si atoms from a Si source at 1200°C on the sample surface before flashing again is necessary. The distance between the Si source and sample was around 4 cm. Generally, several cycles of depositing and flashing are needed. Often a $(\sqrt{3} \times \sqrt{3})$ reconstructed SiC (0001) surface is obtained during these cycles (see Figure 3.1 (c) and (d)).

Second, to obtain the (3×3) rich Si surface, further evaporation of the Si source on the 6H-SiC (0001) sample is required. Usually, 8 min is enough (see Figure 3.1 (e)). The SiC crystallographic structure in a perspective view is shown in Figure 3.1 (f). There is a full Si adlayer on top of the bulk-like terminated Si atoms, and Si tetramers chemically adsorb on the adlayer with an angle of 60° . The adatoms protruding from the surface are positioned in the T4 sites (hollow) of the three-fold coordinated silicon atoms, and contribute to the (3×3) superstructure in the LEED pattern. The (3×3) reconstruction is a saturated surface phase; only the surface-protruding adatom has a dangling bond in the unit cell, all the other Si atoms are fully saturated with optimized Si-Si bonds. The optimization is mainly ascribed to the rotation of some atoms around adatom or some buckling in the adlayer and top bulk layer[15]. Since the (3×3) saturated reconstruction created many steps on the surface, it is favorable for the atomic diffusion and homoepitaxial growth[16]. At this point, the clean (3×3) surface was checked by STM. The atomic-scale STM image was presented in Figure 3.2. There are some vacancies on the surface, it is caused by the hydrogen atoms of the remaining water in the chamber. To obtain the uniform graphene, the vacancies should be less than 5%. In addition, the (3×3) rich Si surface shows a triangular lattice in STM image, in agreement with the atomic structure in Figure 3.1 (f).

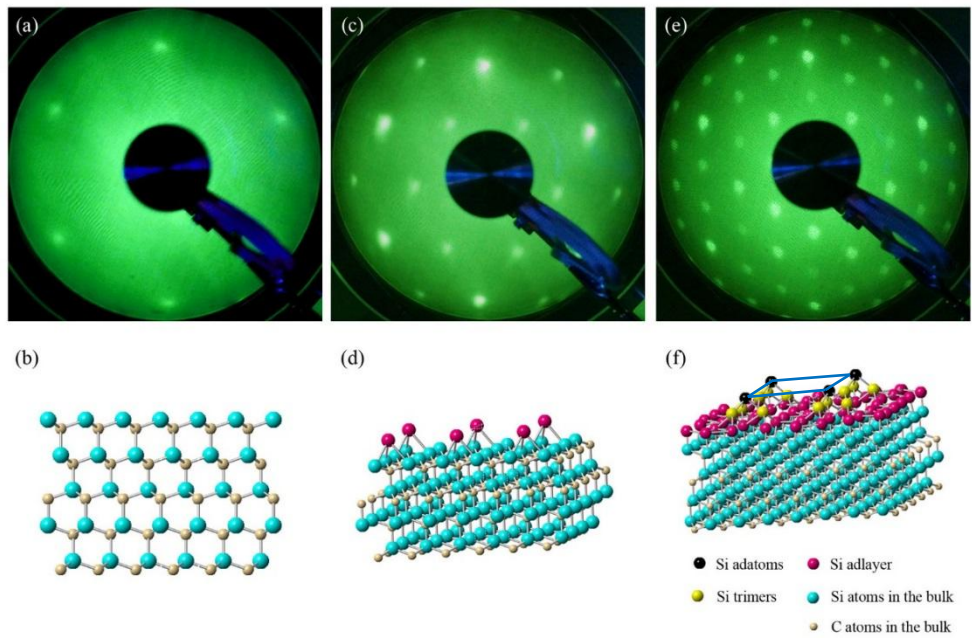


Figure 3.1 The LEED pattern and corresponding structural models of the surface reconstruction of the 6H-SiC (0001) during the preparation of (3×3) rich Si surface. (a) The LEED pattern for the (1×1) 6H-SiC (0001) at 75 eV; (b) The structural model of the (1×1) 6H-SiC (0001) in the side view. The blue balls represent the Si atoms, the gray balls represent the C atoms; (c) The LEED pattern for the $(\sqrt{3} \times \sqrt{3})$ 6H-SiC (0001) at 83 eV; (d) The structural model of the $(\sqrt{3} \times \sqrt{3})$ 6H-SiC (0001) reconstruction in a perspective view; (e) The LEED pattern for the (3×3) surface reconstruction of the 6H-SiC (0001) at 75 eV; (f) The structural model of the (3×3) reconstruction of the 6H-SiC (0001) in a perspective view.

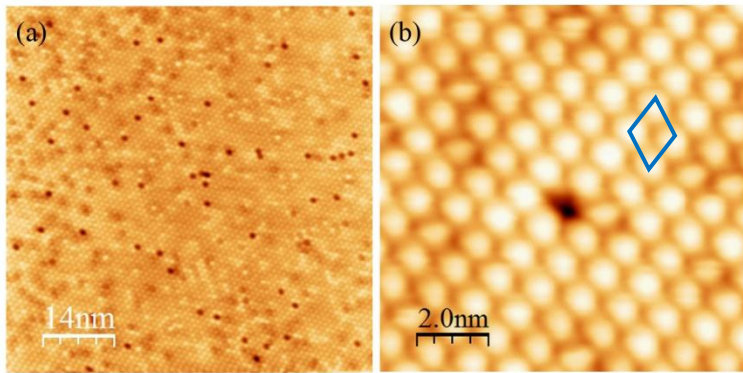


Figure 3.2 Atomic-scale STM image of (3×3) SiC reconstruction surface. (a) $70\text{nm} \times 70\text{nm}$, tunneling condition: $V=-2.5\text{V}$, $I=0.2\text{nA}$, the vacancies should be less than 5%; (b) $10\text{nm} \times 10\text{nm}$, tunneling condition: $V=-2.5\text{V}$, $I=0.2\text{nA}$.

Third, the (3×3) SiC sample was flashed at 1150°C to desorb part of top Si atoms, and the $(\sqrt{3} \times \sqrt{3})$ surface reconstruction was formed (see Figure 3.1 (e)). It has been determined that there is only one Si protruding atom in the $(\sqrt{3} \times \sqrt{3})$ superstructure unit cell, and the adatom resides on the T4 site of the bulk terminated Si atoms with three optimized Si-Si bonds[15, 17] (see Figure 3.3 (b)). The bond optimization also results in some buckling of the top bulk C layer and neighboring Si sublayer underneath[18].

Fourth, the $(\sqrt{3} \times \sqrt{3})$ SiC sample was flashed at 1250°C to continue sublimating surface Si atoms until the $(6\sqrt{3} \times 6\sqrt{3})$ phase developed. It corresponds to the six satellite spots which are rotated 30° with respect to the SiC $(0, 1)$ diffraction spot (see Figure 3.3 (c)). The $(6\sqrt{3} \times 6\sqrt{3})$ reconstruction is an intermediate carbon layer before the graphene layer is formed, it is the so called zero layer graphene or buffer layer. There are two types of non-equivalent C atoms in the buffer layer, one is still bond to the Si atoms in the substrate, and three C atoms from a sp₂ bonded layer, which occupies about one-third of all the atoms in the buffer layer, while the last one is free from the substrate and only bonds with three sp₂ C atoms[19] (see Figure 3.3 (d)).

Fifth, a higher temperature of 1325 °C was used to flash the $(6\sqrt{3} \times 6\sqrt{3})$ SiC sample to release all the C atoms in the buffer layer from the substrate and convert them into a free graphene layer (monolayer graphene). The LEED pattern was checked from time to time until it showed the clear graphene spots which are located in the center of the buffer layer satellite spots (see Figure 3.3 (e)). According to the LEED pattern, graphene shows same orientation as the buffer layer, so it is rotated 30° with respect to the SiC lattice direction. In addition, the buffer layer satellite spots have a similar intensity as the graphene spots. It has been demonstrated with the growth of an additional graphene layer, that a new buffer layer is generated from the underlying SiC substrate [20] (see Figure 3.3 (f)).

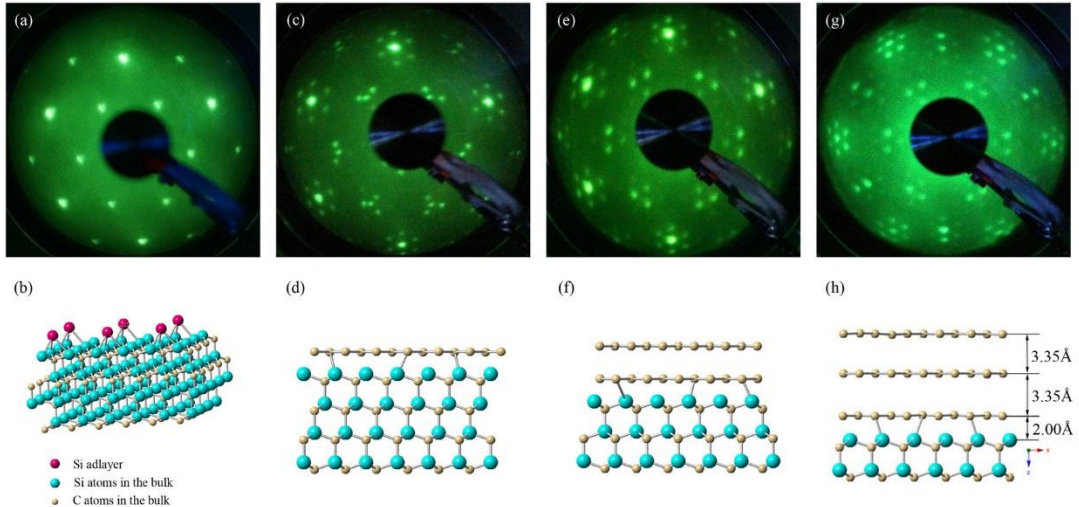


Figure 3.3 The LEED pattern and corresponding structural model of 6H-SiC (0001) during growing graphene on rich Si surface. (a) LEED pattern for the $(\sqrt{3} \times \sqrt{3})$ 6H-SiC (0001) at 83 eV; (b) Structural model of the $(\sqrt{3} \times \sqrt{3})$ 6H-SiC reconstruction in a perspective view; (c) LEED pattern for the $(6\sqrt{3} \times 6\sqrt{3})$ reconstruction at 104 eV; (d) Structural model of the $(6\sqrt{3} \times 6\sqrt{3})$ 6H-SiC reconstruction in the side view²; (e) LEED pattern for (1×1) monolayer graphene on 6H-SiC (0001) at 106 eV; (f) Structural model of the monolayer graphene on 6H-SiC (0001) in the side view; (g) LEED pattern for the bilayer graphene on 6H-SiC (0001) at 135 eV; (h) Structural model of the bilayer graphene on 6H-SiC (0001) in the side view.

Even though the rich Si surface facilitates the growth of graphene, bilayer graphene can also be found locally. The LEED pattern of bilayer graphene is shown in Figure 3.3 (g), the graphene spots intensity are a little stronger than the buffer layer and SiC spots. The structure of bilayer graphene can be seen in Figure 3.3 (h). With the second graphene layer formed, the buffer layer underneath was also renewed. The average distance between buffer layer and SiC substrate is about 2.0 Å, while two graphene layers are arranged on top of buffer layer by van der Waals force, the distances between each other are 3.35 Å. The detailed structure and electronic properties of the buffer layer and graphene will be illustrated in the next section.

² The bulking of buffer layer is not shown in the structural model.

3.3 Topography and Electronic Properties of Graphene on 6H-SiC (0001)

3.3.1 Topography and Electronic Properties of the Buffer Layer

During the fabrication of graphene by Si sublimation from the 6H-SiC (0001) surface, a buffer layer forms before the characteristic graphene LEED pattern appears. STM studies[21, 22] and spectroscopic measurements[23] have demonstrated that the buffer layer is composed of a complete layer of C atoms, without any Si atoms in it. Within this layer, part of the C atoms are covalently bonded with Si atoms in the substrate. Figure 3.4 presents the atomic-scale STM images of the buffer layer at different bias voltages. When a high potential was used in panel (a) (-2.0V) and (b) (-1.5V), the STM images show a clear (6×6) honeycomb periodicity (with a ripple amplitude of 1.0 Å³ and width 1.9 nm) in the buffer layer, similar to the value reported in many other papers[24, 25]. The morphology can be understood that the lower DOS in the dark area arises from the C atoms that covalently bond with the substrate, and the higher DOS in the bright boundary of the hexagons is produced by the C atoms unbound to the substrate[19]. Under certain tip conditions, when the bias voltage was -1.0V, the bright four-atom diamond (in the black circle) and dark seven-atom hexagonal (in the blue circle) clusters can be clearly observed in the buffer layer, as shown in Figure 3.4 (c). According to the STM images, the atomic structure of the buffer layer can be deduced as the model in Figure 3.5. The buffer layer consists of numerous irregular hexagonal rings. The (6×6) unit cell is formed by the four-atom diamond clusters (black triangular lattice), in which, the C atoms are unbound to the substrate. Each seven-atom hexagonal cluster is shared by three irregular hexagonal rings. The repeating of seven-atom hexagonal clusters has a period of 32 Å (blue triangular lattice), and 30 ° rotation angle with respect to the (6×6)

³ The amplitude measured by STM also depends on the bias voltage and tip condition.

lattice, gives the $(6\sqrt{3} \times 6\sqrt{3})$ reconstruction lattice. The lattice parameters are consistent with the buffer layer LEED pattern in Figure 3.3 (c). The $(6\sqrt{3} \times 6\sqrt{3})$ lattice is mainly caused by the lattice difference between graphene honeycomb (2.46\AA) and SiC (3.08\AA), as well as the angle between buffer layer and substrate[26]. The buffer layer image at bias voltage of -0.5V (Figure 3.3 (d)) also shows the irregular hexagonal rings and dark valleys, whereas the lattice is not easy to be distinguished.

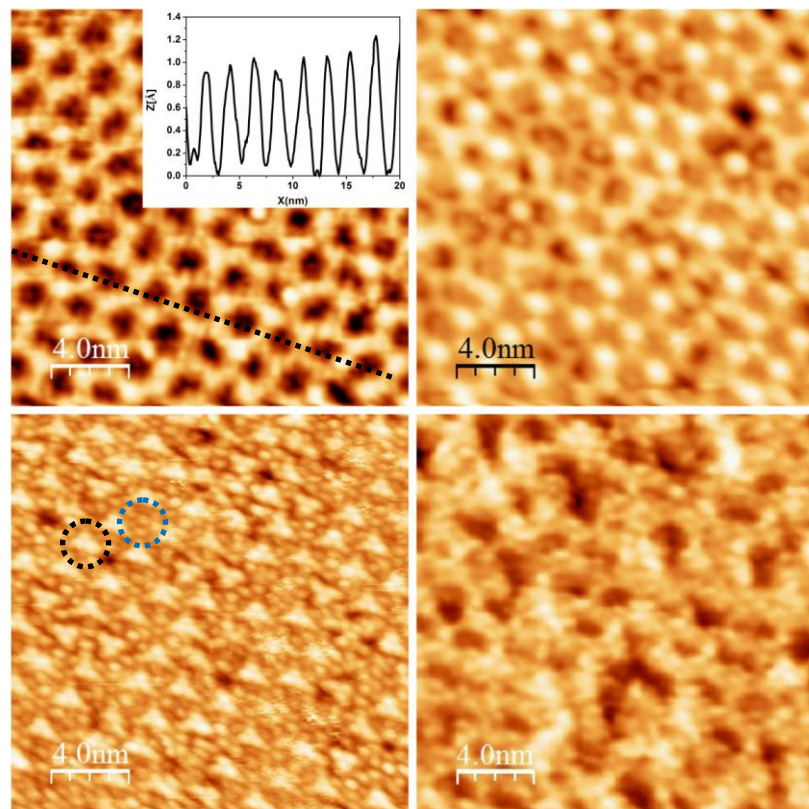


Figure 3.4 20nm×20nm STM topography of the buffer layer on 6H-SiC (0001). (a) Buffer layer topography at $V=-2.0V$, $I=0.2nA$; (b) Buffer layer at $V=-1.5V$, $I=0.2nA$; (c) Detailed structure of buffer layer at $V=-1.0V$, $I=0.2nA$; (d) Buffer layer at $V=-0.5V$, $I=0.2nA$ ⁴.

⁴ All STM images showed in my thesis are obtained at room temperature, the thermal drift is less than 1nm/ min. The measured value in the thesis is the real value after thermal drift calibration.

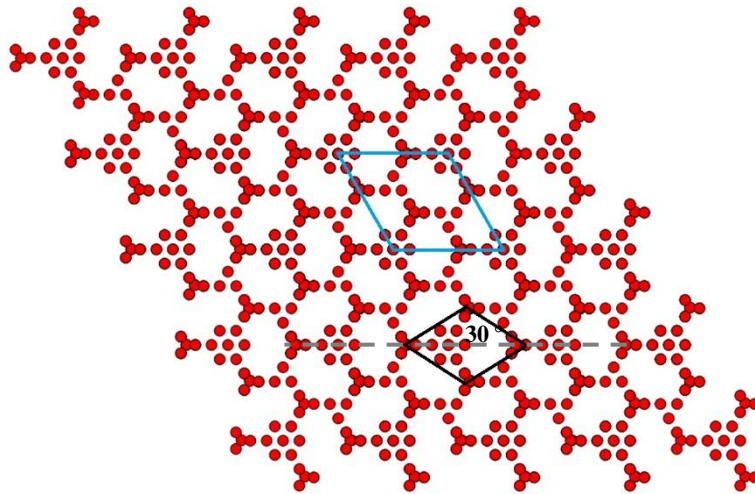


Figure 3.5 The atomic structure of the buffer layer with the $(6\sqrt{3} \times 6\sqrt{3})$ periodicity. The black triangular lattice represents the (6×6) lattice; the blue triangular lattice corresponds to the $(6\sqrt{3} \times 6\sqrt{3})$ lattice of buffer layer, the angle between the two lattices is 30° .

For the electronic properties of the buffer layer, Angle Resolved Photoemission Spectroscopy (ARPES) showed that buffer layer has the same σ -bonds as graphene, while the π -bonds are different[27]. The same σ -bonds are in the direction parallel to the substrate, where the C atoms form the sp^2 honeycomb reconstruction with a similar C-C bond length (1.42\AA). In the direction perpendicular to the substrate, the C atoms in the dark valley of irregular hexagons still bond to one Si atom in the substrate, while the C atoms at the boundary of the hexagons have localized π -bonds with the Si dangling bonds underneath. The area ratio of the two carbon components in the ARPES is a little bit less than half and both components contribute to the surface states of the $(6\sqrt{3} \times 6\sqrt{3})$ superstructure. The difference between the π -bonds is the consequence of the hybridization of localized π orbitals in the buffer layer and the Si dangling bonds[28]. It is agreed that the covalent bonding of the C atoms in the buffer layer and SiC substrate preserves the σ -bonds and breaks up the π -orbitals.

In my experiment, the electronic properties of the buffer layer were detected by scanning tunneling spectroscopy (STS) at different set-point bias voltages, as shown

in Figure 3.6. When the set-point bias is -2.0V, the differential conductance of the buffer layer is almost zero from -0.70V to +0.15V, a little different from the reported extremely low current in the range of ± 0.5 V with respect to the Fermi level[29]. When a lower set-point bias voltage is used (-1.5V), the non-conductance range decreases to (-0.39eV +0.18eV), and then descends to (-0.21eV +0.27eV) at the set-point bias voltage -1.0V. It is reasonable because the distance between the tip and sample varies with bias voltage, when the tunneling current is kept constant by the feedback loop. As the bias voltage decreases, the conductance increases because the tip approaches to the sample[30, 31]. When the set-point bias voltage is -0.5V, the non-conductance range of the buffer layer disappears (corresponding to the STM image in the Figure 3.4 (d)).

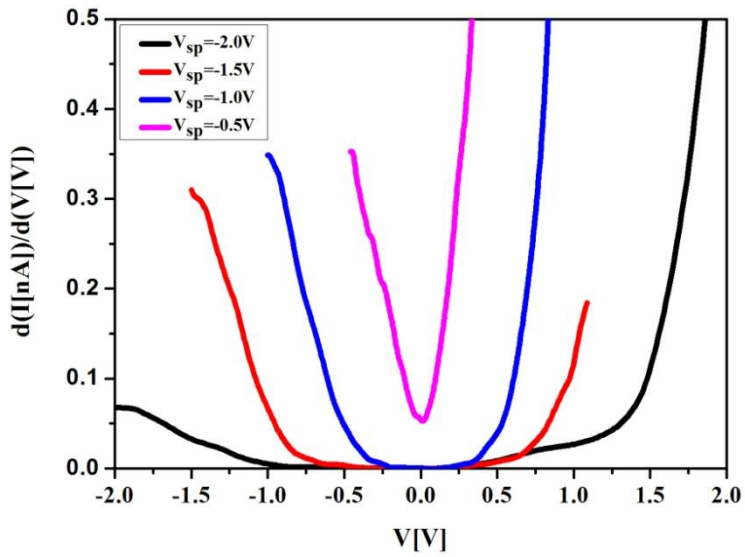


Figure 3.6 The dI/dV -V spectroscopy curves at the different set-point bias voltages. When the set-point bias voltage decreases, the band gap of the buffer layer becomes smaller. When the bias voltage is -0.5V, the band gap of buffer layer is zero, similar to the graphene π orbital.

3.3.2 Topography and Electronic Properties of Monolayer Graphene on 6H-SiC (0001)

Monolayer graphene is the second carbon layer above the buffer layer on 6H-SiC (0001) substrate, in which all the C atoms possess sp^2 hybridization and are free from the substrate, as presented in Figure 3.3 (f). With the growth of the monolayer graphene, a new buffer layer formed between the graphene and SiC substrate, the distance between the monolayer graphene and buffer layer is about 3.35 Å[32]. The atomic-scale topography and electronic structure of the monolayer graphene are shown in Figure 3.7. Because there is a weak electronic interaction between buffer layer and graphene, the morphology of graphene follows the buffer layer, like a carpet, the corrugation of the (6×6) superstructure (Moiré pattern) is obviously visible in the monolayer graphene STM image. The inset profile in Panel (a) reveals the amplitude of the monolayer ripple of about 0.62 Å (± 0.07 Å)⁵. The 2D Fast Fourier Transform (FFT) study of the total charge density in a large scale STM image indicates the graphene lattice (solid arrow) rotates 30° with respect to the (6×6) SiC reconstruction (dash arrow), which is consistent with the LEED pattern shown in Figure 3.3 (e). In the zoomed (25 Å × 25 Å) atomic-scale STM image (see Figure 3.7 (c)), the honeycomb structure of the monolayer graphene generated by the electron DOS along C-C bond network can be clearly observed, the measured bond length is about 1.40 Å.

As we all know, the free standing graphene can be considered as a zero-band gap semiconductor or semi-metal. Each C atom in the graphene has an sp^2 hybridized orbital, the valence band and conduction band intersect at the Dirac point, where both electrons and holes are massless. In my experiment, the differential conductance was measured to study the electronic properties of graphene on the 6H-SiC (0001) substrate (see Figure 3.7 (d)). In the dI/dV-V spectroscopy curve, the

⁵ The error estimation in the thesis is the standard deviation of a series of measurements.

Dirac point is seen as a dip which is located at about 0.40eV below the Fermi level, similar to the ARPES results[19]. The electron-doping of the graphene is most likely the consequence of the surface charge existing at the graphene-SiC interface (buffer layer)[12]. In the perpendicular direction, about two-thirds of the C atoms in buffer layer are free from the SiC, the Si dangling bonds in the substrate charges the buffer layer negatively and makes monolayer graphene n-doped. The doping extent is considered has nothing with the carrier concentration of the substrate, polytype or experimental procedure[19, 33]. Describing further the band structure of the monolayer graphene on 6H-SiC (0001), no band gap is observed in the spectroscopy curve in Figure 3.7 (d), in agreement with the DFT calculation[34] and ARPES results[35].

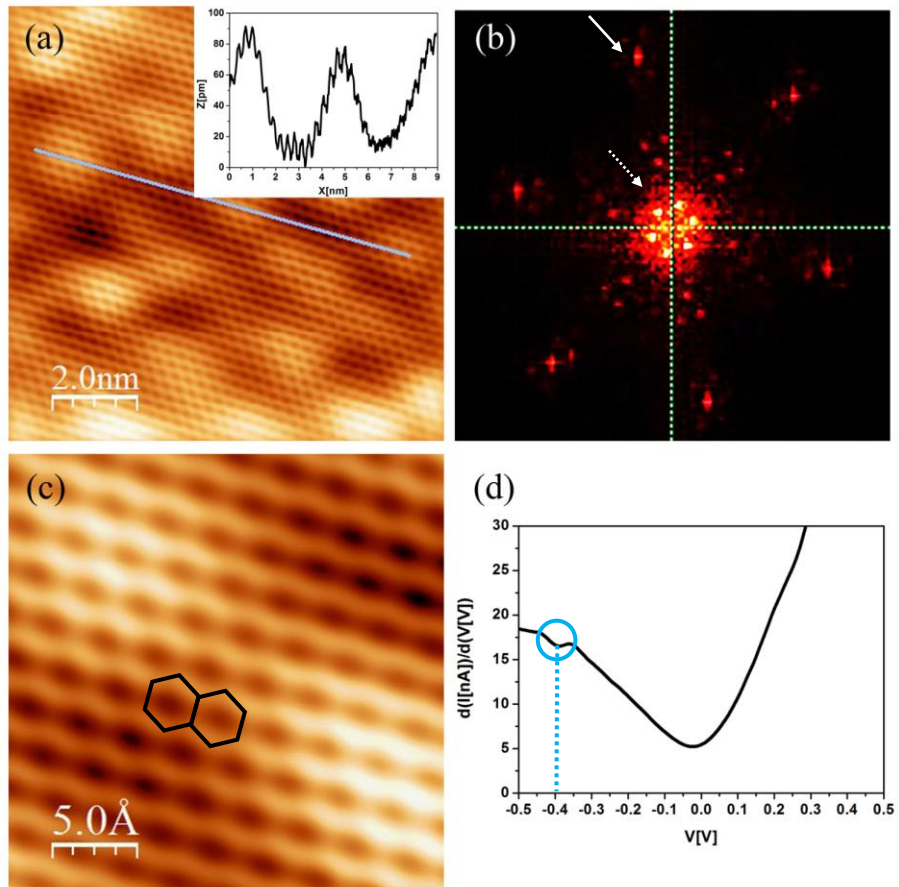


Figure 3.7 (a) ($10\text{nm} \times 10\text{nm}$) STM topography of the monolayer graphene on 6H-SiC (0001), the tunneling conditions: $V=-0.05\text{V}$, $I=0.2\text{nA}$. The profile indicates that the graphene morphology follows (6×6) superstructure corrugation (Moiré pattern), the amplitude of the graphene ripple is about 0.62\AA . (b) 2D Fast Fourier Transform (FFT) analyses for a large scale image of monolayer graphene. The solid arrow represents (1×1) graphene spots, the dash arrow is the (6×6) SiC reconstruction. The direction between the two superstructures is 30° ; (c) The zoomed ($25\text{\AA} \times 25\text{\AA}$) atomic-scale image of the monolayer graphene in Panel (a) clearly shows the hexagonal structure of the graphene; (d) The $(dI/dV)-V$ spectroscopy for the monolayer graphene, $V_{sp}=-0.03\text{V}$. The Dirac point (a minimum conductance value) shifts to 0.4eV below the Fermi level, and no band gap is detected.

3.3.3 Topography and Electronic Properties of Bilayer Graphene on 6H-SiC (0001)

In the process of growing graphene on SiC (0001), the number of graphene layers can be detected by different methods. In the LEED pattern, monolayer graphene spots

display a similar intensity to the surrounding ($6\sqrt{3} \times 6\sqrt{3}$) spots, while for the bilayer graphene, the graphene spots are brighter than the surrounding spots[19]. The graphene layer also can be distinguished by the ARPES because of the different electronic structures: Monolayer graphene has one linear π bond, while bilayer graphene shows two parabola π branches[19]. Atomic-scale STM image is also available to make a distinction between monolayer graphene (honeycomb lattice) and multilayer graphene (triangular lattice). In addition, the number of the graphene layer can be easily defined by the number of nodes in the dZ/dV spectroscopy[36]. Raman spectroscopy also can be used to distinguish monolayer and bilayer graphene by the shape of 2D peak caused by the different in-plane vibrations of the carbon atoms[37]. Moreover, the thickness of graphene can be estimated by Auger electron spectroscopy (AES).

In my experiment, growing graphene from the (3 \times 3) rich Si surface of 6H-SiC (0001) is favorable to the formation of a uniform monolayer graphene, however, there are localized areas of bilayer graphene, which occupies roughly 20% of the whole sample. In the atomic-scale STM image of bilayer graphene, the corrugation of the (6 \times 6) SiC reconstruction can also be seen (Figure 3.8 (a)). The morphology of the bilayer graphene follows the corrugation, and shows a ripple with an amplitude of 0.31Å ($\pm 0.02\text{\AA}$), which is a little lower than that of the monolayer (0.62Å). The 2D FFT pattern shows that bilayer graphene (solid arrow) has the same orientation as the monolayer, both rotate 30° with respect to the (6 \times 6) SiC reconstruction (dash arrow). In the zoomed (25Å \times 25Å) atomic-scale bilayer graphene image (see Figure 3.8 (c)), the triangular lattice with a unit cell of 2.50Å is resolved instead of the honeycomb lattice. Owing to a lower formation energy, the bilayer graphene has a Bernal stacking arrangement[38] (see the inset in Panel (c)). The honeycomb carbon sheets in the monolayer and bilayer graphene weakly interact via the 2p_z orbital overlap, resulting in a non-equilibrium between two adjacent atomic sites: the α -site atoms (red atoms) which are directly above a carbon atom in the first layer graphene and the β -site atoms

which are located in the hollow of a hexagonal ring in the underlying layer. Consequently, the electronic conductivity of the top graphene layer varies locally slightly, so that the atoms without neighbors appear higher than the others. Because the local DOS of the surface contributes mainly to the tunneling current, the C atoms located directly over the hollow of the hexagonal ring are brighter, while the other atoms are darker.

For the electronic structure of bilayer graphene, the Dirac point shifts to around 0.35eV below Fermi level (see Figure 3.8 (d)). The lower electron doping in bilayer graphene compared to the monolayer is the result of a reduced charge transfer from the substrate as the thickness increases[33]. In contrast to monolayer graphene, it was reported that the bilayer graphene has a small band gap at Dirac point (about 0.10eV). The reasons are linked to the buffer layer and the Bernal stacking of bilayer graphene[19, 27, 33]. The electron interactions between the buffer layer and first layer graphene result in an electrostatic asymmetry between the graphene layers. In addition, without electric field in the perpendicular direction, the free-standing bilayer graphene behaves as a semimetal (no band gap at the Dirac point), however, when the perpendicular electric fields are applied, variable band gap at the Dirac point is induced[39]. Hence, the inequivalent electronic influence of the interface between graphene and substrate is likely the primary cause of the band gap opening in bilayer graphene. In my experiment, the band gap at the Dirac point or Fermi level is not detected.

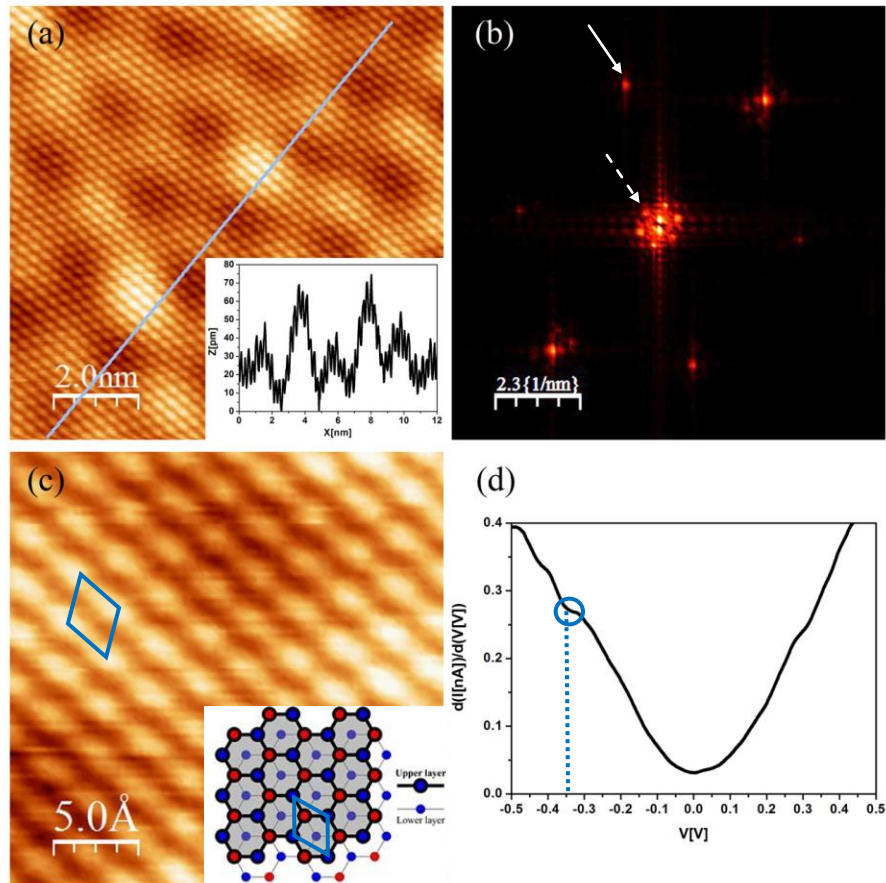


Figure 3.8 (a) The (10nm×10nm) STM topography of bilayer graphene on 6H-SiC (0001), tunneling conditions: $V=-0.5$ V, $I=0.2$ nA. The line profile indicates the bilayer graphene morphology also follows the (6×6) corrugation, the amplitude of the bilayer ripple is about 0.31Å. (b) The 2D Fast Fourier Transform (FFT) analysis of a large scale STM image of bilayer graphene. The solid arrow represents (1×1) graphene spots, the dash arrow is the (6×6) SiC reconstruction. The angle between the two superstructures is 30°. (c) The zoomed (25Å×25Å) atomic-scale image of bilayer graphene in Panel (a). The triangular structure of the bilayer graphene is clearly visible; the atomic structure of the bilayer graphene with Bernal stacking is displayed in the inset panel, only the C atoms which are located in the hollow of the hexagon rings contribute to the DOS⁶; (d) The $(dI/dV)-V$ spectroscopy for the bilayer graphene, $V_{sp} = -0.5$ V. The Dirac point (a minimum conductance value) shifts to 0.35eV below the Fermi level.

⁶ The C atoms in bilayer graphene obtained by RT-STM are not round because of the thermal drift as well as the possibly imperfect tip.

3.4 Epitaxial Graphene Grown on 6H-SiC (000-1)

At present, graphene has been widely grown on Si-terminated SiC substrate, because large-scale uniform electron-doped graphene can be obtained and the number of graphene layers can be precisely controlled. On the other hand, on the C-terminated face, neutral graphene with similar uniformity can be produced, but multilayer growth dominates, even though the carrier mobility of graphene on the C face is higher than that on Si face[13, 40]. In this section, the experimental procedure, topography and electronic properties of graphene grown on the C-terminated SiC substrate will be discussed.

3.4.1 Experimental Procedure to Grow Graphene on 6H-SiC (000-1)

In the experiment, the procedure of growing graphene on C-terminated 6H-SiC substrate under UHV condition was based on the reference[41]. A 10mm×4mm C-terminated 6H-SiC sample was cut from a SiC (000-1) wafer. After entry sample into the UHV chamber, it was cleaned by annealing at 750°C under a Si flux. Then the sample was flashed at 850°C until the (1×1) diffraction spots were clearly visible in the LEED pattern. After that, the (3×3) SiC reconstruction was obtained by heating sample at 1050°C. Further annealing at 1150°C led to the coexistence of (3×3) and (2×2) surface reconstruction. Continued warming of the sample at 1150°C for 20min produced a ring-like LEED pattern, indicating the formation of few layer graphene (FLG). This is different from the graphene LEED pattern on Si-terminated face (The intense spots which are rotated 30 °with respect to the SiC), the ring-like LEED pattern on C-terminated face reflects the multitude of graphene orientations.

3.4.2 Topography of Graphene on 6H-SiC (000-1)

A large scale image of graphene on 6H-SiC (000-1) substrate is displayed in Figure 3.9. Three graphene domains with different corrugations are separated by a series of

beads and a SiC step (step height: 2.07Å). The corrugation is a result of the different orientations between SiC interface and graphene as well as the rotations between graphene layers.

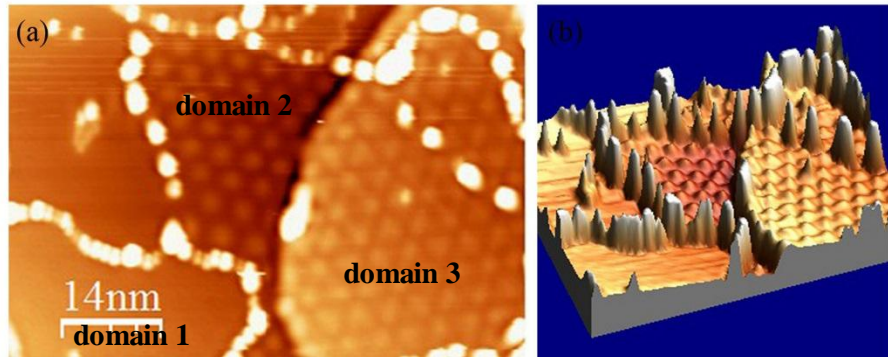
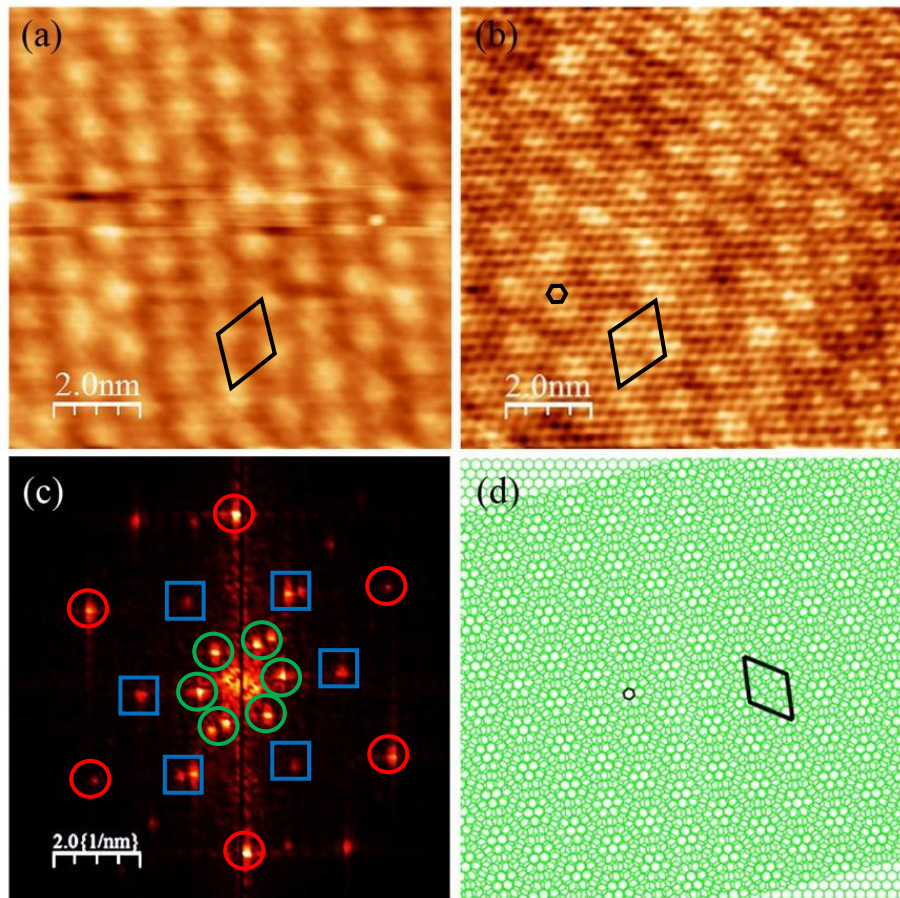


Figure 3.9 (a) A large scale image ($70\text{nm}\times50\text{nm}$) of different graphene domains separated by a series of beads and a SiC step, tunneling conditions: $V=-2.5\text{V}$, $I=0.2\text{nA}$; (b) Three-dimensional STM image of the different graphene domains on SiC (000-1).

To study the stacking of graphene on SiC (000-1) substrate in more detail, each graphene domain is zoomed. The topography of the first domain is represented in Figure 3.10. When the bias voltage is -2.5V (panel (a)), the (3×3) or (2×2) interface is expected to be seen, because graphene becomes transparent at high bias voltage. Panel (a) displays a triangular lattice with a period of 1.07nm, comprised of a single protrusion in each unit cell. Even though the super lattice periodicity is the same as the reported (3×3) SiC (000-1) reconstruction, the DOS of the super lattice at negative bias voltage is distinct from that of the (3×3) interface (a regular array of the hexagonal holes in each unit cell)[42]. In Panel (b), the atomic-scale graphene with a honeycomb lattice is seen at low bias voltage (-0.5V), which indicates the single graphene layer or the AA stacking between different graphene layers. The corrugation (Moiré pattern) in panel (b) represents the same periodicity and orientation with those at high bias voltage. The observation suggests the super lattice at high bias voltage is the corrugation instead of the (3×3) interface. There are

several graphene layers in the first domain and the corrugation is the result of the rotation between the top few graphene layers (only the topmost graphene layers contribute to the DOS in STM image). In the FFT pattern for (10nm×10nm) graphene image at -0.5V, the graphene lattice (red circles) is rotated 24° with respect to the Moiré pattern (green circles). We assume the Moiré pattern is the consequence of the azimuthal disorder between the top two graphene layers (AA'), then a 14° rotation leads to the triangular super lattice with a period of 1.06nm (in Figure 3.10 (d)), and the angle between graphene lattice and Moiré pattern is 23°, which are consistent with the experimental results. The hypothesis also matches with the calculation proposed by Varchon *et al*[43]. In the model in panel (d), the graphene layers are mainly in an AA stacking pattern; This orientation matches the honeycomb lattice of graphene obtained in the STM image. The STM image calculation based on the DFT calculation also reveals the honeycomb lattice of graphene at low bias voltage[44]. The analysis above demonstrates there are several graphene layers (more than two layers) in the first domain, and the Moiré pattern results from the azimuthal disorder of the top two graphene layers.

In the FFT pattern, the ($\sqrt{3} \times \sqrt{3}$) super lattice is also found (blue square) (graphene Brillouin zone). The six spots in blue squares also correspond to the graphene k-points resulting from the quantum interference composed of waves propagating in three directions. Because the first domain is confined by three boundaries (Figure 3.9), the super lattice might be caused by the electron backscattering near the edges[42, 45].



|Figure 3.10 (a) The topography of the first domain at high bias voltage, $V=-2.5\text{V}$, $I=0.2\text{nA}$; (b) Atomic-scale graphene image in the first domain at $V= -0.5\text{V}$; (c) FFT for the $(10\text{nm} \times 10\text{nm})$ graphene image at -0.5V . Because $k=1/\lambda_F$, the resolution in k -space is 0.10nm^{-1} . The red circles are graphene spots, the green circles represent the Moiré pattern, the blue squares are $(\sqrt{3} \times \sqrt{3})$ superlattice (graphene Brillouin zone); (d) The model of azimuthal disorder of two graphene layers (AA'). The angle between two graphene layers is 14° , the Moiré pattern has a period of 1.06nm , and the angle between Moiré pattern and graphene is 23° .

The zoomed STM image of the second domain at high bias voltage (-2.5V) presents a triangular corrugation with a period of 3.23nm instead of the (3×3) or (2×2) interface (Figure 3.11 (a)). There is a single protrusion in each unit cell. The atomic-scale graphene image at low bias voltage (-1.0V) (Figure 3.11 (b)) combines the triangular lattice with a Moiré pattern amplitude. This pattern has an amplitude of 0.44\AA , which

is in the range of (0.2-0.5Å) found by Varchon[43]. The angle between the graphene lattice (red circle) and Moiré pattern (blue square) is 31°, calculated from the FFT pattern in panel (c). The triangular lattice of graphene indicates the strong AB site asymmetry, similar to the Bernal stacking. Therefore, the Moiré pattern in the second domain probably results from the azimuthal disorder of the top four graphene layers: two sets of AB Bernal stacking graphene layers rotated by a certain angle (AB)(AB)'. The model in panel (d) indicates that a rotation of 5.1° gives rise to the triangular Moiré pattern with a period of 3.24nm. The angle between graphene lattice and Moiré pattern is 32°, which is coincident with the angle in the experiment. The strong AB site asymmetry in the top two graphene layers (AB)' is the origin of the triangular lattice in STM image at low negative bias voltage, agrees with the ab initio calculations in the reference[44].

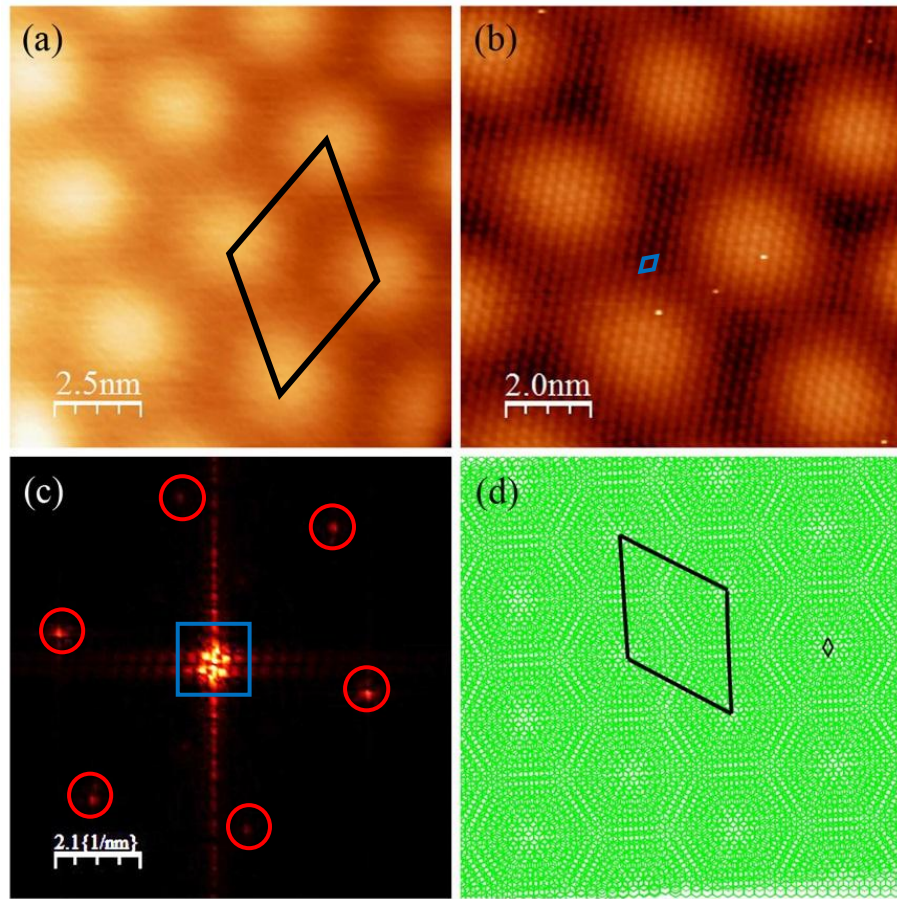


Figure 3.11 (a) (12.5nm×12.5nm) Topography of the second domain at high voltage, $V=-2.5V$, $I=0.2nA$; (b) Atomic-scale graphene image (10nm×10nm) in the second domain at $V= -1.0V$; (c) FFT pattern for the graphene image in panel (b). The red circles are graphene spots, the blue square represents the Moirépattern; (d) The model of azimuthal disorder of four graphene layers (AB)(AB)'. The angle between (AB) and (AB)' is 5.1° , the Moirépattern has a period of 3.24nm, the angle between the Moirépattern and graphene is 32° .

The zoomed (15nm×15nm) STM image for the third domain at -2.5V shows a quasi-triangular super lattice (period: 3.49nm) and triangular graphene lattice (0.25nm) (Figure 3.12 (a)), which has the same orientation in the zoomed (10nm×10nm) graphene image at -0.5V (Figure 3.12 (b)). Similar to the first and second domains, there are also a few graphene layers on 6H-SiC (000-1) substrate. The corrugation in panel (b) has an amplitude of 0.38Å and it shows the same

orientation with graphene lattice. The FFT pattern (Figure 3.12 (c)) also reflects the same orientation of the corrugation (blue square) and graphene lattice (red circles). Based on the azimuthal disorder of the graphene layers and the strong AB site asymmetry, the corrugation is the result of the turbostratic stacking⁷ of the top three graphene layers ABA', as shown in the model of panel (d). The angle between the A and A' graphene planes is 2.8 °, the corrugation exhibits a clear triangular lattice with a single protrusion in each unit cell, the period is 3.50 nm, and the angle between the corrugation and graphene lattice is zero. The model matches well with the experimental results. In addition, a larger triangular super lattice with a hexagon and two triangles in each unit cell is represented. It also exhibits the same orientation with graphene lattice with a period of 6.67 nm, which is the real Moiré pattern caused by the turbostratic stacking of ABA' graphene layers. It corresponds to the super lattice shown by the dash line in the STM image in panel (a), while it is not observed in FFT pattern because of the limited STM image size. Moreover, the ABA' stacking of graphene layers leads to the strong asymmetry of LDOS at the AB sites, which explains the triangular lattice of the graphene in the STM image.

⁷ The Moiré patterns are observed on multilayer graphene grown on C-terminated 6H-SiC. They arise from both the SiC interface and rotational stacking faults between the different graphene planes. The latter is the characteristic of a turbostratic stacking.

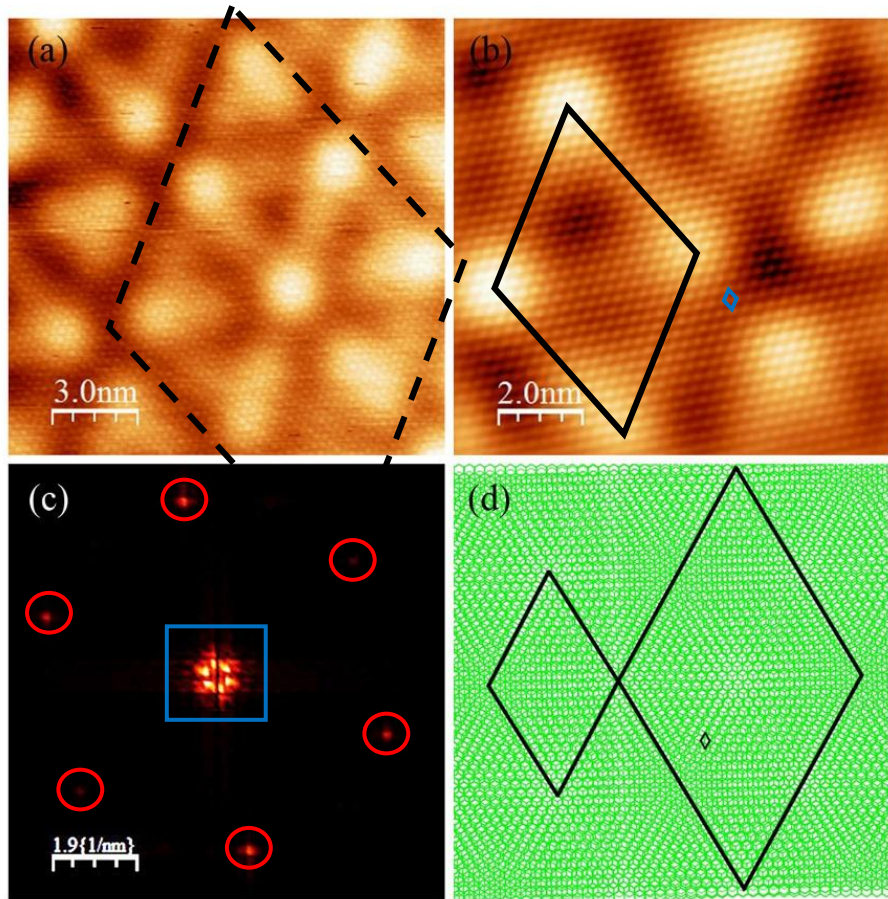


Figure 3.12 (a) ($15\text{nm} \times 15\text{nm}$) Topography of the third domain at high voltage, $V=-2.5\text{V}$, $I=0.2\text{nA}$; (b) Atomic-scale graphene image ($10\text{nm} \times 10\text{nm}$) in the third domain at $V=-1.0\text{V}$; (c) FFT pattern for the graphene image in panel (b). The red circles are graphene spots, the blue square represents the Moiré pattern; (d) The model of turbostratic stacking of three graphene layers (ABA'). The angle between A and A' plane is 2.8° , the corrugation has a period of 3.50nm , and it exhibits the same orientation with graphene lattice. The Moiré pattern is the large triangular lattice with a hexagon and two triangles in each unit cell, the period is 6.67nm .

Figure 3.13 shows the graphene with a Moiré pattern similar to the first domain. The period of the Moiré pattern is 1.00nm , with an amplitude of 4.61\AA , same as that in the first domain. Here, the graphene exhibits a triangular lattice (strong AB site asymmetry) at low bias voltage (-1.0V) instead of the honeycomb lattice (Figure

3.13 (a)). The angle between the graphene triangular lattice and the Moiré pattern is about 32° , shown by the FFT pattern (Figure 3.13 (b)). Based on the analysis above, the Moiré pattern probably arises from the AA'B stacking of the graphene layers with an angle of 14° between the A and A' graphene planes, as illustrated in Figure 3.13 (c). The Moiré pattern shows a period of 1.00nm and an angle of 32° with graphene lattice, which agrees with the experiment results. It confirms that the Moiré pattern comes from the azimuthal disorder of the top three graphene layers.

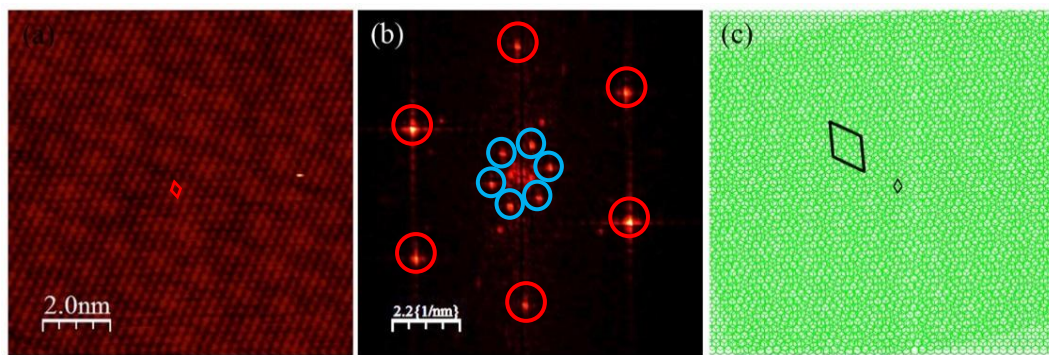


Figure 3.13 (a) ($10\text{nm} \times 10\text{nm}$) The atomic-scale graphene image ($10\text{nm} \times 10\text{nm}$) close to the first domain at $V = -1.0\text{V}$, $I = 0.2\text{nA}$; (b) FFT pattern for the graphene image in panel (a). The red circles are graphene spots, the blue circles represent the Moiré pattern; (c) The model of the turbostratic stacking of three graphene layers (AA'B). The angle between A and A' planes is 14° , the corrugation has a period of 1.00nm, and the orientation with graphene lattice is 32° .

3.4.3 Electronic Properties of Graphene on 6H-SiC (000-1)

To study the electronic properties of multilayer graphene on 6H-SiC (000-1) substrate, the spectroscopy measurement in single point mode was conducted (see Figure 3.14 (a)). More than 15 similar curves were chosen to guarantee the reproducibility of the results. Under normal imaging conditions, a constant current of 0.2nA was used. A smaller tip-sample separation is required for a smaller bias

voltage. When the spectroscopy measurement is carried out, the feedback loop is off, so that the tip position remains unchanged. Thus, over the same bias voltage ramp range, a smaller tip-sample separation exponentially increases the electron tunneling, producing a higher tunneling current.

The differential conductance of graphene in different domains are represented in Figure 3.14 (b). From the dI/dV spectroscopy curve, when a bias voltage of -1.0V was applied, the differential conductance is smaller compared with the curves at a bias voltage of -0.5V. Whereas, the zoomed dI/dV -V curve shows the band gap near Fermi level is zero. At a set-point bias voltage of -0.5V, the differential conductance curve also shows a zero band gap. In addition, the inflection point representing the Dirac point in dI/dV -V curve is not detected. The spectroscopy feature of multilayer graphene on SiC (000-1) is similar to the quasi-free standing monolayer graphene, agreeing with the previous study of graphene electronic properties on C-terminated SiC substrate[46, 47].

At a same set-point bias voltage, for the multilayer graphene with different stacking modes, no obvious differences are shown in the dI/dV -V curves, indicating the azimuthal disorder of graphene on C-terminated SiC cancels out the electronic interactions between the graphene layers and makes the multilayer graphene on SiC (000-1) show a feature of free-standing graphene.

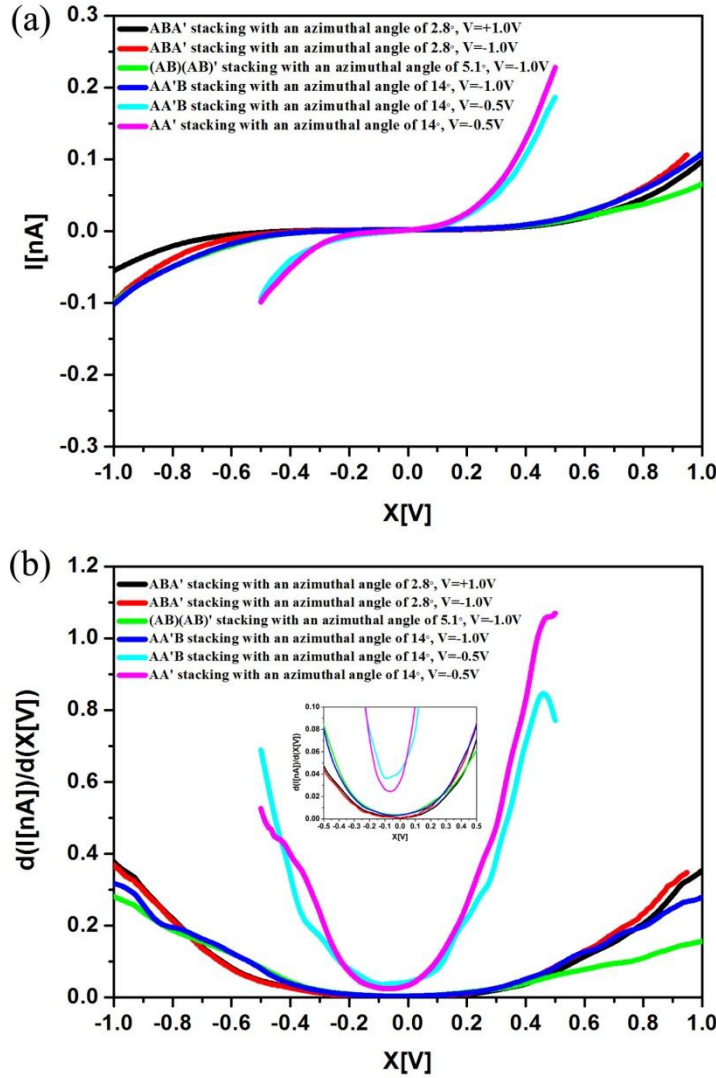


Figure 3.14 (a) I-V spectroscopy measurement for the multilayer graphene in different domains on 6H-SiC (000-1); (b) Differential conductance ($dI/dV-V$) of the multilayer graphene with different azimuthal angles on 6H-SiC (000-1) substrate, tunneling current $I=0.2nA$.

On 6H-SiC (000-1) substrate, the graphene domains are confined by pleats and a series of beads at the boundaries. The topography and electronic properties of the beads are also studied. In Figure 3.15, a zoomed STM image ($12\text{nm}\times12\text{nm}$) of the beads surrounding the second domain at low bias voltage (-1.0V) is presented. The average height of the beads ranges from 1.76\AA to 6.17\AA . The differential conductance of the beads is measured when the set-point bias is -1.0V (Figure 3.15 (b)). The dI/dV spectroscopy curve does not show clear band gap and the Dirac

point shift with respect to the Fermi level is not detected. The spectroscopy feature is similar to the STS curve of multilayer graphene on SiC (000-1), which implies the beads are folded sp₂ hybridized graphene. They can be perceived as the precursor for the carbon nanotube grown on the C face of SiC substrate[48, 49].

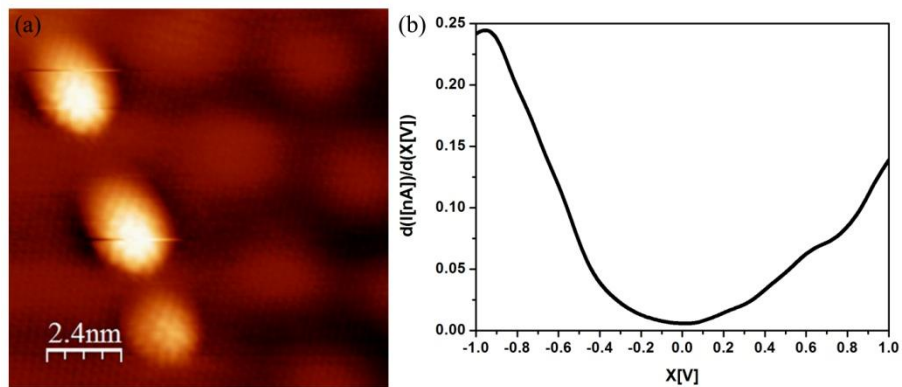


Figure 3.15 (a) (12nm×12nm) Topography of the beads surrounding the second domain, the average height is 3.05Å, tunneling condition: V= -1.0V, I=0.2nA; (b) The (dI/dV)-V spectroscopy for the beads in Panel (a), V_{sp}=-1.0V, I=0.2nA.

3.5 Conclusions

In this chapter, the experimental procedure, topography and electronic structure of epitaxial graphene grown on both Si-terminated and C-terminated 6H-SiC substrate are studied.

The number of graphene layers can be precisely controlled on the Si-terminated face. The angle between the graphene and the SiC substrate is always 30°. In my experiment, only monolayer and bilayer graphene were obtained. Monolayer graphene shows a honeycomb lattice, while bilayer graphene exhibits a triangular lattice because of the Bernal stacking. The $(6\sqrt{3} \times 6\sqrt{3})$ buffer layer between the graphene and the SiC substrate induces n-doping in the graphene and makes the Dirac point of zero-band gap graphene shift to lower energy than the Fermi level.

In contrast to the graphene on Si-terminated face, several graphene layers grow on the C-terminated SiC substrate and they show a turbostratic growth mode. Even though the preferential orientations of graphene on 6H-SiC (000-1) substrate have been reported[46], it is not obvious in my experimental results. Graphene domains with different Moiré patterns are separated by the folded sp₂ hybridized carbon pleats and beads. The Moiré pattern comes from the azimuthal disorder of the top few graphene layers, and a smaller azimuthal angle leads to a larger period of the Moiré pattern. In addition, the buffer layer does not exist between graphene and SiC substrate, which keeps Dirac point at the same energy level as the Fermi level. Graphene on C-terminated SiC substrate behaves more like free-standing compared with that on Si-terminated face.

3.6 Bibliography

- [1] K. S. Novoselov, A. K. Geim, *et al.* Electric field effect in atomically thin carbon films. *Science.*, 306: 666-669 (2004).
- [2] K. S. Novoselov, A. K. Geim, *et al.* Two-dimensional gas of massless Dirac fermions in graphene. *Nature*, 438: 197-200 (2005).
- [3] Y. Zhang, Y.-W. Tan, *et al.* Experimental observation of the quantum Hall effect and Berry's phase in graphene. *Nature*, 438: 201-204 (2005).
- [4] A. K. Geim and K. S. Novoselov. The rise of graphene. *Nature Mater.*, 6: 183-191 (2007).
- [5] M. Choucair, P. Thordarson and J. A. Stride. Gram-scale production of graphene based on solvothermal synthesis and sonication. *Nature Nanotechnology.*, 4: 30-33 (2009).
- [6] S. Park and R. S. Ruoff. Chemical methods for the production of graphenes. *Nature Nanotechnology*, 4: 217-224 (2009).
- [7] H. M. Wang, Y. H. Wu, *et al.* Electronic transport and layer engineering in multilayer graphene structures. *Appl. Phys. Lett.*, 92: 053504 (2008).

- [8] C. G. Navarro, M. Burghard and K. Kern. Elastic properties of chemically derived single graphene sheets. *Nano Lett.*, 8: 2045-2049 (2008).
- [9] S. Bae, H. Kim, *et al.* Roll-to-roll production of 30-inch graphene films for transparent electrodes. *Nature Nanotech.*, 5: 574-578 (2010).
- [10] L. Y. Jiao, L. Zhang, *et al.* Narrow graphene nanoribbons from carbon nanotubes. *Nature.*, 458: 877-880 (2009).
- [11] D. V. Kosynkin, A. L. Higginbotham, *et al.* Longitudinal unzipping of carbon nanotubes to form graphene nanoribbons. *Nature.*, 458: 872-876 (2009).
- [12] C. Berger, Z. M. Song, *et al.* Ultrathin epitaxial graphite: 2D electron gas properties and a route toward graphene-based nanoelectronics. *J. Phys. Chem. B.*, 108: 19912-19916 (2004).
- [13] W. A. d. Heera, C. Berger, *et al.* Epitaxial graphene. *Solid State Commun.*, 143: 92-100 (2007).
- [14] Luxmi, N. Srivastava, *et al.* Comparison of graphene formation on C-face and Si-face SiC {0001} surfaces. *Phys. Rev. B.*, 82: 235406 (2010).
- [15] K. Heinz, J. Bernhardt, *et al.* Functional surface reconstructions of hexagonal SiC. *J. Phys.: Condens. Matter*, 16: 1705-1720 (2004).
- [16] H. Matsunami and T. Kimoto. Step-controlled epitaxial growth of SiC: High quality homoepitaxy. *Mater. Sci. Eng., R.*, 20: 125-166 (1997).
- [17] X. N. Xie, N. Yakolev and K. P. Loh. Distinguishing the H3 and T4 silicon adatom model on 6H-SiC(0001) $\sqrt{3}\times\sqrt{3}R30^\circ$ reconstruction by dynamic rocking beam approach. *J. Chem. Phys.*, 119: 1789-1793 (2003).
- [18] J. Schardt, J. Bernhardt, *et al.* Crystallography of the (3×3) surface reconstruction of 3C-SiC(111), 4H-SiC(0001), and 6H-SiC(0001) surfaces retrieved by low-energy electron diffraction. *Phys. Rev. B.*, 62: 10335 (2000).
- [19] C. Riedl, C. Coletti and U. Starke. Structural and electronic properties of epitaxial graphene on SiC(0001): A review of growth, characterization, transfer doping and hydrogen intercalation. *J. Phys. D: Appl. Phys.*, 43: 374009 (2010).

- [20] K. V. Emtsev, F. Speck, *et al.* Interaction, growth, and ordering of epitaxial graphene on SiC{0001} surfaces: A comparative photoelectron spectroscopy study. *Phys. Rev. B*, 77: 155303 (2008).
- [21] W. Chen, K. P. Loh, *et al.* Nanoparticle dispersion on reconstructed carbon nanomeshes. *Langmuir*, 20: 10779-10784 (2004).
- [22] W. Chen, H. L. Zhang, *et al.* C₆₀ on SiC nanomesh. *J. Phys. Chem. B.*, 110: 21873-21881 (2006).
- [23] K. V. Emtsev, T. Seyller, *et al.* Initial stages of the graphite-SiC(0001) interface formation studied by photoelectron spectroscopy. *Mater. Sci. Forum*, 556: 525-528 (2007).
- [24] C. Riedl, U. Starke, *et al.* Structural properties of the graphene-SiC(0001) interface as a key for the preparation of homogeneous large-terrace graphene surfaces. *Phys. Rev. B.*, 76: 245406 (2007).
- [25] J. Hass, W. A. d. Heer and E. H. Conrad. The growth and morphology of epitaxial multilayer graphene. *J. Phys.: Condens. Matter*, 20: 323202 (2008).
- [26] F. Varchon, P. Mallet, *et al.* Ripples in epitaxial graphene on the Si-terminated SiC(0001) surface. *Phys. Rev. B.*, 77: 235412 (2008).
- [27] S. Kim, J. Ihm, *et al.* Origin of anomalous electronic structures of epitaxial graphene on silicon carbide. *Phys. Rev. Lett.*, 100: 176802 (2008).
- [28] J. Y. Veuillen, F. Hiebel, *et al.* Interface structure of graphene on SiC: an ab initio and STM approach. *J. Phys. D: Appl. Phys.*, 43: 374008 (2010).
- [29] S. Goler, C. Coletti, *et al.* Revealing the atomic structure of the buffer layer between SiC(0001) and epitaxial graphene. *Carbon*, 51: 249-254 (2013).
- [30] C. Bai. Scanning Tunneling Microscopy and Its Application. Springer-Verlag Berlin Heidelberg (2000).
- [31] J. A. Stroscio, R. M. Feenstra and A. P. Fein. Electronic Structure of the Si(111)2×1 Surface by Scanning-Tunneling Microscopy. *Phys. Rev. Lett.*, 57: 2579 (1986).

- [32] H. Yang, G. Baffou, *et al.* Topology and electron scattering properties of the electronic interfaces in epitaxial graphene probed by resonant tunneling spectroscopy. Phys. Rev. B., 78: 041408 (2008).
- [33] S. Y. Zhou, G. H. Gweon, *et al.* Substrate-induced bandgap opening in epitaxial graphene. Nature Mater., 6: 770-775 (2007).
- [34] A. Mattausch and O. Pankratov. Ab initio study of graphene on SiC. Phys. Rev. Lett., 99: 076802 (2007).
- [35] A. Bostwick, T. Ohta, *et al.* Quasiparticle dynamics in graphene. Nature Phys., 3: 36-40 (2007).
- [36] H. Yang. Atomic-scale study of graphene and electroluminescence properties of PTCDI on 6H-SiC (0001) surface by scanning tunneling microscopy. Université Paris-Sud 11 (2009).
- [37] D. S. Lee, C. Riedl, *et al.* Raman spectra of epitaxial graphene on SiC and of epitaxial graphene transferred to SiO₂. Nano Lett., 8: 4320-4325 (2008).
- [38] T. Ohta, A. Bostwick, *et al.* Controlling the electronic structure of bilayer graphene. Science., 313: 951-954 (2006).
- [39] M. Aoki and H. Amawashi. Dependence of band structures on stacking and field in layered graphene. Solid State Commun., 142: 123-127 (2007).
- [40] C. Berger, Z. M. Song, *et al.* Electronic confinement and coherence in patterned epitaxial graphene. Science., 312: 1191-1196 (2006).
- [41] F. Hiebel, P. Mallet, *et al.* Atomic and electronic structure of monolayer graphene on 6H-SiC(000-1)(3×3): A scanning tunneling microscopy study. Phys. Rev. B., 80: 235429 (2009).
- [42] F. Hiebel, P. Mallet, *et al.* Graphene-substrate interaction on 6H-SiC(000-1): A scanning tunneling microscopy study. Phys. Rev. B, 78: 153412 (2008).
- [43] F. Varchon, P. Mallet, *et al.* Rotational disorder in few-layer graphene films on 6H-SiC(000-1): a scanning tunneling microscopy study. Phys Rev B., 77: 165415 (2008).

- [44] S. Latil, V. Meunier and L. Henrard. Massless fermions in multilayer graphitic systems with misoriented layers: Ab initio calculations and experimental fingerprints. *Phys. Rev. B.*, 76: 201402 (2007).
- [45] J. M. Campanera, G. Savini, *et al.* Density functional calculations on the intricacies of Moiré patterns on graphite. *Phys. Rev. B*, 75: 235449 (2007).
- [46] L. I. Johansson, R. Armiento, *et al.* Multiple π -bands and bernal stacking of multilayer graphene on C-face SiC, revealed by nano-angle resolved photoemission. *Sci Rep.*, 4: 4157 (2014).
- [47] M. Sprinkle, J. Hicks, *et al.* Multilayer epitaxial graphene grown on the SiC (000-1) surface; structure and electronic properties. *J. Phys. D: Appl. Phys.*, 43: 1-12 (2010).
- [48] T. Yamauchi, T. Tokunaga, *et al.* Influence of surface structure modifications on the growth of carbon-nanotubes on the SiC(000 1) surfaces *Surf. Sci.*, 600: 4077-4080 (2006).
- [49] M. Naitoh, M. Kitada, *et al.* An STM observation of the initial process of graphitization at the 6H-SiC (000-1) surface. *Surf. Rev. Lett.*, 10: 473 (2003).

Chapter 4

Electronic Properties of Ni-Phthalocyanine Molecules on Graphene

Table of Contents

4.1 Introduction.....	80
4.2 Experimental Procedure.....	81
4.3 Topography of Self-Assembled NiPc Molecules on Graphene/ 6H-SiC (0001).....	82
4.3.1 Steps of NiPc Molecular Network on Monolayer Graphene.....	82
4.3.2 Atomic-Scale STM Images of NiPc Molecules on Graphene.....	86
4.4 Electronic Properties of NiPc Molecules on Graphene.....	90
4.5 DFT Calculations of NiPc Molecules on Graphene/SiC (0001).....	92
4.5.1 Topography of NiPc Molecules on Graphene.....	92
4.5.2 Interpretation of Spectroscopy Results by DFT Calculation.....	98
4.6 Conclusions.....	104
4.7 Bibliography.....	104

4.1 Introduction

Metal-Phthalocyanine (MPc) molecules have a π -conjugated electronic structure with tunable electronic and magnetic properties through the appropriate choice of the central metal ion. They have many similarities with the porphyrin structure found in biological molecules, such as chlorophyll and haemoglobin. Thus, they are of great technological and fundamental interest. Among them, the isolated Ni-Phthalocyanine (NiPc) molecule shows a square planar configuration with D_{4h} symmetry. Its molecular structure is illustrated in Figure 4.1 (a), wherein the central Ni²⁺ is coordinated by four N atoms with same bond length (about 1.92 Å in the optimized configuration from DFT calculations)[1]. According to the ligand field theory, the frontier molecular orbital of NiPc is the linear combination of the central Ni²⁺ ion and the surrounding Pc²⁻ ring. The Ni²⁺ ion has a 3d⁸ electron configuration and its orbital energy diagram in the NiPc molecule is shown in Figure 4.1 (b), in which the d_{z²} orbital is fully filled[2, 3].

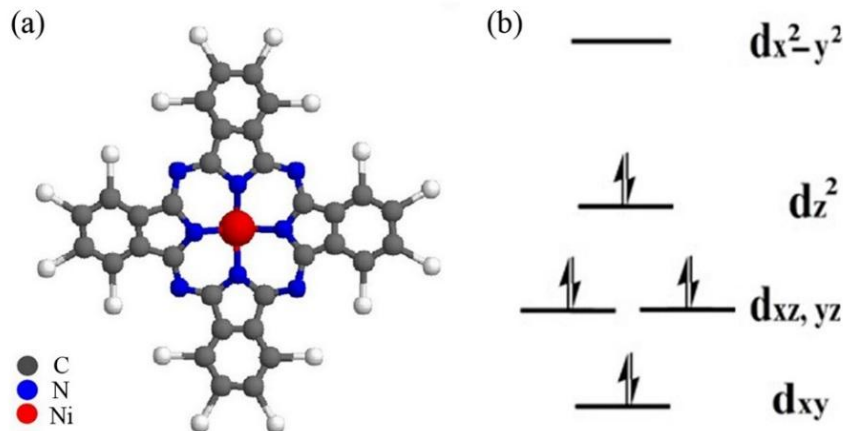


Figure 4.1 (a) NiPc molecular structure. The dark grey balls represent C atoms, blue balls represent N atoms, the red ball represents the Ni²⁺ ion, and silver balls are H atoms. The NiPc molecule has a square planar configuration with D_{4h} symmetry; (b) Schematic orbital energy diagram for Ni²⁺ in NiPc molecules, the d_{z²} orbital is fully filled.

4.2 Experimental Procedure

In this study, NiPc molecules in the form of a dark blue powder were purchased from Sigma Aldrich and with a synthesis purity of 85%. Monolayer graphene was epitaxially grown on the (3×3) n-doped 6H-SiC (0001) surface by sublimation of bulk silicon atoms in ultra-high vacuum (UHV). Prior to molecule deposition, the molecular powder was cleaned by several cycles of degassing. After that, the self-assembled molecular layer (SAM) were made by a 8 min deposition at 250°C by resistive heating of the NiPc molecules in a Quad Dopant Source with water cooling. During the deposition, the sample was held at room temperature with an initial pressure of 2×10^{-10} mbar. Subsequently, the sample was post-annealed by indirect resistive heating at 200°C for 3 hours to stabilize the molecules on the graphene substrate.

The topography of the NiPc molecules on graphene was observed by room-temperature STM (10^{-11} mbar). The electronic interactions between molecules and graphene were probed by tunneling spectroscopy (I-V) with the feedback loop off. The normalized differential conductivity (NDC) was also obtained by dividing the smoothed first derivative of I-V curves ($d\text{I}/d\text{V}$) with smoothed I-V curves. The purpose of smoothing is to avoid the artificial mathematical errors produced in the normalized differential conductivity calculation. The STM images and spectroscopy were processed by the free software ‘WSXM’. Density functional theory (DFT) calculations based on van der Waals approximation were performed by Prof. Philippe Sonnet (IS2M, Mulouse) in collaboration with Dr. Eric Duverger (FEMTO-ST, Besançon) to further understand the electron coupling regime of NiPc molecules on graphene.

4.3 Topography of Self-Assembled NiPc Molecules on Graphene/ 6H-SiC (0001)

4.3.1 Steps of NiPc Molecular Network on Monolayer Graphene

Figure 4.2 (a) presents a 100nm×100nm STM image of the NiPc molecular layer on graphene/ 6H-SiC (0001) substrate. NiPc molecules grow seamlessly across the surface steps between the first, second and third terraces. However, the molecular array changes 16 ° in anti-clockwise direction at the step between the second and fourth domains. The three-dimensional topography of NiPc molecules rotated by 90 ° with respect to the 2D image in clockwise direction displays the height difference between different molecular domains. To better understand the cause for the change in the molecular array direction, the step heights are measured (see Figure 4.2 (c)). The black line profile shows a step height between the first and second molecular domains of $6.03 \pm 0.14\text{\AA}$. The red line profile presents the height differences of second-third domains and second-fourth domains; they are 4.98\AA ($\pm 0.16\text{\AA}$) and 3.15\AA ($\pm 0.13\text{\AA}$), respectively. The steps are likely to be caused by the graphene or bulk SiC. In the process of growing graphene on 6H-SiC (0001) by thermal evaporation of Si atoms, the $(6\sqrt{3} \times 6\sqrt{3})$ (R30 °) reconstruction, or zero-layer graphene, is the precursor before the real graphene appears. To obtain the sp₂-hybridized graphene, the bulk SiC atoms have to be consumed. Because the area density of C atoms in a SiC bilayer ($1.22 \times 10^{15} \text{ cm}^{-2}$) is about one-third of C atoms in graphene ($3.82 \times 10^{15} \text{ cm}^{-2}$), three layers of SiC is required to form one graphene layer. When the temperature distribution is inhomogeneous during thermal evaporation, the underlying $(6\sqrt{3} \times 6\sqrt{3})(\text{R}30^\circ)$ interface will start to convert to the second graphene layer in regions with a local high temperature, and a new buffer layer will form by consuming the bulk SiC underneath. The formation of a new graphene layer induces a bilayer graphene structure with an interlayer spacing of 3.35\AA . Hence, the step height between the monolayer and bilayer graphene terraces

will be the height difference between three times the SiC bilayer thickness and the double-layer graphene spacing, which is 4.19 Å[4-6].

Figures 4.2 (d) and (e) reflect the likely mechanism of the graphene step formation under the molecular domains in panel (a). The 6H-SiC (0001) crystal has steps on the surface and the step height is generally integer multiples of a SiC bilayer (2.51 Å). We assume that the cross-sectional model of monolayer graphene terraces on SiC (0001) is as illustrated in Figure 4.2 (d). The height difference between the left and middle monolayer graphene terraces is one SiC bilayer spacing, and the difference between the middle and right graphene terraces is three SiC bilayers (7.54 Å). If the graphene growth is not uniform, the temperature in middle region is higher, the second graphene layer will start to nucleate here. Because three SiC bilayers will be consumed in the formation of a new graphene layer, the newly formed ($6\sqrt{3} \times 6\sqrt{3}$) (R30°) interface in the middle region will collapse to the same height as the zero layer graphene in the right area and will be bound at the edge to the Si atoms in the bulk SiC (see Panel (e)). The expected step height between the middle and right area will be the separation of the bilayer graphene (3.35 Å), which corresponds to the height difference between the second and fourth NiPc molecular domains (deviation: 5.97%). The height difference between the left monolayer graphene and middle bilayer graphene terraces will be 6.70 Å (height difference between monolayer and bilayer graphene terraces 4.19 Å plus a SiC bilayer spacing). It is correlated to the step height between the first and second molecular domains (deviation: 10%). Even though the step height of 6.03 Å is close to the graphite interlayer spacing plus a SiC bilayer step (deviation: 3.07%), these two steps cannot form at the same position, due to the permanent interlayer spacing of graphite.

The step height between the second and third domains (4.98 ± 0.16 Å) can be deduced as two SiC bilayers (deviation: 0.4%). The step edge has a straight and zigzag shape, it is similar to the reported three SiC bilayer steps on hydrogen etched 6H-SiC (0001)

surface[7]. Even though our SiC sample is not H etched, steps with an integral multiple of the SiC bilayer thickness are likely exist.

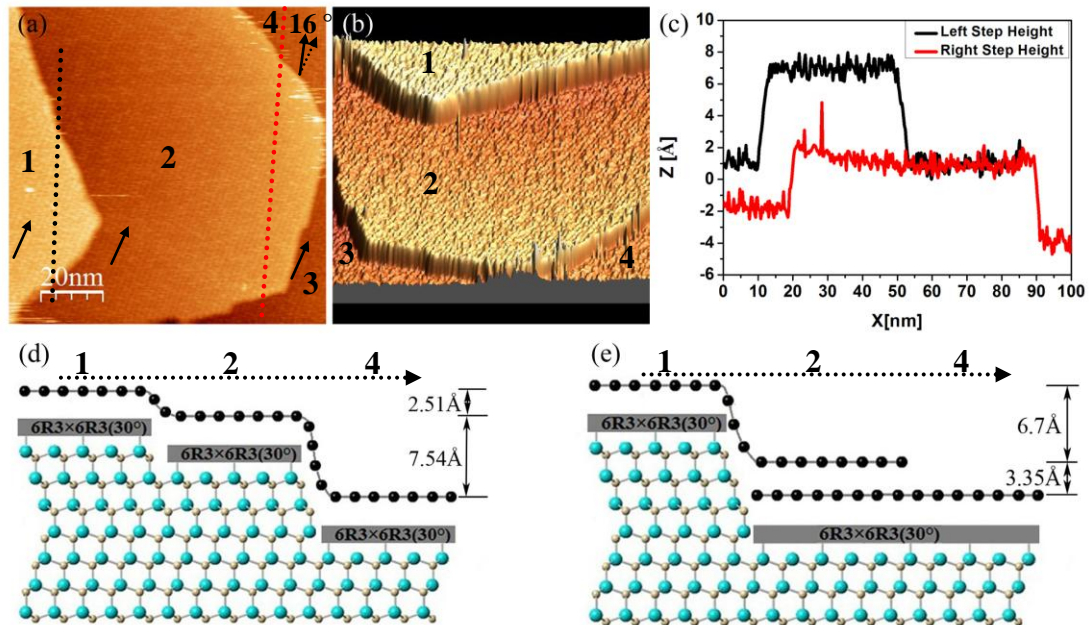


Figure 4.2 (a) 100nm×100nm STM image of self-assembled NiPc molecules on graphene/ SiC (0001), tunneling condition: $V=-2.5V$, $I=0.1nA$; (b) Three-dimensional topography of NiPc molecular domains, which is rotated 90° with respect to the 2D STM image; (c) Line profiles of the molecular domain step heights; the black curve is the step height between the first and second domain (6.03Å). The red curve is the step heights of second-third domain and second-fourth domains (4.98Å and 3.15Å respectively); (d) and (e) The mechanism of a new graphene layer formation underneath the NiPc molecular domains. The blue balls represent Si atoms, grey balls represent C atoms in the bulk SiC, black balls represent the C atoms in graphene.

Now that the step heights in the molecular domains have been figured out, it is interesting to find that the NiPc molecular network is continuous at the steps of 6.03Å and 4.98Å, where the graphene terraces persist, while the molecular network is interrupted at the step of 3.15Å, where the graphene terraces are interrupted. This indicates that the NiPc molecular network is commensurate with the underlying

graphene topography. This result is also found in other molecular systems on graphene, such as the close-packed molecular network of PTCDA[8], pentacosadiynoic acid (PCDA)[9], phthalocyanines[10] and the low density networks of dehydrobenzo(12) annulene (DBA) derivatives[11]. These findings corroborate that the commensurability of the molecular network with underlying graphene topography is not a property of a given molecular system but is rather inherent to the substrate underneath (graphene-SiC combination).

Figure 4.3 (a) illustrates a $50\text{nm} \times 50\text{nm}$ STM image of NiPc molecules on graphene/6H-SiC (0001). The molecular network is continuous along the transition region between two graphene terraces. The measured step height is 10.10\AA , which can be deduced as the monolayer-bilayer graphene terrace separation (4.19\AA) plus two SiC bilayer spacing (5.02\AA) (deviation: 9.78%)⁸ (see panel (c)). A graphene step with a height of 10.00\AA is also found on the pure graphene terraces on 6H-SiC (0001) (see the inset in panel (c)). This further demonstrates the adherence of molecular network to the graphene/ SiC substrate underneath.

⁸ The Z-piezo in our RT-STM has a vertical error of 5%-10% larger than the real value. The step height with a deviation less than 10% is reasonable.

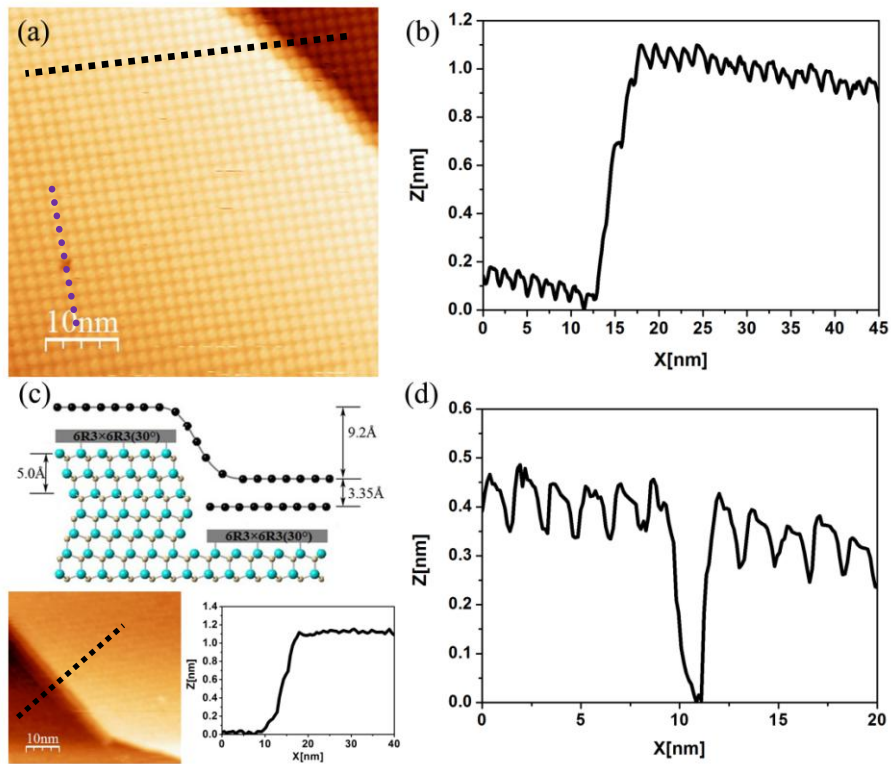


Figure 4.3 (a) 50nm×50nm STM image of NiPc molecular network along 10.10 \AA graphene step, tunneling condition: V=+2.5V, I=0.4A; (b) Line profile of the step height along the black dotted line in panel (a); (c) Atomic model of 9.20 \AA graphene step underneath NiPc molecular domains and the measured 10.00 \AA step in the pure graphene terraces on 6H-SiC (0001), tunneling condition: V=-0.5V, I=0.3nA; (d) Profile for the single vacancy in NiPc molecular network.

4.3.2 Atomic-Scale STM Images of NiPc Molecules on Graphene

Figure 4.4 illustrates a series of 10nm×10nm atomic-scale STM images of the occupied and unoccupied states of the NiPc molecules on graphene/6H-SiC (0001). Each molecule within the layer shows four lobes corresponding to the phthalocyanine ring with a depression in the center at both negative (-2.0V and -1.6V) and positive bias voltage (+0.7V, +1.6V, +2.0V and +2.5V). A similar topography is also found in NiPc molecules on Au (111) substrate[2], PtPc and PdPc molecules on Highly Ordered Pyrolytic Graphic (HOPG)[12], and CuPc on Au (111)[13] and on graphene/Ir (111)[14].

It is well known when the tip electronic states are uniform, the STM images reflect the local density of state (LDOS) near the Fermi level of the surface at the tip position ($\rho_s(\gamma, E)$). The LDOS of Ni^{2+} primarily comes from the d_z^2 orbital and a small fraction from dxz and dyz orbitals. It is obvious that the 3d orbitals of the Ni^{2+} are conspicuous by their absence in STM image. The depression in the center indicates that the molecular DOS is dominated by the π -states of the phthalocyanine ring with little contribution from the Ni atom. The topography of the NiPc molecular layer on HOPG is similar. The d_z^2 orbital of Ni^{2+} is located at 2.9eV below the Fermi level [12]. When the smaller bias voltage is used, the molecular center will show a depression because of the lack of the d_z^2 orbital contribution.

Even though there is reduced LDOS at the position of the metal center, there is a correlation with the molecule-substrate interaction because the d-orbital-mediated tunneling is possibly an important channel between the MPc molecules and substrate. The electronic coupling between NiPc molecules and graphene will be discussed in the next section.

Another possible factor influencing the LDOS of the metal ion is the chemical reactivity. It is reported that NiPc molecules can adsorb oxygen with saturation coverage at the pressure of 3×10^{-8} Torr[15]. In our case, all the experimental procedures concerning the NiPc molecules (deposition, measurement, and so on) were conducted in UHV (10^{-10} mbar), so the reactions with oxygen could be ignored.

In Figure 4.4 (a) ($V=+2.5\text{V}$) and (e) ($V=-1.6\text{V}$), the bright area of the NiPc molecules also comprises the four coordinated N atoms. It results from the higher contribution from p_z orbitals of N atoms to the tunneling current which is confirmed by the DFT calculations discussed later.

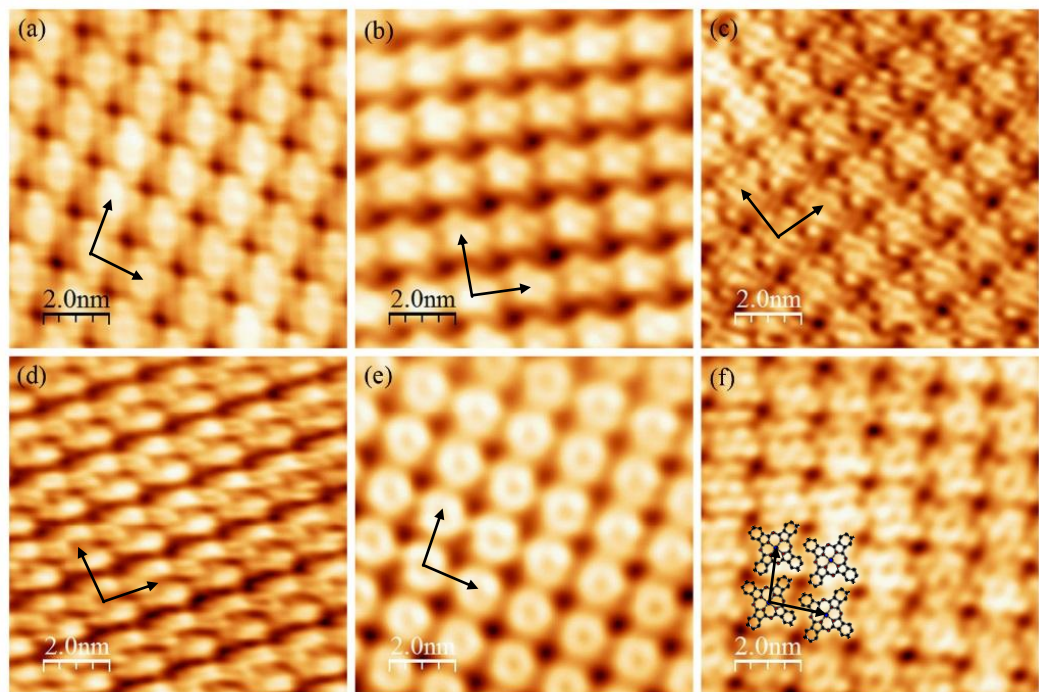


Figure 4.4 Zoomed $10\text{nm} \times 10\text{nm}$ STM image of NiPc molecular network on epitaxial graphene on 6H-SiC (0001). (a) Unoccupied state of NiPc molecules, tunneling condition: $V=+2.5\text{V}$, $I=0.4\text{nA}$; (b) Unoccupied state of NiPc molecules, tunneling condition: $V=+2.0\text{V}$, $I=0.4\text{nA}$; (c) Unoccupied state of NiPc molecules, tunneling condition: $V=+1.6\text{V}$, $I=0.4\text{nA}$; (d) Unoccupied state of NiPc molecules, tunneling condition: $V=+0.7\text{V}$, $I=0.4\text{nA}$; (e) Occupied state of NiPc molecules, tunneling condition: $V=-1.6\text{V}$, $I=0.4\text{nA}$; (f) Occupied state of NiPc molecules, tunneling condition: $V=-2.0\text{V}$, $I=0.4\text{nA}$. The images were Fourier filtered to reduce the noise.

From the STM images in Figure 4.4, it can also be seen that the NiPc molecules form a self-assembled close packed molecular network on graphene with a square lattice. The averaged lattice constant is 1.42nm ($\pm 0.03\text{nm}$) $\times 1.38\text{nm}$ ($\pm 0.02\text{nm}$) with an angle of 89° ($\pm 1^\circ$) (see Figure 4.5 (b)).

In the NiPc molecular domains, the molecular orientation has a certain angle with respect to the molecular lattice direction. The electrostatic interaction between H-terminated molecules provides the lateral stabilization of the self-assembled close packed layers. Moreover, the repulsive force between C-H bonds in adjacent

benzene rings limits the possible orientations. Several molecular rotation angles with respect to the molecular lattice directions are observed in the experiment: 0° ($\pm 2^\circ$), $\pm 10^\circ$ ($\pm 2^\circ$), and $\pm 20^\circ$ ($\pm 3^\circ$). The whole system is in equilibrium between the molecule-molecule interaction and molecule-substrate interaction, NiPc molecules do not have the preferential orientations on graphene, which implies the molecule-graphene interaction might be weak.

In addition, the atomic-scale STM images of NiPc molecules on graphene (Figure 4.4) display different molecular lattice directions. In total, there are six molecular arrays in the experiment, as summarized in Figure 4.5 (b). The model of six molecular square lattices are displayed in Figure 4.5 (c). In the model, each line in the same color represents one square lattice of the self-assembled molecular network. The six molecular square lattice directions are approximately uniformly distributed on the graphene. The averaged angle difference between the adjacent molecular lattice directions is 15° ($\pm 2.2^\circ$), which is the half of the graphene armchair-zigzag angle difference. The change of molecular lattice direction (16°) at the bilayer graphene separation step (3.15 \AA) also matches with the value here. Graphene has three-fold symmetry and the NiPc molecules have D_{4h} symmetry, so the six square lattice directions (twelve molecular arrays) can be deduced as the combination of three C-C crystallographic directions of the graphene and four molecular conformations. These observations of the NiPc molecular lattice and orientations demonstrate that the molecular lattice direction is dominated by the substrate (graphene) symmetry underneath, while the molecular orientations are primarily dependent on the intermolecular interaction.

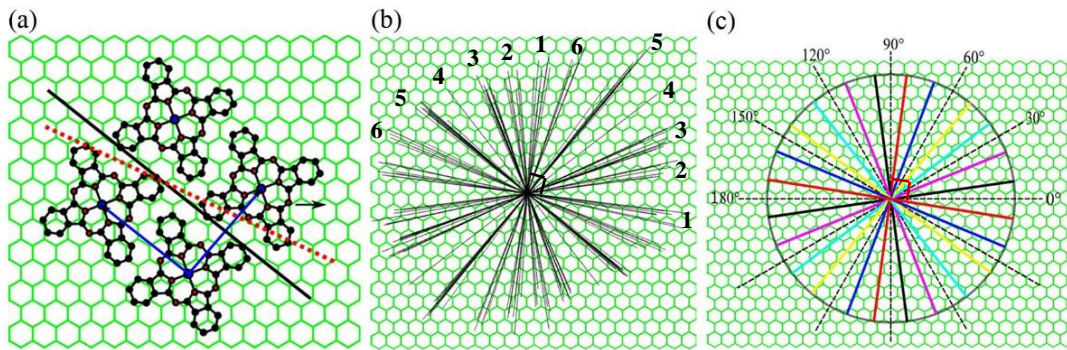


Figure 4.5 (a) The schematic diagram of NiPc molecular square lattice on graphene/SiC (0001) based on experimental results. The lattice constant is $1.42\text{nm} \times 1.38\text{nm}$ with an angle of 89° ; (b) All the NiPc molecular lattice directions summarized from the experiments; (c) The averaged six NiPc molecular lattice directions based on Panel (b), each cross lines in the same color represents one molecular lattice, the angle difference is about 15° .

4.4 Electronic Properties of NiPc Molecules on Graphene

To study the electronic properties of the NiPc molecular network on graphene/6H-SiC (0001), scanning tunneling spectroscopy (STS) measurements were carried out. Figure 4.6 shows the STS results both in the centers (Panel (a)) and on the lobes (Panel (c)) of the NiPc molecules. For all the I-V curves, the tunneling current decreases as the increased set-point bias voltages. For a constant tunneling current of 0.4nA , as the set-point bias voltage increases, the tip-sample separation becomes larger. When a spectroscopic measurement is made, the feedback loop is off, so that the tip-sample separation is constant when the bias voltage ramps in the same energy range from $+2.0\text{V}$ to -2.0V , the electronic overlap will be less if the tip-sample separation is large. Hence, the higher set-point bias voltage is correlated to the lower electron tunneling current in I-V curve. In addition, the I-V curves in molecular centers show a diode-like asymmetrical nature: the tunneling current at positive

potential is higher than that at negative potential, while, for the I-V curves on molecular lobes, the tunneling current is similar at the bipolar potentials.

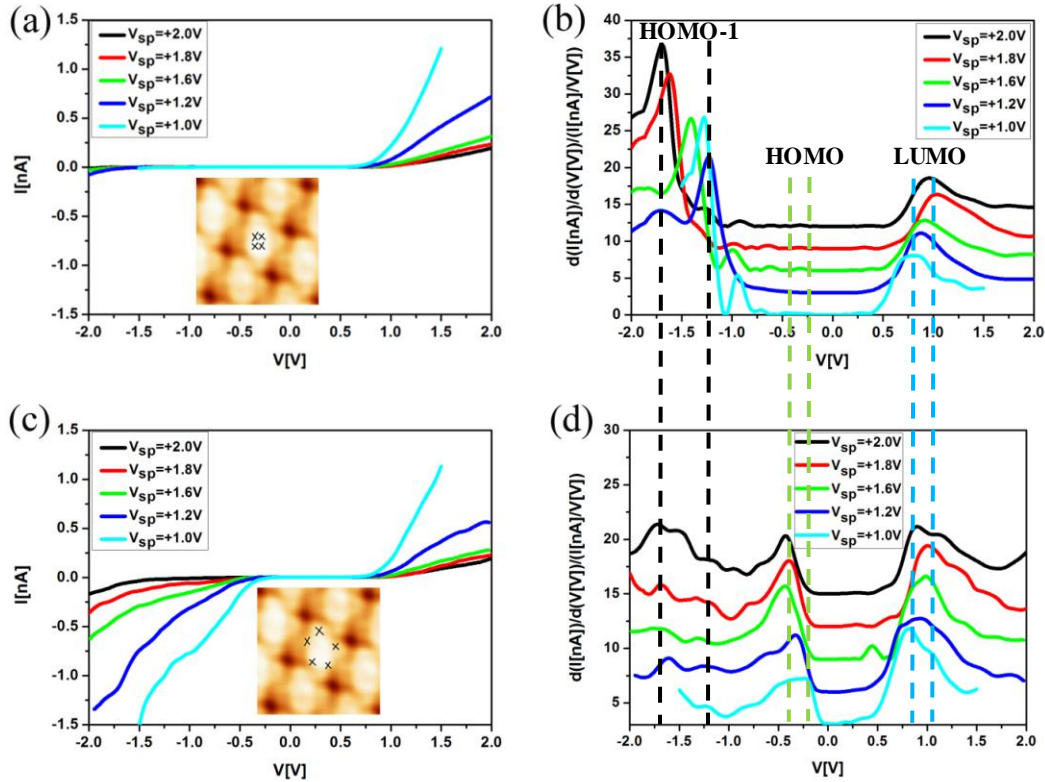


Figure 4.6 Spectroscopy measurement for NiPc molecules on graphene/ SiC (0001). (a) I-V curves for the NiPc molecular centers at different set-point bias voltages, tunneling current $I=0.4\text{nA}$; (b) The corresponding normalized differential conductance curves for the NiPc molecular centers, each curves are shift in Y axis to better present the conductance difference at different bias voltages; (c) I-V curves for the NiPc molecular lobes at different set-point bias voltages, tunneling current $I=0.4\text{nA}$; (d) The corresponding normalized differential conductance curves for the NiPc molecular lobes.

To understand the electronic properties of NiPc molecules on graphene/ 6H-SiC (0001) substrate, the normalized differential conductance (NDC) was obtained by dividing the first derivative of I-V curves (dI/dV), with I-V curves (see Panel (b)). Curve smoothing was kept to a minimum during the calculation to avoid any artificial peak shift. Each curve is shifted a certain value in Y axis to see more clearly

the molecular orbital features at different set-point bias voltages. For the NDC curves for both the molecular centers and the lobes, an unoccupied molecular resonance peak in the range of (+0.81eV, +1.03eV) was detected from the set-point bias voltage of +1.0V to +2.0V, which is assigned as LUMO. For the occupied molecular states, a peak in the range of (-0.43eV, -0.24eV) is detected on the molecular lobes, while this peak is not obvious in the molecular centers. According to the DFT calculation in section 4.5, this resonance peak is the HOMO. It gives a HOMO-LUMO gap ranges from 1.46eV to 1.27eV when the set-point bias voltage varies from +2.0V to +1.0V. The second occupied molecular resonance peak in the range of (-1.70eV, -1.23eV) on the whole molecule can be deduced as the HOMO-1. In this energy range, two peaks are detected. This can be explained by the molecular orbital split. The DFT calculation corroborates that HOMO-1 shows an e_g symmetry, there are two identical charge spatial distributions. The two resonance peaks in dI/dV curve might be caused by the splitting of the degenerate e_g molecular orbital (see section 4.5).

In dI/dV curve, it is interesting to notice that all the NiPc molecular resonance peaks shift closer to the Fermi level with the decrease of the set-point bias voltage (smaller tip-sample separation). It is a little different from the previous results of NiPc molecules on HOPG, where the HOMO peaks shift to Fermi level with the tip-sample separation decreases, while LUMO peak is pinned[16]. The regime for the molecular orbitals shift will be discussed in section 4.5.2.

4.5 DFT Calculations of NiPc Molecules on Graphene/SiC (0001)

4.5.1 Topography of NiPc Molecules on Graphene

To better interpret the STM images and electronic interactions between NiPc molecules and graphene on 6H-SiC (0001), DFT calculations based on van der Waals

approximation were conducted. The DOS calculation of four NiPc molecules self-assembled on AA-stacked bilayer graphene were carried out by Prof. Philippe Sonnet in Mulhouse and the STM image calculations were made by Dr. Eric Duverger in Besançon. Here, I will present the explanations of NiPc molecular topography in this experiment based on DFT calculations.

For graphene grown on SiC (0001), there is a buffer layer underneath the monolayer graphene. Because buffer layer has the same σ -bonds as graphene in the direction parallel to the substrate, to simplify the model in DFT calculation, the AA-stacked bilayer graphene was adopted to simulate the monolayer graphene on buffer layer. The electron doping from the SiC substrate to graphene is not considered. Four molecules were taken to calculate the self-assembled molecular layer on graphene, as shown in Figure 4.7. In the calculation, the molecules form a square lattice with the lattice constants of $14.21\text{\AA} \times 13.83\text{\AA}$ with an angle of 90° ; the parameters are in excellent agreement with the experimental results ($1.42\text{nm} \times 1.38\text{nm}$ with an angle of 89°)

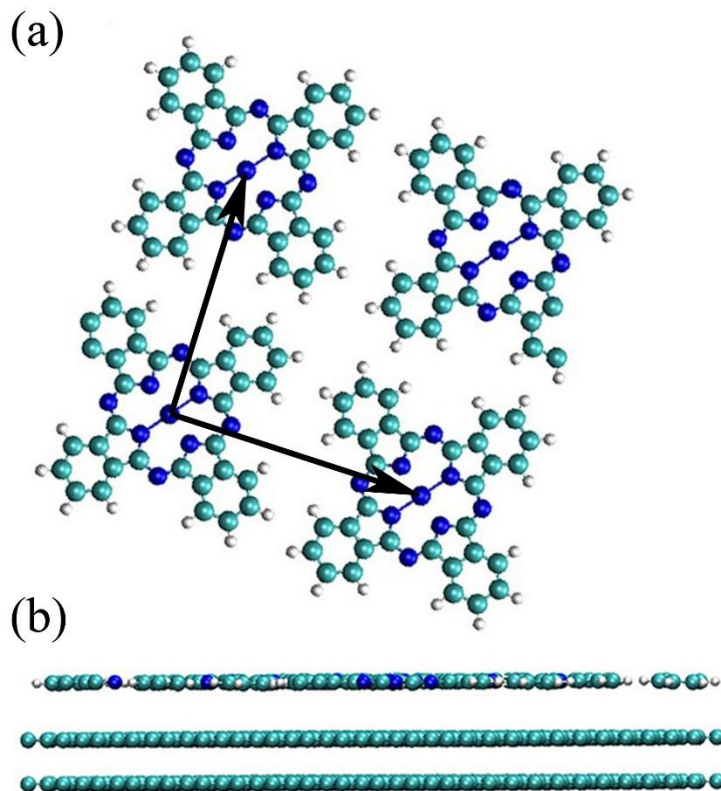


Figure 4.7 (a) Top view of the DFT calculated unit cell of self-assembled NiPc molecular network on AA-stacked bilayer graphene; (b) Front view of the NiPc molecular network on AA-stacked bilayer graphene. The calculated square lattice parameters are $14.21\text{\AA} \times 13.83\text{\AA}$ with an angle of 90° .

The STM images of NiPc molecular network on AA-stacked bilayer graphene were calculated with the BSKAN code and W tip (both s and p orbitals of W are considered in the calculation). Similar to the STM images of the NiPc molecules in the experiment, the NiPc molecules present a depression in the center in both the occupied states (negative bias at -1.0V and -1.5V) and the unoccupied states (positive bias +1.0V and +1.8V). In particular at -1.0V, the NiPc molecular DOS is seen as a dark center and a phthalocyanine ring with four lobes (see Figure 4.8).

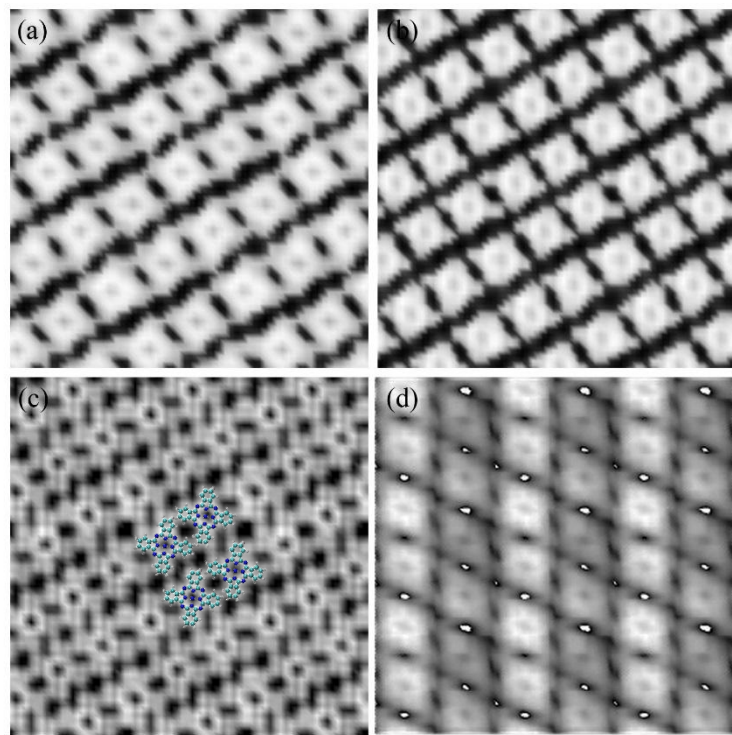


Figure 4.8 DFT calculated STM images of NiPc molecules on AA-stacked bilayer graphene. The BSKAN code was used to simulate the W tip (both s and p orbitals are considered) in the calculation. (a) $V=+1.8V$; (b) $V=+1.0V$; (c) $V=-1.0V$; (d) $V=-1.5V$.

To better explain the STM images from the perspective of molecular frontier orbitals, the projected density of states (PDOS) of self-assembled NiPc molecules on AA-stacked bilayer graphene is calculated. The DOS peaks and the corresponding molecular orbital symmetries near the Fermi level are depicted in Figure 4.9. From the calculation, the LUMO orbital shows a $2e_g$ symmetry, where both the N atoms and π states of C atoms dominate to the DOS. The LUMO is found 0.6eV above the Fermi level. The HOMO is composed of 96.51% from the π state of the C atoms in the Pc ring, the symmetry is a_{1u} , and it found 0.86eV below the Fermi level. The HOMO-1 has a symmetry of e_g and the energy state is 1.46eV below Fermi level. The molecular orbital has a contribution of 43% from the d_{xz} and d_{yz} orbitals of Ni atoms (see Table 4.1). The molecular orbital arising from d_z^2 orbital of Ni^{2+} is further away from the

Fermi level than HOMO-1. According to the crystal field theory, for the metal complex with a square planar geometry, the $d_{x^2-y^2}$ and d_{xy} orbital are higher in energy because of the strong interaction with the ligands in the XY plane, while d_{xz} and d_{yz} orbitals are lower in energy. For the d_{z^2} orbital, the ligand interaction in the z direction is absent, so it has the lowest energy among the d orbitals.

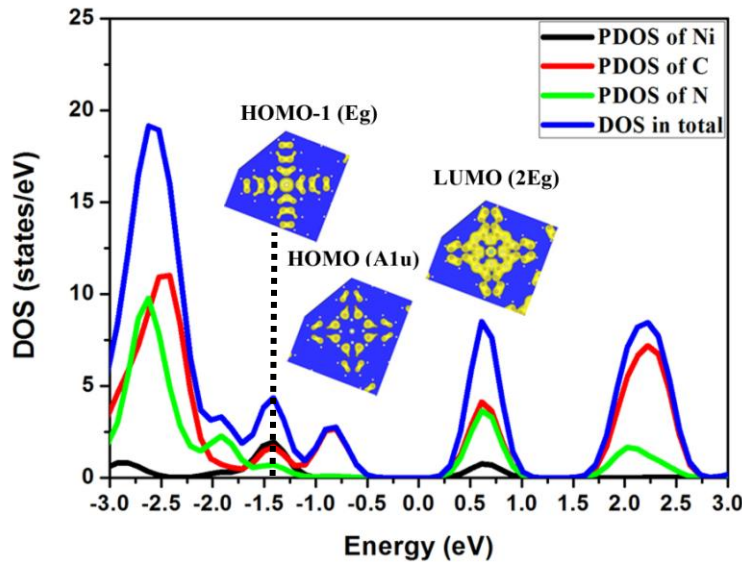


Figure 4.9 Calculated projected density of state (PDOS) of the self-assembled NiPc molecules on decoupled AA-stacked bilayer graphene. The blue profile is the total DOS, the red profile is the PDOS contribution from the C atoms, the green profile is the PDOS contribution from the N atoms, and the black profile is the PDOS contribution from the Ni atoms. The molecular orbitals HOMO-1, HOMO and LUMO are at the energies of -1.46eV , -0.86eV , and $+0.6\text{eV}$ respectively. The corresponding symmetries of molecular orbitals are e_g , a_{1u} and $2e_g$.

The STM images of NiPc molecules on graphene in the occupied and unoccupied states can be explained by the frontier molecular orbitals. In STM, the tunneling current can be expressed by the formula given below:

$$I = \int_0^{eV} \rho_s(r, E) \rho_t(r, -eV + E) T(E, eV, r) dE,$$

Where I is the tunneling current, $\rho_s(r, E)$ and $\rho_t(r, E)$ are the density of states of the sample and tip at the location r and energy E , measured with respect to their individual Fermi levels. $T(E, eV, r) dE$ is the tunneling transmission probability for the electrons with energy E and applied bias voltage V . When tip is imaging the molecules on a substrate, all the molecular orbitals within the energy range between the applied voltage and the Fermi level would contribute to the tunneling current. STM images reflect the mixed information of topography and electronic properties of the surface. NiPc molecules are demonstrated to have planar geometry, therefore, the STM images are dominated by the electronic properties of NiPc molecules on graphene.

For the applied bias voltages of +1.0V and +1.8V, the tunneling current mainly comes from the DOS of molecular LUMO orbital ($2e_g$). Because the contribution from the Ni (8.76%) to the PDOS is small, the molecular center will be a dip in the STM image. In addition, the large PDOS contribution (41.81%) from orbitals of the N atoms makes the four coordinated N atoms prominent in the STM images, in agreement with the experimental results at +2.5V. For the bias voltage of -1.0V, the tunneling current is dominated mainly by the π states of the C atoms in the Pc ring (96.51%) (HOMO with a_{1u} symmetry), so the dark center and four lobes of Pc ring are shown in the STM image (same as the spatial charge distribution of HOMO in Figure 4.9). At $V=-1.5V$, both the HOMO and HOMO-1 contribute to the tunneling current. Because of the e_g symmetry of the HOMO-1, the PDOS from the Ni is produced by the d_{xz} and d_{yz} orbitals. Even though Ni has a majority contribution to the HOMO-1, the e_g symmetry makes the DOS weaker in the centermost position. In addition, the PDOS proportion in both HOMO+ HOMO-1 is less than that of the C atoms, the depression in the molecular center is still present in the STM images.

Table 4.1 PDOS of NiPc molecular layer on AA-stacked bilayer graphene

	HOMO-3	HOMO-2	HOMO-1	HOMO	LUMO	LUMO+1
Molecular Orbital (eV)	-2.56	-1.90	-1.46	-0.86	+0.6	+2.17
Ni (%)	4.03	9.67	43.8	0	8.76	0.4
N (%)	47.1	68.26	16.9	3.49	41.81	19.27
C (π) (%)	48.87	22.07	39.2	96.51	49.43	80.33

4.5.2 Interpretation of Spectroscopy Results by DFT Calculation

To clarify the spectroscopy curves of self-assembled NiPc molecules on graphene, it is important to study the electronic interactions between NiPc molecules on graphene/SiC (0001). In the DFT calculation within D3 van der Waals approximation, the PDOS peaks of both single NiPc molecules in gas phase and the self-assembled NiPc molecular layer (four molecules) on decoupled AA-stacked bilayer graphene are very similar. The calculated adsorption energy of each molecule on graphene is -2.15eV and the total charge transfer from four NiPc molecules to the neutral AA-stacked bilayer graphene is 0.0378e-according to the Bader charge analysis, which is quite small. It indicates a weak van der Waals force between the NiPc molecular layer and neutral graphene. The spatial charge densities of self-assembled NiPc molecules on AA-stacked bilayer graphene are displayed in Figure 4.10. The equilibrium distance between NiPc molecular layer and top graphene layer is 3.24Å. No electron accumulation or depletion is found between NiPc molecular layer and AA-stacked bilayer graphene for any of the HOMO-1, HOMO and LUMO energy levels. It confirms the near-zero charge transfer at the interface of NiPc molecules and neutral graphene.

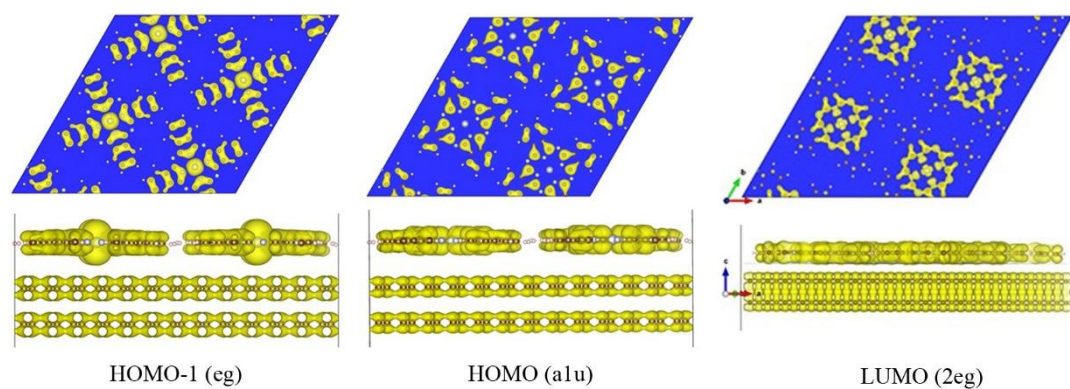


Figure 4.10 Spatial charge distribution for each PDOS peaks of self-assembled NiPc molecules on AA-stacked bilayer graphene. The symmetries of HOMO-1, HOMO and LUMO are e_g , a_{1u} and 2_{eg} respectively.

It was reported that for the organic molecules on metal via non-covalent bonding, after the adsorption of organic molecules on metal, the Fermi level (charge neutrality level (CNL)) of the molecular orbitals tend to align with the Fermi level of the substrate. The charge transfer direction at the interface depends on the relative value of the CNL with the metal work function. If the organic molecular CNL is higher than the metal work function, the electrons will be transferred from the organic molecules to the metal, giving rise to an electrostatic dipole at the interface. This dipole will shift the relative energy levels of both materials in the direction of aligning the CNL and metal work function (ϕ_M)[17, 18]. The similar regime can be used to analyze the adsorption of organic molecules on graphene via the electrostatic interaction. The near-zero charge transfer from NiPc molecules to the neutral AA-stacked bilayer graphene indicates the graphene Fermi level (Dirac point) is at the similar energy level to the CNL states of the NiPc molecules. There are only image potential and pillow effect existing at the NiPc molecular layer/ neutral graphene interface.

For the n-doped graphene on SiC (0001), the Fermi level is at 0.4eV higher energy than the Dirac point. After the adsorption of NiPc molecules on n-doped graphene, the Fermi level of the graphene will be at a higher energy than the CNL energy level of NiPc molecules. The non-equivalence of the Fermi level at the NiPc/ n-doped graphene interface would lead to a small charge transfer from n-doped graphene to NiPc molecules.

In STS measurement for NiPc molecules on n-doped graphene, the HOMO-LUMO gap (from 1.27eV to 1.46eV with the set-point bias voltage varies from +1.0V to +2.0V) is a little narrower than the calculated gap of the NiPc molecules on neutral AA-stacked bilayer graphene (1.46eV), indicating a little metalization of NiPc molecules on n-doped graphene. It is consistent with the small charge transfer from n-doped graphene to NiPc molecules.

Based on the weak coupling between the NiPc molecules and graphene/ SiC (0001), we can analyze the spectroscopy results shown in section 4.4. The first feature is the asymmetric I-V curve and the missing of HOMO resonance peak in the molecular centers. The asymmetry of the I-V curves depends on both the asymmetric energy states with respect to the Fermi level and the asymmetric position of the molecular layer in the tunneling gap[19, 20]. The DFT calculation showed the HOMO DOS is dominated by the π states of C atoms in Pc ring. The little contribution from Ni^{2+} and N atoms explains the missing of the HOMO resonance peak in the molecular centers, therefore, the tunneling current starts increasing at a higher negative potential (the zero-current region is wider) in the molecular center. It exhibits a smaller tunneling current at the same energy position in the I-V curves than that on the molecular lobes.

The second feature of the $dI/dV-V$ curve for NiPc molecules is the shift of the molecular resonance peaks with the variation of the tip-sample separation. Specifically, with the set-point bias voltage varies from +2.0V to +1.2V, the HOMO-1 peak shifts 0.47eV, HOMO peak shifts 0.19eV, and LUMO peak shifts

0.22eV towards Fermi level, respectively. The shift of HOMO and LUMO peaks leads to the shrink of the HOMO-LUMO gap.

Because of the weak coupling between NiPc molecules and graphene, the NiPc molecular layer-graphene interface has a pure capacitive nature instead of ohmic characteristic. The electron tunneling barrier can be considered as two parts: tip-molecular layer and molecular layer-substrate. To figure out the reason for the molecular orbitals shift, the electron tunneling process needs to be analyzed. The electronic properties of graphene epitaxial grown on 6H-SiC (0001) have been discussed in Chapter 3. Specifically, the SiC substrate is a wide band gap semiconductor with a valance band at -2.0eV and a conduction band at +1.0eV. For monolayer graphene on SiC (0001), the band gap is zero, and the Dirac point is at 0.4eV below Fermi level because of the n-doping from SiC. The electron tunneling model is shown in the Figure 4.11.

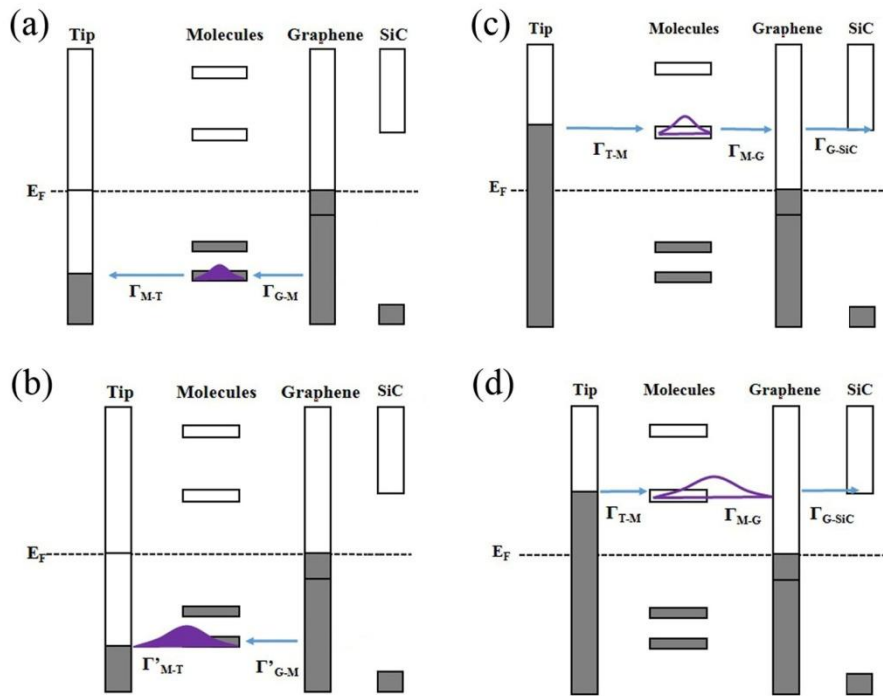


Figure 4.11 The electron tunneling schematic diagram at negative and positive bias voltages. (a) and (b) show the electron tunneling schematic diagram when the sample is negatively charged with the decrease of tip-sample separation; (c) and (d) present the electron tunneling schematic diagram when the sample is positively charged with the decrease of tip-sample separation.

In the spectroscopy measurement, the tip DOS is considered to be uniform since we used a metal tip. Therefore, the peaks in the NDC curves reflect the DOS contribution from the NiPc molecular layer and the substrate. Considering the NiPc molecular orbitals, we can analyze the STS curves over different energy ranges. In the negative energy range of the dI/dV curve, the sample is negatively charged, and the electrons tunnel from graphene to the tip via the NiPc molecular occupied states (HOMO or HOMO-1). We can label this tunneling probability as Γ_{G-M} , and the tunneling probability from the molecular occupied states to the tip Fermi level as Γ_{M-T} . During tunneling, the d-orbitals in the molecules approach to the tip, while the π electrons are less affected, because they are conjugated and strongly bound to the backbone of the molecules. This local polarization of the metal atom site reduces the

electron density in the molecule, giving a more positively charged molecule. When a high bias voltage is applied (-2.0V), the tip is far away from the molecular layer, and so the electron tunneling probability Γ_{G-M} is higher than Γ_{M-T} . With the decrease of the set-point bias voltage, the tip-sample separation decreases, the d-orbitals in the molecules are approached to the tip. Because of the narrow tunneling barrier between the tip and molecular layer combined with the electron density from the d-orbital polarization, the tunneling rate of Γ_{M-T} increases to Γ'_{M-T} . At the same time, the tunneling rate Γ_{G-M} decreases a little to Γ'_{G-M} due to the lower electron density between the molecular layer and graphene (see Figure 4.11 (a) and (b)). Therefore, with the decrease of the set-point bias voltage (smaller tip-sample separation), the tunneling rate $\Gamma'_{M-T} > \Gamma'_{G-M}$, which causes the NiPc molecules transform from negatively charged to neutral and then to positively charged, the occupied molecular orbitals shift closer to the Fermi level. Because the molecular orbital resonance peak depends on both the molecular orbitals compared to the Fermi level and the molecular layer position in the tunneling barrier. If the HOMO and LUMO orbitals are symmetric compared to the Fermi level, then the resonance peaks arising from the symmetric spectroscopy curves can be deduced as the neutral molecular orbitals energy levels (Because of the same electron tunneling probability in the two tunneling barriers).

The LUMO peak shifts about 0.22eV as the bias voltage is reduced from +2.0V to +1.0V. In the positive energy range in STS, the sample is positively charged. The electrons are injected from the tip to graphene via the unoccupied molecular states. During the tunneling, the d-orbitals in the molecular layer are attracted to the substrate (graphene), which increases the electron density between the molecular layer and the graphene. When a high bias voltage is applied, the electron rate Γ_{T-M} is smaller than Γ_{M-G} . As the bias voltage is decreased, the electron density between tip and molecular layer increases, Γ_{T-M} improves greatly to Γ'_{T-M} . At the same time, Γ_{M-G} also increases a little bit because of the higher electron density. If the electron

tunneling rate between the tip and the NiPc molecular layer is smaller than that between molecular layer-graphene interface $\Gamma_{T-M} < \Gamma_{M-G}$, the molecular layer has an effective positive charge. When the bias voltage decreases to a certain value, the electron tunneling rate between tip and molecular layer is higher than that between molecular layer-graphene interface, $\Gamma'_{T-M} > \Gamma'_{M-G}$, the molecules will tend to negatively charged, and LUMO shift closer to the Fermi level (see Figure 4.11 (c) and (d)). The molecular orbitals shift with the variations of the tip-sample separation confirms the weak coupling between NiPc molecules and graphene.

4.6 Conclusions

The self-assembly and electronic properties of NiPc molecules on monolayer graphene/ 6H-SiC (0001) substrate are discussed in this chapter. The single layer NiPc molecules form a close-packed square lattice on graphene and they display the topography of four lobes with a depression in the center. The molecular orientations depend on the molecule-molecule interaction, while the molecular lattice direction relies on the graphene symmetry underneath. NiPc molecules are physisorbed on neutral graphene via the van der Waals force, whereas, there is a small charge transfer from n-doped graphene to NiPc molecules. With the variations of the tip-sample separation, the molecular orbitals shift because of the molecular charging during tunneling and the capacitive nature of the molecule-graphene interface.

4.7 Bibliography

- [1] M. S. Liao and S. Scheiner. Electronic structure and bonding in metal phthalocyanines, Metal=Fe, Co, Ni, Cu, Zn, Mg. *J. Chem. Phys.*, 114: 9780-9791 (2001).
- [2] X. Lu and K. W. Hipps. Scanning tunneling microscopy of metal phthalocyanines: d6 and d8 cases. *J. Phys. Chem. B.*, 101: 5391-5396 (1997).

- [3] X. Shen, L. L. Sun, *et al.* Spin transport properties of 3d transition metal(II) phthalocyanines in contact with single-walled carbon nanotube electrodes. *Phys. Chem. Chem. Phys.*, 12: 10805-10811 (2010).
- [4] P. Lauffer, K. V. Emtsev, *et al.* Atomic and electronic structure of few-layer graphene on SiC(0001) studied with scanning tunneling microscopy and spectroscopy. *Phys. Rev. B.*, 77: 155426 (2008).
- [5] S. W. Poon, W. Chen, *et al.* Growth dynamics and kinetics of monolayer and multilayer graphene on a 6H-SiC(0001) substrate. *Phys. Chem. Chem. Phys.*, 12: 13522-13533 (2010).
- [6] E. Vesapuisto, W. Kim, *et al.* Growth temperature dependence of the electrical and structural properties of epitaxial graphene on SiC(0001). *Phys. Status Solidi B.*, 248: 1908-1914 (2011).
- [7] A. Nakajima, H. Yokoya, *et al.* Step control of vicinal 6H-SiC(0001) surface by H₂ etching. *J. Appl. Phys.*, 97: 104919 (2005).
- [8] Q. H. Wang and M. C. Hersam. Room-temperature molecular-resolution characterization of self-assembled organic monolayers on epitaxial graphene. *Nat. Chem.*, 1: 206-211 (2009).
- [9] A. Deshpande, C. H. Sham, *et al.* Self-assembly and photopolymerization of sub-2 nm one-dimensional organic nanostructures on graphene. *J. Am. Chem. Soc.*, 134: 16759-16764 (2012).
- [10] Y. Ogawa, T. C. Niu, *et al.* Self-assembly of polar phthalocyanine molecules on graphene grown by chemical vapor deposition. *J. Phys. Chem. C.*, 117: 21849-21855 (2013).
- [11] B. Li, K. Tahara, *et al.* Self-assembled air-stable supramolecular porous networks on graphene. *ACS Nano.*, 7: 10764-10772 (2013).
- [12] J. Meiss. Computational and experimental investigation of ultra-thin layers of NiPc, PdPc and PtPc adsorbed on HOPG by STM, STS and Gaussian98. Master, Chemnitz University of Technology (2006).

- [13] X. Lu, K. W. Hipp, *et al.* Scanning Tunneling Microscopy of Metal Phthalocyanines: d7 and d9 Cases. *J. Am. Chem. Soc.*, 118: 7197-7202 (1996).
- [14] P. Järvinen, S. K. Hämäläinen, *et al.* Self-Assembly and Orbital Imaging of Metal Phthalocyanines on a Graphene Model Surface. *J. Phys. Chem. C.*, 118: 13320-13325 (2014).
- [15] S. C. Dahlberg and M. E. Musser. Electron acceptor surface states due to oxygen adsorption on metal phthalocyanine films *J. Chem. Phys.*, 72: 6706-6711 (1980).
- [16] T. G. Gopakumar, J. Meiss, *et al.* HOMO-LUMO gap shrinking reveals tip-induced polarization of molecules in ultrathin layers: tip-sample distance-dependent scanning tunneling spectroscopy on d8 (Ni, Pd, and Pt) phthalocyanines. *J. Phys. Chem. C.*, 112: 2529-2537 (2008).
- [17] H. Vázquez, Y. J. Dappe, *et al.* Energy level alignment at metal/organic semiconductor interfaces: “Pillow” effect, induced density of interface states, and charge neutrality level *J. Chem. Phys.*, 126: 144703 (2007).
- [18] H. Vázquez, F. Flores, *et al.* Barrier formation at metal-organic interfaces: dipole formation and the charge neutrality level. *Appl. Surf. Sci.*, 234: 107-112 (2004).
- [19] S. Lei and S. D. Feyter. STM, STS and Bias-Dependent Imaging on Organic Monolayers at the Solid-Liquid Interface. Springer Berlin Heidelberg (2008).
- [20] B. Larade and A. M. Bratkovsky. Current rectification by simple molecular quantum dots: An ab initio study. *Phys. Rev. B.*, 68: 235305 (2003).

Chapter 5

Electronic Properties of Pt-Tetraphenylporphyrin Molecules on Graphene

Table of Contents

5.1 Introduction.....	108
5.2 Experimental Procedure.....	109
5.3 Self-Assembled PtTPP Molecules on Graphene.....	110
5.3.1 Self-Assembled PtTPP Molecules on Graphene/ SiC (0001).....	110
5.3.2 Self-Assembled PtTPP Molecules on Graphene/6H-SiC (000-1).....	118
5.4 Scanning Tunneling Spectroscopy of PtTPP Molecules on Graphene.....	121
5.5 DFT Calculations of PtTPP Molecules on Graphene.....	124
5.5.1 PtTPP Molecular Network on Graphene.....	124
5.5.2 Topography and Electronic Properties of PtTPP on Graphene.....	126
5.5.3 Electronic Coupling between PtTPP Molecules and Graphene.....	131
5.6 Conclusions.....	135
5.7 Bibliography.....	136

5.1 Introduction

In contrast to the planar geometry of NiPc molecules discussed in the previous chapter, the backbone of the porphyrin molecules is not usually planar but is distorted either by doming or by ruffling. The distortions can be the results of the molecule trying to accommodate a central atom which is larger or smaller than the central hole, but also from the packing interaction. Among the metal-porphyrin molecules, the PtTPP molecule in the gas phase is reported to be domed, wherein, the expected phenyl groups are titled at an angle of 79.6° with respect to the (001) plane, and the inner pyrrole ring an angle of 12° [1, 2]. For the central Pt^{2+} coordinated to four N atoms, it has an electron configuration of $5\text{d}8$. The spin state is zero, the same as that of the Ni^{2+} in the NiPc molecule (in the same group). However, the Pt atom ($Z=194$) is much heavier than Ni (58). It was reported that the neutral Pt (II)-porphyrins (PtP) are non-magnetic, but the ionized form carries a magnetic moment of one Bohr magneton[3]. The adsorption study for hundreds of PtP molecular layers on graphene showed a gate-tunable magnetism. The hypothesis is that the graphene electronic structure tends to kept neutral in the system (Dirac point is at Fermi level), the charge transfer direction depends on the polarity of the external gate bias (If graphene is n-doped, the charge transfer is from graphene to molecule, if graphene is p-doped, the charge transfer direction is the opposite) [4]. However, the electronic interaction between molecular layer and graphene was not confirmed in this study. To better understand the magnetic properties of PtP molecules on graphene, it is fundamental to study the electronic coupling between PtP molecules and graphene in the equilibrium state. This is the motivation of our study for the adsorption of PtTPP molecules on graphene.

Here, we used the STM to probe the structure and electronic properties of the PtTPP molecules adsorbed on both neutral and n-doped graphene; in particular, the position

of the Pt atoms with respect to the graphene lattice, and any charge transfer which might be detected using STS.

5.2 Experimental Procedure

In this study, the meso-substituted PtTPP molecules with functional group of CO_2CH_3 (CO_2Me) was used. The molecular structure and the sample of molecular powder in purple color is shown in Figure 5.1. In the experiment, the graphene terraces on both Si-terminated 6H-SiC and C-terminated 6H-SiC substrates were prepared following the procedures described in Chapter 3. On the Si-terminated SiC substrate, mostly monolayer graphene and a small percentage of bilayer graphene were obtained, according to the LEED observations and topography measurements by STM. After that, the $\text{PtTPP}(\text{CO}_2\text{Me})_4$ molecules were cleaned by several cycles of degassing at 200 °C. Then, the molecular powder in the Quad Dopant Source was deposited on graphene by resistive heating at 248 °C for 60s. During the deposition, the sample was held at room temperature with an initial pressure of 4.0×10^{-10} mbar. Subsequently, the same sample was post-annealed at the increasing temperatures (~100°C, ~150°C, ~200°C, and ~250°C). After each annealing, the surface was imaged by STM.

On the C-terminated SiC substrate, multilayer graphene was grown with an azimuthal disorder. The topography and electronic properties of multilayer graphene are discussed in Chapter 3. After degassing, the $\text{PtTPP}(\text{CO}_2\text{Me})_4$ molecules were deposited on graphene substrate at 240°C for 40s, followed by post-annealing at about 200°C.

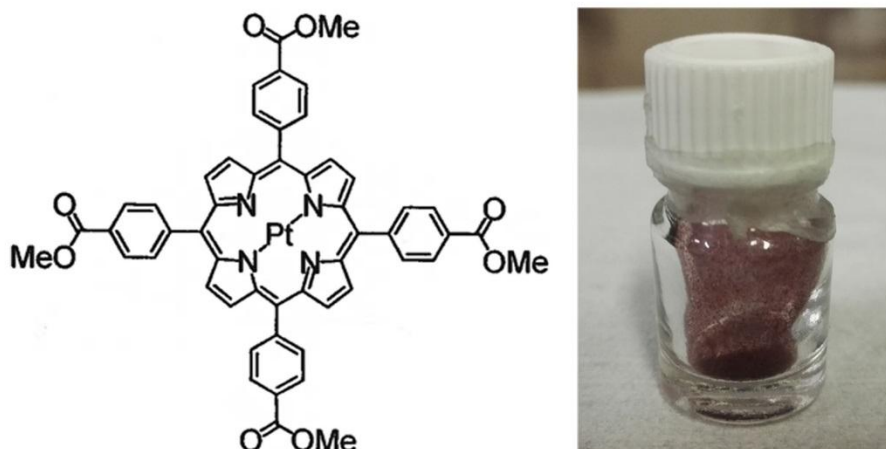


Figure 5.1 The molecular structure of PtTPP(CO₂Me)₄ and the molecular powder in a purple color.

The topography of the PtTPP(CO₂Me)₄ molecules on graphene was observed by room-temperature STM (10^{-11} mbar). The electronic interactions between the molecules and graphene were probed by scanning tunneling spectroscopy measurements (I-V) with the feedback loop off. The normalized differential conductivity (NDC) was obtained by dividing the smoothed first derivative of I-V curves (dI/dV) with smoothed I-V curves. The purpose of smoothing is to avoid the artificial mathematical errors produced in the normalized differential conductivity calculation. The STM images and spectroscopy were processed by the free software ‘WSXM’. DFT calculations of PtTPP(CO₂Me)₄ molecules on free-standing monolayer graphene taking into account van der Waals interactions were performed by Dr. Yannick Dappe at the SPEC laboratory in the IRAMIS of CEA to understand the electron coupling regime between the PtTPP(CO₂Me)₄ molecules and graphene.

5.3 Self-Assembled PtTPP Molecules on Graphene

5.3.1 Self-Assembled PtTPP Molecules on Graphene/ SiC (0001)

The 50nm×50nm STM image of PtTPP(CO₂Me)₄ molecules on graphene/ 6H-SiC (0001) show a well-ordered close packed molecular domain with a 5×6 array of

molecular vacancies (Figure 5.2 (a)). Within the square vacancy array, well-ordered molecules can also be seen at a lower level, which suggests there are two molecular layers on graphene/ 6H-SiC (0001). The measured height between the top and bottom molecular layer inside the vacancy array is 4.91 Å (see Figure 5.2 (b)). A step edge between the adjacent molecular layers is shown in Figure 5.2 (c). Molecular diffusion occurs during STM tip scanning because of the higher degree of freedom for the molecules at the edge than that in the molecular domain. The black line profile in Figure 5.2 (d) shows a step height of 5.18 Å, consistent with the measured molecular layer separation in Figure 5.2 (b), which confirms the double-molecular layers on graphene/ SiC (0001) substrate. Both molecules in the bottom and top layers show a near-square lattice with the same lattice direction, the averaged lattice constants are 1.72 nm × 1.64 nm with an angle of 90 ° (± 3 °). The molecular position on the top layer (red lines) shifts 4.9 Å (± 2.4 Å) in both molecular lattice directions compared with that on the bottom layer (green lines). It is reported that the porphyrin molecules form a commensurate unit cell with the respective substrate, ensuring the most effective geometric lattice matching. The ZnTPP molecules can form a monoclinic crystal with a flat macrocycle[5]. PtTPP thin film has a body centered tetragonal unit cell on a KCl (100) substrate. The molecular centers shift 6.69 Å between the adjacent molecular layers in both molecular array directions, while on Cu (110)-(2×1)O substrate, the PtTPP thin film shows a triclinic phase, with the shift of 0.72 Å[6]. In my experiment, the PtTPP(CO₂Me)₄ molecules form a near-square lattice network on graphene, giving that the molecular shifts between the adjacent molecular layers in both lattice directions are within the range of (0.72 Å, 6.69 Å). We can suggest that the PtTPP(CO₂Me)₄ molecular thin film on graphene might also form a triclinic unit cell, in which, the molecules in top and bottom molecular layers have an offset-face-to-face stacking.

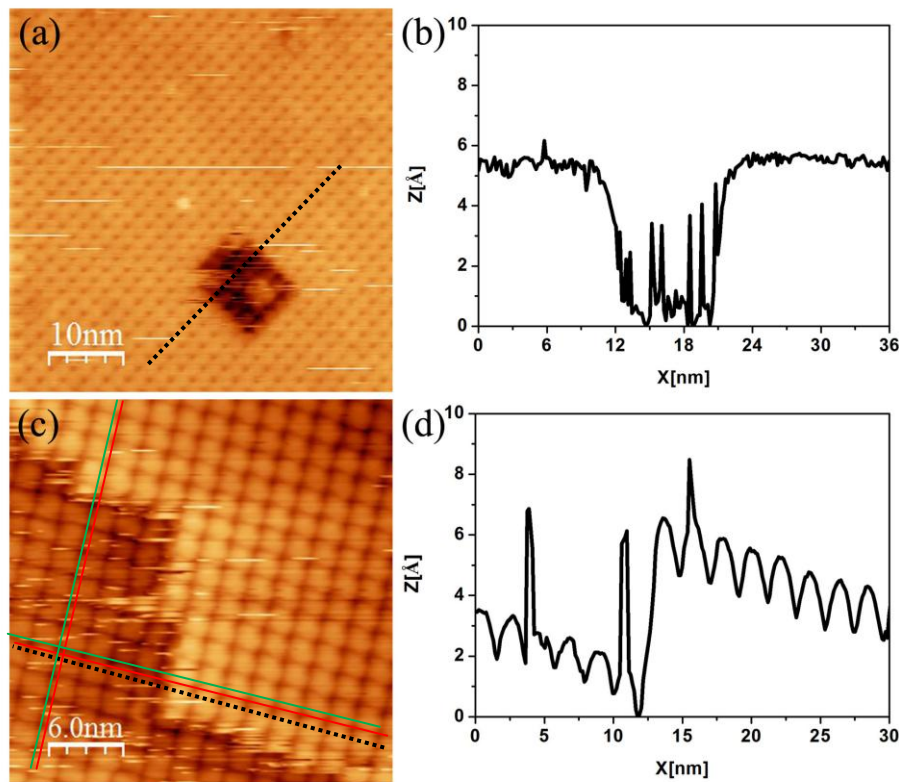


Figure 5.2 Bilayer $\text{PtTPP}(\text{CO}_2\text{Me})_4$ molecules on graphene/ SiC (0001). (a) $50\text{nm}\times 50\text{nm}$ STM image of molecular domain, tunneling condition: $V=-3.3\text{V}$, $I=0.1\text{nA}$; (b) The step height of 4.91\AA between the top and bottom molecular layers; (c) $30\text{nm}\times 30\text{nm}$ STM image of molecular domains, tunneling condition: $V=-3.0\text{V}$, $I=0.1\text{nA}$, the green lines are aligned with the molecular array in the bottom molecular layer, and the red lines with the molecular array direction in the top molecular layer; (d) The spacing between the top and bottom molecular layers is 5.18\AA .

Another step is observed in the molecular domains, where the molecules grow across the step without changing the molecular lattice direction or molecular positions (see Figure 5.3 (a)). The measured step height is 4.32\AA , it could be deduced as the monolayer-bilayer graphene terrace space. Furthermore, several types of molecular vacancies are found in the molecular network on graphene: single, double, and triple molecular vacancies. The averaged depth of the vacancies is 2.96\AA , which is smaller than the measured underlying molecular layer of 4.91\AA . There are two possible explanations for this difference. (i) A single molecular vacancy is too small for the tip

to reach to bottom, due to the response lag of the tip feedback loop at the vacancy sites; (ii) Another case is the extra adsorbates on molecule, for example a hydrogen atom. It is reported the H adsorption on Pt surface leads to a decrease of the electron density of the Pt atom, giving rise to a reduction on surface Pt charge of 0.32e[7]. Whereas, the lower DOS in the STM image is extended in the whole molecular region instead of the molecular center. It is more likely caused by the missing of the molecules in the molecular network rather than the adsorption of the H atom on Pt. The single, double, triple and a rectangular region of molecular vacancies imply the weak in plane molecule-molecule interactions.

Figure 5.3 (b) shows the isolated molecules adsorbed on top of the well-ordered molecular network, with a height of 6.36Å ($\pm 0.20\text{\AA}$). A disordered aggregate of molecular region is observed (at the upper right of the image), this distorted region edge causes a dislocation of the molecular array of 0.45Å, as the dotted polyline shown in Figure 5.3 (b) .

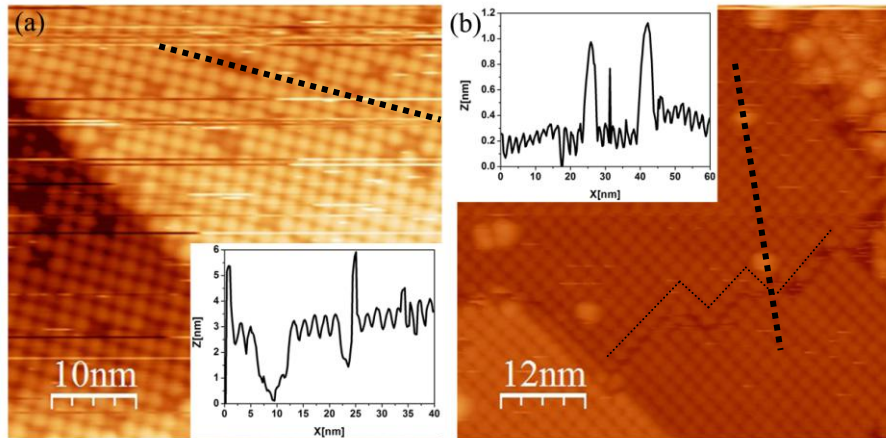


Figure 5.3 (a) PtTPP(CO_2Me)₄ molecules seamlessly grow across the graphene step (5.93Å) on 6H-SiC(0001). There are several molecular vacancies: single molecule, double-molecules, triple-molecules. The measured vacancy depth is 2.96Å, tunneling condition: V=-3.7V, I=0.1nA; (b) Isolated molecules are adsorbed on molecular network on graphene/6H-SiC (0001), the measured height of single molecules on the molecular network is 6.36Å, tunneling condition: V=-3.5V, I=0.1nA.

Apart from the adsorption of isolated molecules on top of the molecular network and the molecular vacancies, different molecular domain directions are also observed on graphene. Figures 5.4 (a) and (b) reveal two PtTPP(CO₂Me)₄ molecular lattices with a rotation angle of 21°. In Chapter 4, the NiPc molecular lattice direction was shown to depend on the graphene symmetry: the molecular array is aligned along the armchair and zigzag directions with a lattice angle of 90°. Because the adjacent armchair and zigzag angle of monolayer graphene is 30°, the 21° rotation angle of PtTPP(CO₂Me)₄ molecules on graphene/ SiC (0001) could be deduced as the molecular array directions along armchair and zigzag of monolayer graphene with a deviation angle of 4.5°. To confirm the hypothesis, the molecular lattice model is shown in Figure 5.4 (c). The self-assembled molecules form a near square lattice on graphene and the averaged molecular lattice parameters are 1.72nm×1.64nm with an angle of 90°(± 3 °). All the molecular domain directions summarized from the STM images are displayed as the black lines in Figure 5.4 (d). These directions can be averaged as three molecular lattice directions with an averaged angle difference of 30°(± 3 °) (see the yellow lines in Panel (d)). It can be deduced as the combination of PtTPP(CO₂Me)₄ molecular C_{2v} symmetry and graphene three-fold symmetry. Whereas, the molecular lattice directions are more dispersed compared with the lattice directions of NiPc molecules on graphene. It might be the result of the molecular topography evolution with the post annealing, as shown in Figure 5.5.

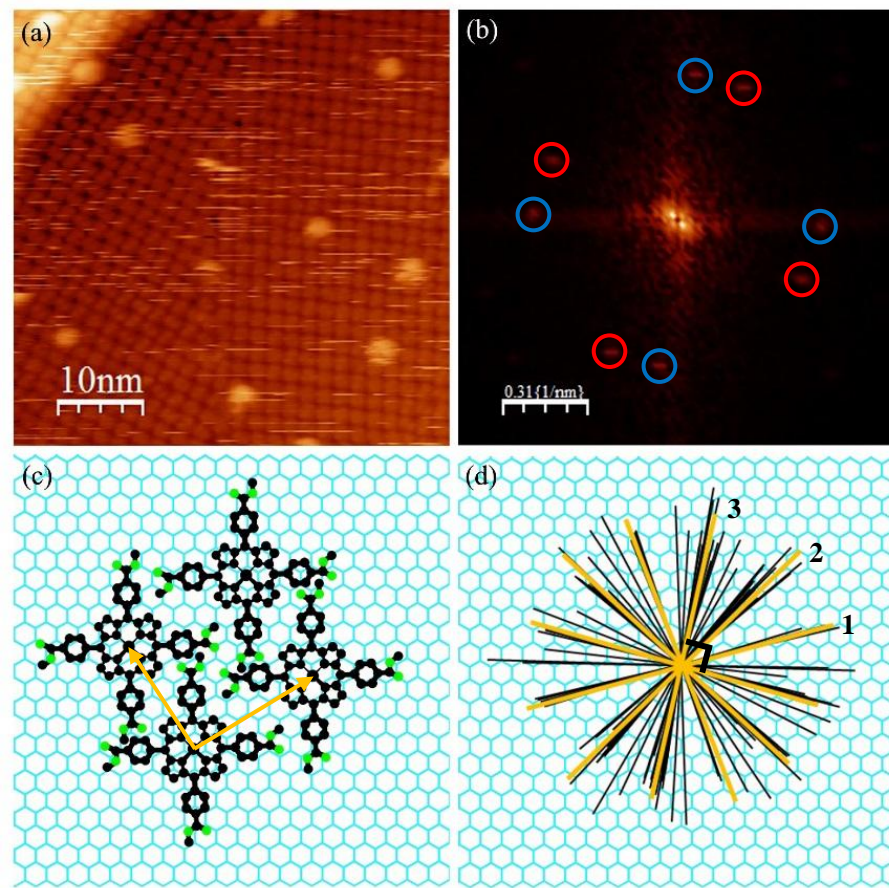


Figure 5.4 (a) The 50nm× 50nm STM image of molecular network on graphene/ 6H-SiC (0001), tunneling condition: V= -3.5V, I=0.1nA; (b) The FFT pattern shows two molecular lattice directions with a rotation of 21 °, (c) The molecular square lattice pattern on graphene; (d) The black lines are all the molecular lattice directions summarized from the STM images, the yellow lines are the three averaged molecular lattice directions.

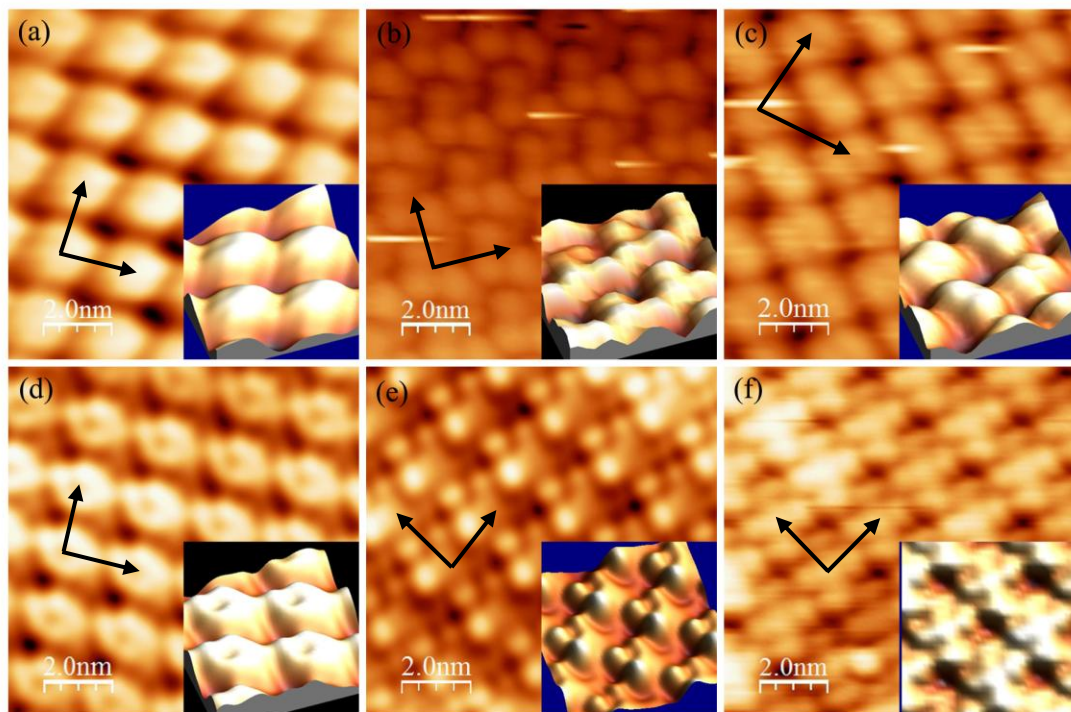


Figure 5.5 Bias-dependent ($10\text{nm} \times 10\text{nm}$) STM images of PtTPP ($\text{CO}_2\text{Me})_4$ molecules on graphene/SiC (0001) with the post-annealing. (a) Tunneling condition: $V=-3.7\text{V}$, $I=0.1\text{nA}$, post-annealing at 100°C for 150min, 150°C for 70min, 200°C for 150min; (b) Tunneling condition: $V=-3.5\text{V}$, $I=0.1\text{nA}$, post-annealing at 100°C for 150min, 150°C for 70min, 200°C for 180min, 250°C for 210min; (c) Tunneling condition: $V=-3.5\text{V}$, $I=0.1\text{nA}$, post-annealing at 100°C for 150min, 150°C for 70min, 200°C for 180min, 250°C for 300 min; (d) Tunneling condition: $V=-3.0\text{V}$, $I=0.1\text{nA}$, post-annealing at 100°C for 150min, 150°C for 70min; (e) Tunneling condition: $V=-3.0\text{V}$, $I=0.1\text{nA}$, post-annealing at 100°C for 150min, 150°C for 70min, 200°C for 180min, 250°C for 90min; (f) Tunneling condition: $V=-2.7\text{V}$, $I=0.1\text{nA}$, post-annealing at 100°C for 150min, 150°C for 70min, 200°C for 180min and 250°C for 240min. The insets in each Panels display the 3D molecular topographies at the corresponding bias voltage and post-annealing condition.

Figure 5.5 shows the bias-dependent small-scale images of the bilayer PtTPP($\text{CO}_2\text{Me})_4$ molecules on graphene/ SiC (0001) after annealing at the increased temperatures step by step (100°C , 150°C , 200°C and 250°C). Due to the ruffling of the PtTPP($\text{CO}_2\text{Me})_4$ molecule, the STM images depend on both the geometry and

the LDOS of the molecules. The stable STM images of molecular topography only can be imaged at high bias voltages (large tip-sample separation), because of the diffusion of isolated molecules adsorbed on top of the molecular network.

Even though the MTPP molecular deformation is restricted in the self-assembled molecular network[2], the PtTPP(CO₂Me)₄ molecular topography evolutions with bias voltages and post-annealing temperatures are clearly observed in Figure 5.5. When the bias voltage is -3.7V, after annealing at 100°C for 150min, 150°C for 70min and then 200°C for 150min, the molecular network with a square lattice is clearly seen, however, the intra-molecular contrast is not reflected because of less electron overlap between tip and molecules (see Figure 5.5 (a)). When the bias voltage is -3.5V after annealing at 100°C for 150min, 150°C for 70min, 200°C for 180min and then 250°C for 210min, the molecules show an asymmetric four lobes with a depression in the center: three lobes are prominent, the other one is fainter with a smaller DOS extension (see Figure 5.5 (b)). When the sample is further annealed at 250 °C for 90min, the molecules show two large lobes with a depression in the center. It is similar to the classic saddle-like MTPP molecules on metallic substrate, except to the central depression. In addition, the self-assembled molecules are in general more closely packed, the adjacent molecular geometry is rotated 90 °; leading to a lattice of 2.25nm×2.08nm with an angle of 100 °(see Figure 5.6 (c)). The two prominent lobes might be the contribution of the two opposing bent-up pyrrole rings. When the bias voltage is -3.0V, after annealing sample at 100°C for 150min and 150°C for 70min, a four-lobed structure with a faint center molecular topography was observed (see Figure 5.5 (d)). After further annealing at 200°C for 180min and 250°C for 90min, similar to the topography in Figure 5.5 (a), the molecule displays an asymmetric four lobes but with a flat center (see Figure 5.5 (e)). When the bias voltage is -2.7V after annealing at 100°C for 150min, 150°C for 70min, 200°C for 180min and then 250°C for 240min, the molecules exhibit an apparent four lobes with a prominent center (see Figure 5.5 (f)). In summary, with the decrease of the bias

voltage, the molecules transform from dark center ($V=-3.5V$) to prominent center ($V=-2.7V$). While, at the same bias voltage, the different post annealing parameters lead to the transformation of the molecular topography. The molecular topography evolution with the bias voltage and annealing temperatures will be discussed in the DFT calculation section in more detail.

5.3.2 Self-Assembled PtTPP Molecules on Graphene/6H-SiC (000-1)

For the $\text{PtTPP}(\text{CO}_2\text{Me})_4$ molecules on graphene/ SiC (000-1), at the deposition parameter of 240 °C for 40s, the molecules also form the close-packed molecular network, however no any steps caused by the different molecular layers were observed. The only step type detected in the molecular domains is the step between different graphene terraces (see Figure 5.6 (a)), where the molecules seamlessly grow across the steps without any molecular lattice shift. From the measured step height of 4.2 Å ($\pm 1.3 \text{\AA}$), the step corresponds to the distance between monolayer and bilayer graphene terraces. From the step features in the molecular domains, we can deduce that there is only single molecular layer on graphene/ 6H-SiC (000-1).

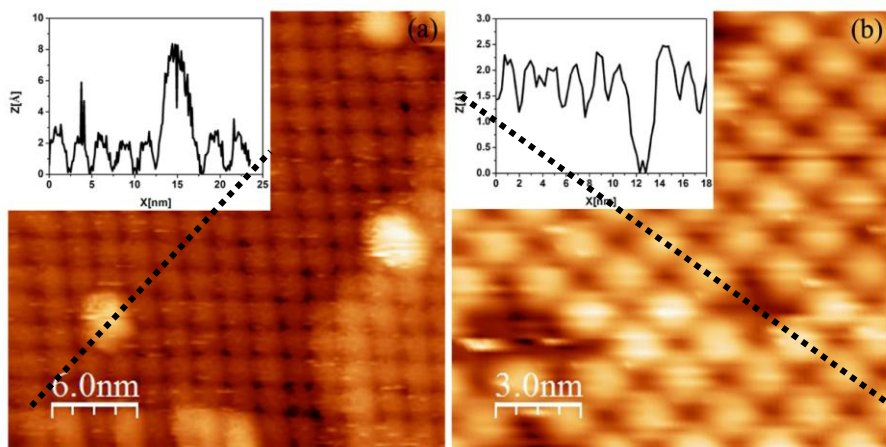


Figure 5.6 (a) Molecules grow across the graphene step of 4.2\AA (monolayer-bilayer terrace step) on 6H-SiC (000-1). In addition, there are several isolated molecules adsorbed on top of the molecular network, the space between adsorbed molecules and molecular network is 5.67\AA , tunneling condition: $V=-3.5\text{V}$. $I=0.1\text{nA}$; (d) Both single and triple molecular vacancies are found in molecular network on graphene/ 6H-SiC (000-1), tunneling condition: $V=-3.7\text{V}$, $I=0.1\text{nA}$.

Same as that on graphene/ SiC (0001), several isolated molecules adsorbed on top of the well-ordered molecular network are observed on graphene/ SiC (000-1). The measured height of the isolated molecules on top of the molecular network is 5.67\AA ($\pm 0.27\text{\AA}$), matching the value measured on graphene/ SiC (0001). Furthermore, both single and triple molecular vacancies are found in the molecular network on graphene/ 6H-SiC (000-1) (see Figure 5.6 (b)). The measured depth of the vacancies is 2.24\AA , similar to the depth value in the molecular network on graphene/ SiC (0001). The isolated molecule adsorbed on molecular network and the various molecular vacancies in the molecular network indicate the weak in-plane molecule-molecule interaction.

For PtTPP (CO_2Me)₄ molecules on graphene/ 6H-SiC (000-1), the self-assembled molecules also form a square lattice, as shown in Figures 5.7 (a) and (c). The lattice parameters are 1.71nm ($\pm 0.12\text{nm}$) $\times 1.59\text{nm}$ ($\pm 0.08\text{nm}$) with an angle of 91° ($\pm 6^\circ$), similar to that on graphene/ SiC (0001). From both STM image (Figure 5.7 (a)) and

FFT pattern (Figure 5.7 (b)), three molecular lattice domains are observed with rotation angles of 19° and 23° , respectively. Because of the azimuthal disorder of multilayer graphene on C-terminated SiC substrate, the honeycomb or triangular lattice of graphene is twisted, resulting in the disruption of the graphene symmetry. The molecular lattice directions on graphene/ 6H-SiC (000-1) in the experiment are summarized in Figure 5.7 (d). They are disorganized, compared with the molecules on graphene/ SiC (0001). The azimuthal disorder of multilayer graphene on SiC (000-1) makes the self-assembled molecular lattice directions complex, indicating the molecular lattice direction depends on both the graphene terrace directions and graphene substrate symmetry. The small-scale ($10\text{nm}\times10\text{nm}$) STM image of PtTPP(CO_2Me)₄ molecules on graphene (Figure 5.7 (c)) does not show the apparent intra-molecular contrast, however, it is clear that the molecular DOS is dominated by the pyrrole rings, instead of the phenyl groups.

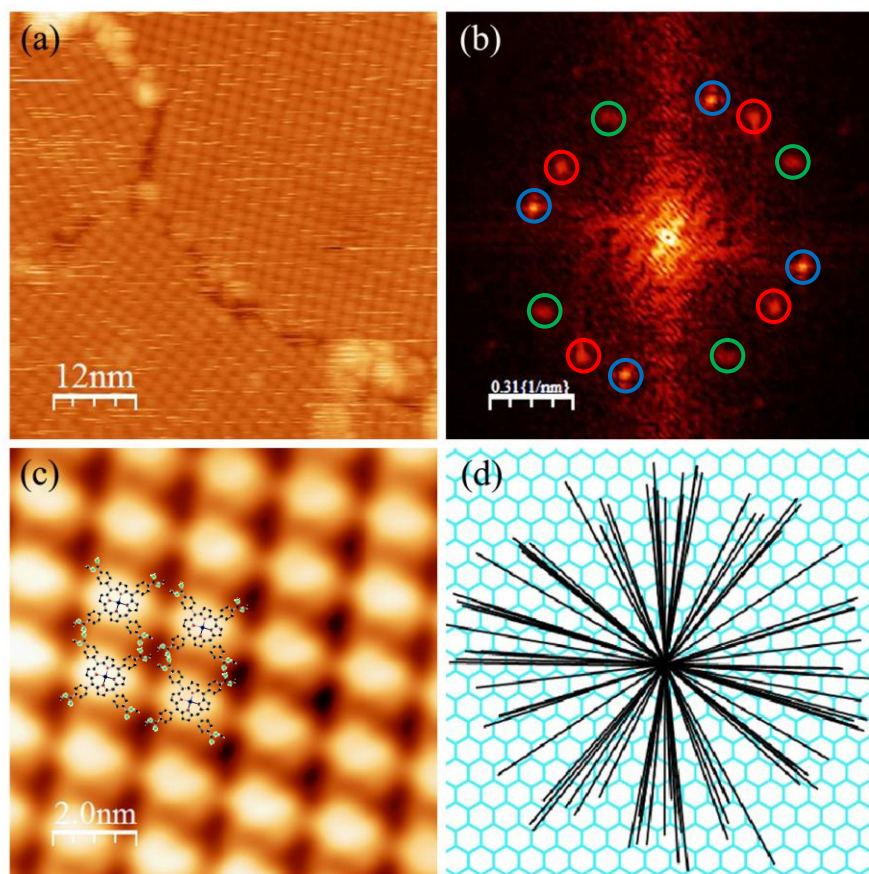


Figure 5.7 (a) 60nm×60nm STM image of molecular network on graphene/ 6H-SiC (000-1), tunneling condition: V=-3.5V, I=0.1nA; (b) The FFT pattern reveals three molecular lattice directions in Panel (a), the angle differences are 19° and 23°, respectively; (c) 10nm×10nm STM image of PtTPP(CO₂Me)₄ molecules on graphene/ SiC (000-1), tunneling condition: V=-3.5V, I=0.1nA; (d) Different molecular lattice directions on graphene/ 6H-SiC (000-1).

5.4 Scanning Tunneling Spectroscopy of PtTPP Molecules on Graphene

The electronic properties of PtTPP(CO₂Me)₄ molecules on both graphene/ SiC (0001) and graphene/ SiC (000-1) were studied by scanning tunneling spectroscopy. The normalized differential conductance (NDC) curves at different set-point bias voltages are exhibited in Figure 5.8. For the STS curves of molecules on graphene/ SiC (0001) in panel (a), with a set-point bias voltage of -3.7V, only one molecular resonance peak

at -2.58eV was detected. With a set-point bias voltage of -3.0V, resonance peaks in both the occupied states and unoccupied states are detected; the peak positions are at -2.21eV and +2.34eV, respectively. When the set-point bias voltage is decreased further to -2.5V (smaller tip-sample separation), the peak positions shift to -2.04eV and +2.02eV, respectively. The resonance peak at -2.04eV is assigned to the HOMO orbital, confirmed by the DFT calculation presented in the next section.

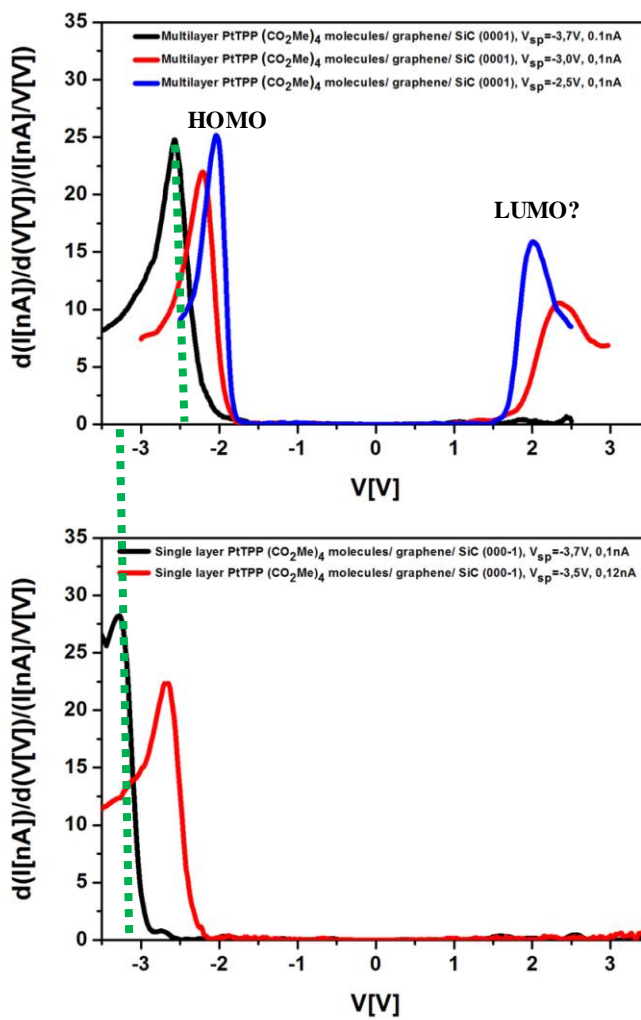


Figure 5.8 The normalized differential conductance of PtTPP(CO_2Me)₄ molecules on both graphene/SiC (0001) (Panel (a)) and graphene/ SiC (000-1) (Panel (b)) at different set-point bias voltages.

With the decrease of the tip-sample separation, the molecular resonance peaks (both occupied states and unoccupied states) shift closer to Fermi level, similar to the NDC curve features of NiPc molecules on graphene. The STM-based spectroscopy of quantum dots was first reported by Bakkers et al[8]; the relative rate of electron tunneling into, versus tunneling out of the dot could be changed by varying the tip-dot distance. If the tip was far from the dot, the tunneling into the dot was slower than tunneling out of the dot, resulting in single electrons tunnel through the dot. If the tip was closer to the dot, the tunneling into the dot became as fast as tunneling out of it. The maximum electron numbers could be present in the particle was found three, which is the coulomb blockade behavior. In the tunneling spectroscopy measurements for self-assembled molecules at room-temperature, the coulomb blockade behavior could not be detected. However, the resonance peak shift with the variation of the tip-sample separation could be explained in the similar regime. With the bias voltage decreases (smaller tip-sample separation), the electron tunneling probability between the Fermi level of the tip and molecular energy states increases, while it is kept similar between molecular energy states and the Fermi level of the substrate. This tunneling probability difference in the two stages of the conductance path results in both the occupied and unoccupied states resonance peaks shift to closer to the Fermi level (The detailed explanation can be found in Chapter 4). Stroscio and Feenstra mentioned the peak shift in the dI/dV spectroscopy measurement on Si (111) surface could be eliminated by using the logarithmic derivative, $d\ln I / d\ln V - V$. However, it is clear not the same case in our experimental results[9].

For the molecules on graphene/ SiC (000-1), only spectroscopy measurements at high set-point bias voltages were obtained. With a bias voltage of -3.7V, a resonance peak appears at -3.27eV, which is 0.69eV further away from Fermi level compared to the resonance peak position on graphene/ SiC (0001) at the same set-point bias voltage. With a set-point bias voltage of -3.5V, the peak position at occupied states shifts to -2.66eV, while there is still no resonance peak detected at the unoccupied states.

In the adsorption system, the electron tunneling between tip and surface involves the molecular orbitals that extend into the vacuum space and their interaction with the surface [10-13]. Therefore, the fact that the unoccupied resonance peak cannot be detected at high set-point bias voltage (large tip-sample separation) might be the consequence of the different spatial extensions of the occupied and unoccupied molecular orbitals: the occupied molecular orbitals extend longer to the vacuum space than the unoccupied orbital does. The molecular orbitals will be discussed in detail in section 5.5.2.

5.5 DFT Calculations of PtTPP Molecules on Graphene

5.5.1 PtTPP Molecular Network on Graphene

For the isolated PtTPP (CO_2Me)₄ molecule in the gas phase, different molecular geometries can be obtained in the DFT calculation using the different codes: symmetric (VASP code) and asymmetric (Fireball code) molecular geometries. For the symmetric geometry, the opposing pyrrole rings bend in the same directions with the same angle. For the asymmetric geometry: three pyrrole rings bend upwards, while the fourth one bends down. When the molecule is adsorbed on a certain substrate, the pyrrole rings and phenyl groups tend to rearrange to increase the adsorption energy (minimize the whole energy in the system). Adsorption induced MTPP molecular deformations are widely reported on metallic substrates [2, 14, 15]. However, after the adsorption of a single PtTPP(CO_2Me)₄ molecule on graphene, the calculations indicate that the molecular geometry remains intact (VASP code). The calculated adsorption energy of a single molecule with a symmetric geometry is 3.36eV with a separation of 3.4Å from the graphene (distance between Pt atom and graphene), as seen in Figures 5.9 (a) and (b). Wherein, the two opposing pyrrole rings in molecule bend up and the other two bend down with respect to the macrocycle plane. The bending angles are around 20 ° ~ 25 °, and the adjacent phenyl

groups tilt in opposite directions with the same angle, which leads to a C_{2v} symmetry of the molecule⁹.

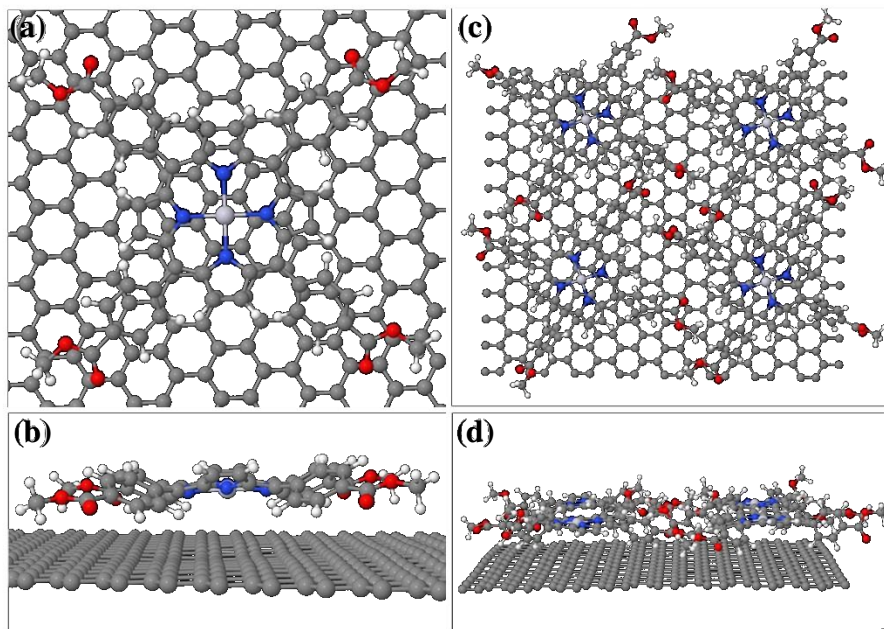


Figure 5.9 Calculated single $\text{PtTPP}(\text{CO}_2\text{Me})_4$ molecule and four self-assembled molecules on the freestanding monolayer graphene. (a) Top view of single molecule adsorbed on graphene; (b) side-view of single molecule adsorbed on graphene, the opposing pyrrole rings bend up and the other opposing pyrrole rings bend down about $20 \sim 25^\circ$; (c) Top view of four self-assembled molecules on graphene with a Pt atom adsorbed in hollow site; (d) Side-view of four self-assembled molecules on graphene.

Four $\text{PtTPP}(\text{CO}_2\text{Me})_4$ molecules are used in the calculation of the self-assembled molecular network on freestanding monolayer graphene with VASP code, and several adsorption sites for the central Pt atom were chosen (top, hollow and bridge). The equilibrium distance between molecular layer and graphene ranges between 4.0 and 4.2\AA , with the corresponding energies between 2.24 and 2.15 eV/molecule,

⁹ All the calculation results are based on the symmetric molecular geometry (VASP code).

indicating that the PtTPP molecules have no site preference on graphene. The calculated equilibrium distance of the self-assembled molecules on graphene is larger than that of the single molecule on graphene, because of the rotation of the phenyl rings caused by the molecule-molecule interaction. The self-assembled molecules with a Pt^{2+} ion adsorbed in hollow site are shown in Figures 5.9 (c) and (d). The molecules form a square lattice with an angle of 90° . Note that, the four molecules are not in the same plane parallel to the graphene; the opposite molecules are lifted up, while the other two molecules are pushed down. The separation of the Pt atoms in different molecules in the direction normal to the porphyrin plane is 0.2\AA , and the lattice constants are $2.56\text{nm}\times2.56\text{nm}$, which are larger than the parameters measured in the experiment. From the small-scale STM images of $\text{PtTPP}(\text{CO}_2\text{Me})_4$ molecules on graphene (see Figure 5.5), the Pt position shift along Z axis between the adjacent molecules are not observed, it might because of the ruffling of the molecular geometry, it is hard to reflect the precise Pt atom positions in the different molecules. In Figure 5.5 (b), after post-annealing at 250°C , a close-packed molecular network with the two-lobe molecular topographies (up-down or left-right) show a near-square lattice of $2.25\text{nm}\times2.08\text{nm}$ with an angle of 100° ; because the adjacent molecular topographies are rotated 90° . However, the molecular lattice unit cell here is still smaller than the calculated molecular lattice parameters. It might be due to the annealing induced closer packing of the molecular network.

5.5.2 Topography and Electronic Properties of PtTPP on Graphene

To interpret the $\text{PtTPP}(\text{CO}_2\text{Me})_4$ molecular topography and the electronic properties of $\text{PtTPP}(\text{CO}_2\text{Me})_4$ molecules on both graphene/SiC (0001) and graphene/ SiC (000-1), the molecular DOS on freestanding monolayer graphene was calculated. The calculated HOMO-LUMO gap of a single molecule on graphene is 1.9eV , wherein, the LUMO orbital ($+0.12\text{eV}$) is very close to the Fermi level (see Figure

5.10 (a)). This gap is as expected from the standard DFT calculations, a little smaller than the electrochemically measured PtTPP(CO_2Me)₄ molecular HOMO-LUMO gap of 2.46eV[3]. For the model of self-assembled four molecules on graphene, the HOMO-LUMO gap decreases to 1.82eV, and the molecular DOS peaks split because of the inequivalence of the four molecules on graphene (see Figure 5.10 (b)). Except the LUMO peak splitting between four molecules because of the molecule-molecule interaction, the LUMO peak for each molecule further splits into two peaks, the averaged energy difference between the two peaks is 0.08eV ($\pm 0.01\text{eV}$) (see the inset panel in Figure 5.10 (b)).

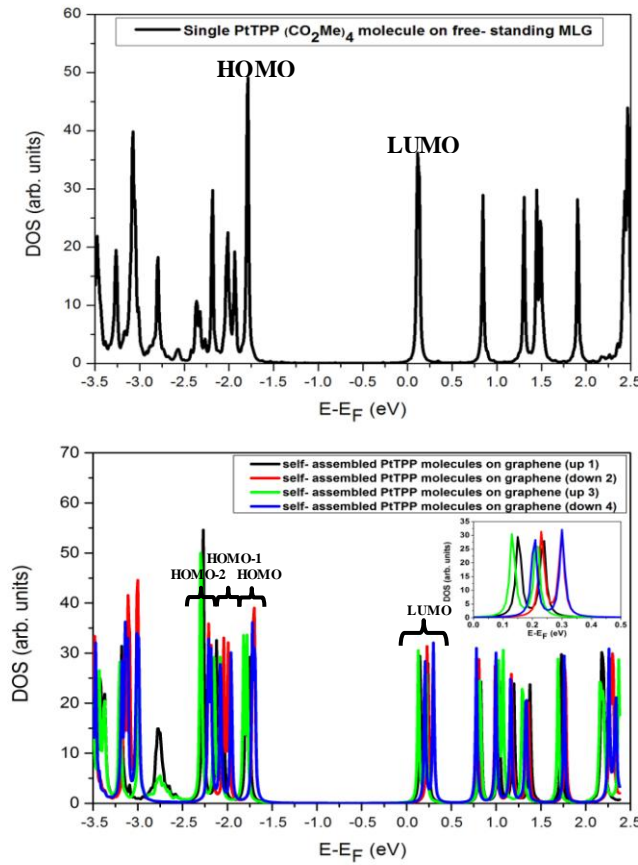


Figure 5.10 (a) Calculated DOS of single PtTPP(CO_2Me)₄ molecule on freestanding monolayer graphene; (b) DOS of four molecules self-assembled on freestanding monolayer graphene. The inset panel shows the LUMO peak splitting.

The isoDOS for each molecular orbital and the atomic DOS contribution to the single molecule on graphene are also calculated, as shown in Figure 5.11 and Table 5.1. From calculation, the HOMO orbital is at -1.8eV compared to the Fermi level and the DOS is contributed by the Pt d_{xz} , d_{yz} orbitals and p_z orbital of the pyrrole rings (see Table 5.1). The HOMO-1 is at -2.01eV, and the DOS is dominated by the $d_{x^2-y^2}$ orbital of Pt, which will not contribute to the tunneling current, because of the absence of DOS extension in the perpendicular direction to the substrate. HOMO-2 is at -2.18eV, whose DOS comes from the Pt d_z^2 and a small fraction from pyrrole rings. The HOMO-3 (-3.08eV) DOS primarily results from the p_x and p_y orbitals of CO₂Me meso group, which will not contribute to the tunneling current, either. HOMO-5 (-3.58eV) DOS are the consequence of Pt, pyrrole rings and phenyl groups. Finally, the LUMO (+0.12eV) DOS shows an e_g symmetry, which is contributed by Pt (d_{xz} , d_{yz}), pyrrole rings and phenyl groups (p_z). It is interesting to observe that the adjacent molecular DOS extension in the molecular network are perpendicular to each other (see Figure 5.11). The energy splitting of the DFT calculated LUMO peak shown in the inset panel of Figure 5.10 can be deduced as the splitting of the degenerate e_g symmetry. In addition, the LUMO DOS extension in the self-assembled molecules may indicate the possible electron or spin transport pathways through the molecular layers along the chain-like molecular DOS extension.

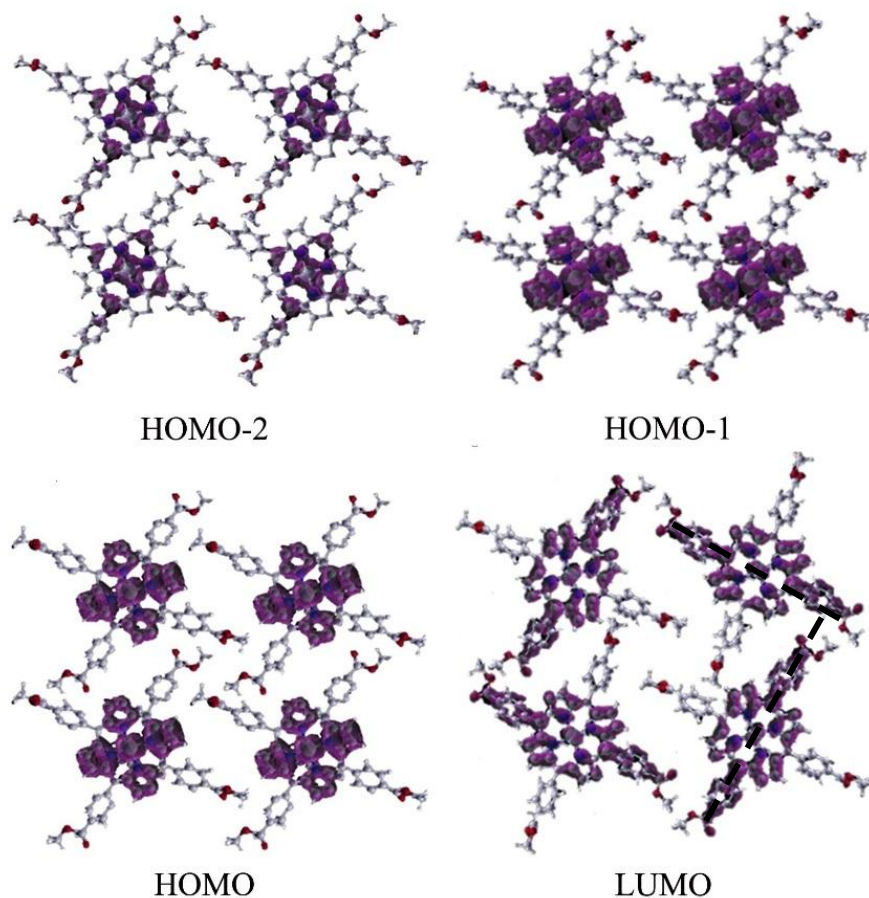


Figure 5.11. The calculated isodos of self-assembled molecular orbitals on freestanding monolayer graphene.

The small-scale STM images of double-layer $\text{PtTPP}(\text{CO}_2\text{Me})_4$ molecules with intramolecular contrast at different set-point bias voltages can be explained by the molecular energy levels and the symmetries of the molecular orbitals. According to the atomic DOS contribution in Table 5.1, when the bias voltage is -3.5V, it is the pyrrole rings that dominate the molecular DOS, whereas, the molecule shows different topographies with annealing. This confirms the molecular geometry deformation in the self-assembled molecular network. The topography in Figure 5.5 (b) can be deduced as the asymmetric bending of pyrrole rings: three pyrrole rings bend up, while the other one bends down, giving rise to the lower Pt position in the macrocycle. In Figure 5.5 (c), the two opposing pyrrole rings bend up, while the

other two bend down. The annealing at 250°C may allow molecules in the self-assembled network to overcome the transition barrier from one conformation to the other. When the bias voltage is -3.0V, the molecular orbital of HOMO-3 (-3.08eV) does not contribute to the tunneling current, because of the absence of the electron density with Z character. Same as the STM images at V=-2.7V, tunneling current mainly arises from the d orbital of Pt and π states of pyrrole rings. In Figure 5.5(d) after annealing at 150°C, the molecules show the four lobes with a depression in the center, which is due to the bending up of the four pyrrole rings. After further annealing at 250°C, three pyrrole rings bend up, while the other one bends down, similar to the asymmetric geometry in panel (a). The Pt d_{z^2} orbital contribution makes the metal center prominent. When the bias voltage is -2.7V after annealing at 250°C, the pyrrole rings tend to be flat, the molecules show clearly lobes with a prominent metal center. The molecular topography evolution with both the bias voltages and the annealing parameters indicates the weak molecule-molecule interaction.

Table 5.1 The atomic DOS contribution to single molecule on freestanding monolayer graphene.

Molecular Orbital	Pt (%)	N (%)	O free (%)	O (methyl) (%)	C (Nitrogen ring) (%)	C (phenyl) (%)
HOMO-5 (-3.53eV)	14.8 (p _z)	34.17 (p _z)	15.91 (p _z)	1.64 (p_y+p_z)	6.17 (p _z)	27.32 (p _z)
HOMO-4 (-3.26eV)	7.38 (d _{z²})	78.73 (p _z)	10.3 (p _x)	1.38 (p _y)	0.23 (p _z)	1.98 (p _z)
HOMO-3 (-3.08eV)	0.19	1.84 (p _z)	80.86 (p _x)	10.11 (p _y)	0.09 (p _z)	6.92 (p _x)
HOMO-2 (-2.18eV)	95.73 (d _{z²})	1.20 (p _z)	2.94 (p _x)	0.01 (p _z)	0.10 (p _z)	0.02 (p _z)
HOMO-1 (-2.01eV)	90.81 (d _{x²-y²})	5.4 (p _z)	0.22 (p _z)	0.03 (p _z)	3.07 (p _z)	0.47 (p _z)
HOMO (-1.79eV)	85.09 (d _{xz} , d _{yz})	6.78 (p _z)	0.28 (p _z)	0.01 (p _z)	6.86 (p _z)	1.00 (p _z)
LUMO (+0.12eV)	34.23 (d _{xz} , d _{yz})	23.93 (p _z)	2.71 (p _z)	0.79 (p _z)	32.05 (p _z)	6.29 (p _z)
LUMO+1 (+0.85eV)	1.50 (d _{xz} , d _{yz})	4.25 (p _y)	21.10 (p _z)	4.65 (p _z)	39.86 (p _z)	30.00 (p _z)
LUMO+2 (+1.31eV)	6.46	3.79 (p _z)	40.32 (p _z)	12.41 (p _z)	0.39 (p _z)	36.63 (p _z)
LUMO+3 (+1.49eV)	4.98 (d _{xz})	5.38 (p _z)	39.50 (p _z)	12.28 (p _z)	9.68 (p _z)	28.18 (p _z)
LUMO+4 (+1.91eV)	0.98 (d _{yz})	3.66 (p _y)	27.79 (p _z)	8.78 (p _z)	52.20 (p _z)	9.76 (p _z)

5.5.3 Electronic Coupling between PtTPP Molecules and Graphene

The spectroscopy measurements of PtTPP(CO₂Me)₄ molecules were made on both graphene/ SiC (0001) and graphene/ SiC (000-1). When the tip-sample separation is large (V<-3.5V), only the occupied states can be detected. This is correlated to the different molecular orbital DOS extensions. For the occupied states, the d orbitals of

Pt dominate the molecular DOS, especially HOMO-2 at -2.18eV, 95% DOS comes from the Pt d_{z^2} orbital. While for the unoccupied states, the DOS comes predominantly from the p_z orbitals of the C and N atoms, whose DOS extension to the vacuum is less than that of Pt d orbital. Even though 34% DOS of LUMO comes from the Pt d_{xz} , d_{yz} orbitals, the LUMO orbital is hard to be detected because the energy level is close to Fermi level (+0.12V). i.e. conductance of graphene is small close to the Fermi level.

When the same set-point bias voltage (-3.7V) and tunneling current (0.1nA) are applied (same tip-sample separation) to the graphene/ SiC (000-1) and to graphene/ SiC (0001) substrates, the same molecular occupied state peak shifts from -3.27eV to -2.58eV. For graphene on Si-terminated SiC, the Dirac point is at 0.42eV below the Fermi level. For graphene on C-terminated SiC, the electronic properties are similar to the freestanding monolayer graphene. In our experiment, the deposition condition (248 °C for 60s) produced bilayer PtTPP(CO_2Me)₄ molecules on graphene/SiC (0001), while only a single molecular layer was grown on graphene/ SiC (000-1) at a deposition temperature of 240°C for 40s. It was suggested the charge transfer from a thick multilayer Pt-Porphyrin (PtP) molecules (~100) on graphene possible be in either directions (from graphene to molecular layer or from molecular layer to graphene) regarding on the polarity of the gate voltage[4]. Specifically, for the negatively charged graphene, the charge transfer direction is from graphene to PtP molecules, on the contrary, for the positively charged graphene, the charge transfer direction is the opposite. If this hypothesis is correct, here, in the STM, the doping of the graphene might determine the charge transfer direction. Because the graphene grown on SiC (0001) is n-doped, the charge transfer direction might be from graphene to the molecular layer, while for the neutral graphene on SiC (000-1), the charge transfer between graphene and molecular layer is likely weak.

To understand the electronic coupling between PtTPP(CO₂Me)₄ molecules and graphene, the charge transfer between a single molecule and freestanding monolayer graphene has been determined by DFT calculation. The calculated charge transfer direction is from graphene to PtTPP(CO₂Me)₄ molecule in the equilibrium state and each molecule receives 0.15e⁻ from graphene.

Previous studies corroborate that the charge transfer only occurs at the interface between TCNQ molecules and graphene. For several TCNQ molecular layers, no charge transfer occurs in the bulk film[16, 17]. The charge transfer between PtTPP(CO₂Me)₄ molecules and graphene might also only happen at the molecule/graphene interface. To better understand the charge transfer between double layer molecules on graphene, the single molecule on molecular network/graphene was calculated, as seen in Figure 5.12. The most stable adsorption site of single PtTPP(CO₂Me)₄ molecule on four self-assembled molecular network is on top, with an adsorption energy of -1.1eV. The charge transfer from molecular network to the single molecule on top is 0.034e⁻. It confirms the charge transfer mainly happens at the PtTPP molecule/ graphene interface.

For bilayer molecules/ graphene/ SiC (0001), even though the n-doped graphene is more favorable for the charge transfer from graphene to the molecules, the top molecular layer might remain neutral. For single molecular layer on graphene/ SiC (000-1), each molecule receives 0.15e from the quasi free-standing graphene, the collective effect of charge transfer in the molecular layer is very likely to shift the occupied molecular orbital to the lower energy by 0.69eV. The experimental data of single layer molecular electronic properties on graphene/ SiC (0001) is necessary to better understand the charge transfer between PtTPP molecules and graphene.

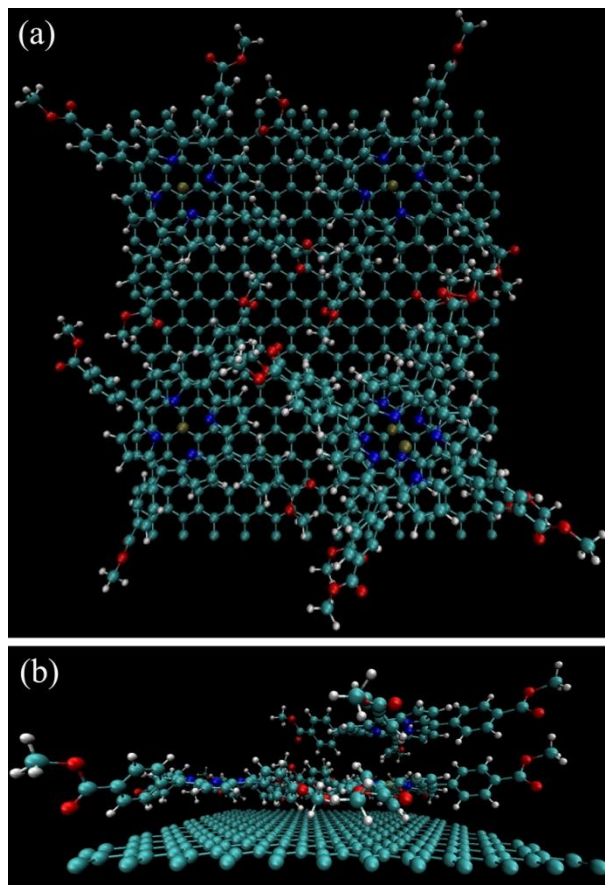


Figure 5.12 DFT calculation for the single PtTPP(CO₂Me)₄ molecule on the self-assembled molecular network/ free standing monolayer graphene. No graphene doping is considered.

When a lower set-point bias voltage is applied ($V=-2.5V$), both occupied and unoccupied resonance peaks can be detected in the spectroscopy measurement (see Figure 5.8(a)). When the sample is negatively charged, the resonance peak at -2.04eV is assigned to the HOMO according to the calculated molecular DOS. For the resonance peak at +2.02eV, there are two hypotheses: first, the peak arises from the higher unoccupied molecular orbital than LUMO (LUMO+2 or LUMO+3). Because the calculated LUMO peak is pinned at Fermi level, it is not visible in the spectroscopy curve. In addition, the DFT calculated HOMO-LUMO gap is generally narrower than the real gap, because DFT only determines the fundamental state of the system and does not calculate the excited states. This results in a systematic underestimation of the gap, and a lack of accuracy in the determination of the

LUMO level position. The second hypothesis is that when the sample is positively charged, the electron conductance path is from tip Fermi level to the surface through the molecular unoccupied states. The electric field might pin the molecular HOMO orbital to the Fermi level of the surface, then the LUMO will shift to +1.9eV, which is correlated to the unoccupied peak position of +2.02eV. Whereas, more studies of the electric field effects on the molecular orbital energy levels should be done to confirm the hypothesis above.

5.6 Conclusions

The topography and electronic properties of PtTPP(CO_2Me)₄ molecules were studied on both graphene/SiC (0001) and graphene/SiC (000-1). The results are summarized below:

1. PtTPP(CO_2Me)₄ molecules in both single and double molecular networks form a self-assembled square lattice on both graphene/ SiC (0001) and graphene/ SiC (000-1). The lattice directions are dominated by the molecular symmetry, graphene terrace directions and the graphene symmetry. In addition, the bilayer PtTPP(CO_2Me) molecules on graphene show a triclinic phase (offset-face to face stacking).
2. The thermal treatment induces the deformation of the molecular configurations in the self-assembled molecular network, indicating a weak molecule-molecules interactions.
3. PtTPP(CO_2Me)₄ molecules are adsorbed on both graphene/SiC (0001) and graphene/ SiC (000-1) via the electrostatic interactions. The charge transfer direction is from graphene to PtTPP molecules.
4. For bilayer PtTPP(CO_2Me)₄ on graphene, the charge transfer only occurs at the molecule/ graphene interface.
5. The charge transfer from free-standing monolayer graphene to PtTPP(CO_2Me)₄ molecule (0.15eV) is stronger than that from NiPc

molecules to AA-stacked bilayer graphene (0.0375eV), indicating the stronger electronic coupling between PtTPP molecules and graphene than that between NiPc molecules and graphene.

5.7 Bibliography

- [1] A. C. Hazell. Structure of (5,10,15,20-tetraphenyl-21H,23H-porphinato)platinum(II), C₄₄H₂₈N₄Pt. *Acta Cryst.*, 40: 751-753 (1984).
- [2] J. Brede, M. Linares, *et al.* Dynamics of molecular self-ordering in tetraphenyl porphyrin monolayers on metallic substrates. *Nanotechnology*, 20: 275602 (2009).
- [3] P. Chen, O. S. Finikova, *et al.* Electrochemistry of Platinum(II) porphyrins: effect of substituents and π -extension on redox potentials and site of electron transfer. *Inorg. Chem.*, 51: 6200-6210 (2012).
- [4] C. Li, K. Komatsu, *et al.* Signature of gate-tunable magnetism in graphene grafted with Pt-porphyrins. *Phys. Rev. B*, 93: 045403 (2016).
- [5] M. P. Bym, C. J. Curtis, *et al.* Porphyrin sponges conservation of host structure in over 200 porphyrin-based lattice clathrates. *J. Am. Chem. Soc.*, 115: 9480-9491 (1993).
- [6] T. Djuric, T. Ules, *et al.* Substrate selected polymorphism of epitaxially aligned tetraphenyl-porphyrin thin films. *Phys. Chem. Chem. Phys.*, 14: 262-272 (2012).
- [7] C. Pistonesi, E. Pronzato and A. Juan. A DFT study of H adsorption on Pt(111) and Pt-Ru(111) surfaces. *Appl. Surf. Sci.*, 254: 5827-5830 (2008).
- [8] E. Bakkers, Z. Hens, *et al.* A tunnelling spectroscopy study on the single-particle energy levels and electron-electron interactions in CdSe quantum dots. *Nature Nanotech.*, 13: 258-262 (2002).

- [9] J. A. Stroscio, R. M. Fccnstra andA. P. Fein. Electronic structure of the Si(111)2 x 1 surface by Scanning-Tunneling Microscopy. Phys. Rev. B., 57: 2579-2583 (1986).
- [10] T. Houwaart, T. L. Bahers, *et al.* Scrutinizing individual CoTPP molecule adsorbed on coinage metal surfaces from the interplay of STM experiment and theory. Surf. Sci., 635: 108-114 (2015).
- [11] P. Sautet and C. Joachim. Interpretation of STM images: copper-phthalocyanine on copper. Surf. Sci., 271: 387-394 (1992).
- [12] P. Sautet and M. L. Bocquet. Shape of molecular adsorbates in STM images: A theoretical study of benzene on Pt (111).... Phys. Rev. B., 53: 4910 (1996).
- [13] P. Sautet and C. Joachim. Calculation of the benzene on rhodium STM images. Chem. Phys. Lett., 185: 23-30 (1991).
- [14] T. Yokoyama, S. Yokoyama, *et al.* Nonplanar adsorption and orientational ordering of porphyrin molecules on Au(111). J. Chem. Phys., 115: 3814 (2001).
- [15] W. Auwarter, A. W. Bargioni, *et al.* Controlled metalation of self-assembled porphyrin nanoarrays in two dimensions. Chem. Phys. Chem., 8: 250-254 (2007).
- [16] W. Chen, S. Chen, *et al.* Surface transfer p-type doping of epitaxial graphene. J. Am. Chem. Soc., 129: 10418-10422 (2007).
- [17] C. Coletti, C. Riedl, *et al.* Charge neutrality and band-gap tuning of epitaxial graphene on SiC by molecular doping. Phys. Rev. B., 81: 235401 (2010).

Chapter 6

Electronic Properties of Fe -Tetraphenylporphyrin Molecules on Graphene

Table of Contents

6.1 Introduction.....	140
6.2 Experimental Procedure.....	140
6.3 Self-Assembled FeTPP Molecules on Graphene/ SiC (0001).....	142
6.3.1 Single-Layer FeTPP Molecular Network.....	142
6.3.2 Molecular Adsorbates on top of the Well-Ordered Molecular Network.....	144
6.4 Double-Layer FeTPP Molecular Network on Graphene/ SiC (0001).....	148
6.5 Self-Assembled FeTPP Molecules on Graphene/ SiC (000-1).....	155
6.6 STS of FeTPP Molecules on both Graphene/ SiC (0001) and Graphene/ SiC (000-1).....	158
6.7 Conclusions.....	167
6.8 Bibliography.....	168

6.1 Introduction

In the proposed spin-field effect transistor based on graphene, the ideal electron conduction path between the source and drain is the dielectric layer/ graphene interface which carries spin information and operates in a ballistic electron transport regime. In previous experiments, the NiPc and PtTPP molecules, whose neutral states do not carry spin information, were used to functionalize graphene to induce the magnetic properties. Introducing a magnetic moment by using the metal-TPP molecules which carry magnetic moments via weak coupling with graphene, such as FeTPP or MnTPP molecules might be a more immediate solution.

In this experiment, the five-coordinated Fe(III)(TPP)Cl molecules were used. There are three possible spin states for Fe(TPP)Cl molecules: low spin ($S=1/2$), intermediate spin ($S=3/2$) and high spin ($S=5/2$). The previous studies proved that the five coordinate Fe(TPP)Cl are very likely to be in the high spin state [1-3]. Here, the topography and electronic properties of Fe(TPP)Cl molecules on graphene were studied.

6.2 Experimental Procedure

In this study, the meso-substituted Fe(TPP)Cl molecules were purchased from SIGMA-ALDRICH. The molecular structure and the sample of molecular powder in dark purple color are shown in Figure 6.1. For the high-spin Fe(TPP)Cl molecular geometry, the DFT calculated Fe-Cl and Fe-N bond lengths are 2.19 Å and 2.05 Å, respectively. The iron atom is displaced out-of-plane from the nitrogen atoms by 0.38Å[4].

In this experiment, the graphene terraces on both Si-terminated 6H-SiC and C-terminated 6H-SiC substrates were prepared following the procedures described in Chapter 3. On the C-terminated SiC substrate, multilayer graphene was grown with an azimuthal disorder. The topography and electronic properties of multilayer graphene

were discussed in Chapter 3. Before deposition, Fe(TPP)Cl molecules were cleaned by several cycles of degassing at 180 °C. Then, the molecular powder in the Quad Dopant Source was deposited on graphene by resistive heating at 195 °C for 30s.

On the Si-terminated SiC substrate, a majority of monolayer graphene with a small percentage of bilayer graphene were obtained. After degassing, the Fe(TPP)Cl molecules were deposited on graphene at 195 °C for 30s. This produced at least a bilayer of FeTPP molecules. This will be discussed in section 6.4. To obtain single molecular layer, the sample was flashed at a maximum temperature of 1100°C and the molecules were redeposited at 195°C for 15s to form the molecular network with lower coverage. After each deposition, the sample was post-annealed at 120°C ~150°C for several hours to stabilize the adsorbed molecules. The surface topography was imaged by STM and the electronic properties were probed by STS.



Figure 6.1 The Fe(TPP)Cl molecular structure and the molecular sample in dark purple color used in the experiment.

6.3 Self-Assembled FeTPP Molecules on Graphene/ SiC (0001)

6.3.1 Single-Layer FeTPP Molecular Network

After the deposition of Fe(TPP)Cl molecules at 195 °C for 15s, a single molecular layer with some molecular adsorbates on top of the molecular network was obtained. The 35nm×35nm STM image in Figure 6.2 (a) shows that the molecules form a close-packed near square lattice, where the average molecular lattice parameters are 1.42nm ($\pm 0.06\text{nm}$) \times 1.37nm ($\pm 0.02\text{nm}$) with an angle of 93 ° ($\pm 4 \text{ }^\circ$). When we focus on the molecules in the molecular network, two types of molecules can be observed; most of the molecules show a low DOS, while a small fraction of molecules display a higher DOS. The line profile in Panel (b) indicates that the measured height difference between the two-type-molecules is 2.99 Å ($\pm 0.34\text{\AA}$). A previous study found that the Fe-Cl bond length in the Fe(TPP)Cl molecule is 2.19 Å, in addition, the Fe iron atom is displaced out-of-plane from the nitrogen atoms by 0.38 Å[4], hence, the Cl atom should be above the porphyrin plane by 2.57 Å. The measured molecular height difference is very close to the distance between the Cl atom and porphyrin plane (deviation: 16.34%), which implies that the bright molecules in the molecular network are Fe(TPP)Cl molecules, while the others are FeTPP molecules. The thermogravimetric analysis revealed that the Fe(TPP)Cl is thermally stable up approximately 400°C[5]. In addition, a molecular network with a majority of FeTPP and a minority of Fe(TPP)Cl molecules in the molecular network was reported after the deposition of Fe(TPP)Cl molecular powder on the Au(111) substrate at 400 °C[6]. In contrast, the annealing of Mn(TPP)Cl molecules at 237 °C leads to a complete removal of the Cl ligand[7]. At the Fe(TPP)Cl molecular deposition temperature of 195 °C in our experiment, the molecules in the molecular network should still contain the chlorine. To distinguish the type of molecule in the molecular network, a zoom of the molecular network with the low DOS for each molecule was studied, as

shown in Figure 6.2 (c). The molecules in the occupied states image at -1.5eV show a typical saddle-like conformation of MTPP molecules, the depression in the molecular center indicates that they are FeTPP molecules. Due to the Fe-Cl bond, the Fe(TPP)Cl molecular topography should have a prominent center regardless of the applied bias voltages.

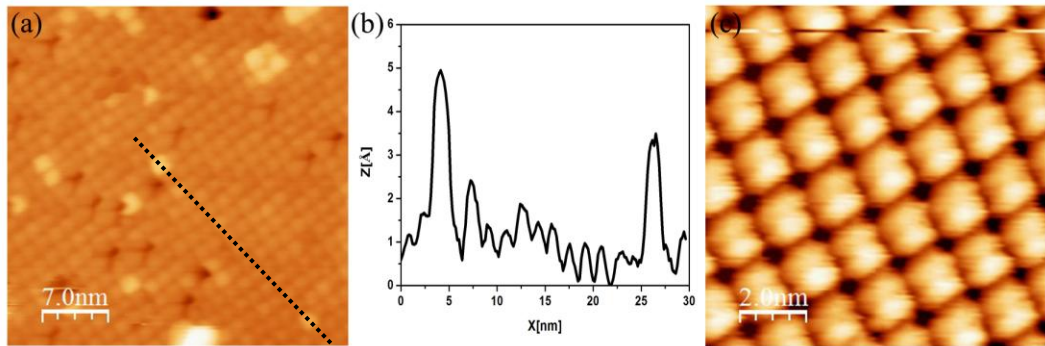


Figure 6.2 (a) 35nm × 35nm STM image of well-ordered single FeTPP molecular layer on graphene/SiC(0001), Tunneling condition: V=-1.5V, I=0.15nA; (b) The profile along the black dotted line in Panel (a) indicates the height difference between two types of molecules is 2.99Å ($\pm 0.34\text{\AA}$); (c) The 10nm × 10nm STM image of the single layer molecules with intramolecular contrast, tunneling condition: V=-1.5V, I=0.15nA.

Figure 6.3 shows the boundary of a well-ordered FeTPP molecular network. In the 50nm × 50nm STM image at a bias voltage of -2.0V in Panel (a), the left part is the well-ordered molecules with some molecular adsorbates on top of the molecular network. The right part shows a clean flat terrace without molecules. When the flat terrace is zoomed (15nm × 15nm), the honeycomb lattice is displayed indistinctly (see Panel (b)). The FFT pattern for the zoomed image confirms its honeycomb lattice with a period of 1.81 nm ($\pm 0.15\text{nm}$). It is the feature of the buffer layer with the (6×6) lattice and a period of 1.9nm, which indicates the flat terrace is graphene, because at high bias voltage, the electrons tunnel directly into the buffer layer underneath the graphene (see the discussion in Chapter 3). From several STM images, the average

distance between the molecular layer and graphene is 3.20\AA , which confirms the single molecular layer in the left part. Among the experiments performed on NiPc, PtTPP and FeTPP molecules, this is the first time that the molecular layer and graphene edge can be observed directly from the STM images. This implies that the electronic coupling between FeTPP molecules and graphene is stronger than that between NiPc or PtTPP molecules and graphene. Whereas, the horizontal lines at the boundary of molecules and graphene imply the molecular diffusion during scanning, which suggests the non-covalent bonding between FeTPP molecules and graphene.

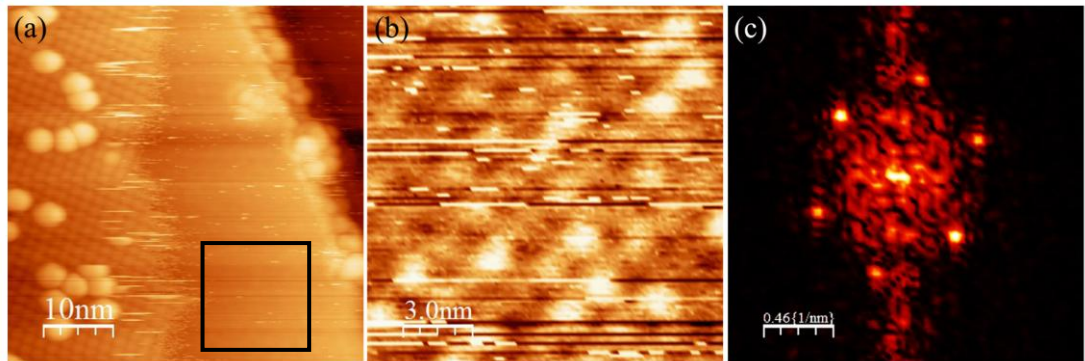


Figure 6.3 (a) The $50\text{nm}\times 50\text{nm}$ STM image of single molecular layer on graphene, tunneling condition: $V=-2.0\text{V}$, $I=0.15\text{nA}$; (b) The zoomed $15\text{nm}\times 15\text{nm}$ STM image of the right part in the rectangular region; (c) The FFT pattern for the zoomed STM image in panel (b).

6.3.2 Molecular Adsorbates on top of the Well-Ordered Molecular Network

Several square-like adsorbates on top of the single-layer molecular network are observed in Figure 6.3 (a). When the same area was scanned several times, the diffusion of the adsorbates could be clearly observed. With a scanning speed of 150nm/s , it takes about $2\text{min}20\text{s}$ to finish scanning a $50\text{nm}\times 50\text{nm}$ image. To understand better the diffusion, a series of zoomed $22\text{nm}\times 45\text{nm}$ STM images at the same area of the molecular adsorbates on top of the molecular network at the same

area are shown in Figure 6.4. In Panel (a), seventeen adsorbates are randomly positioned on top of the molecular network. From Panel (a) to Panel (b) (The interval between the two scan start time is 5min), two adsorbates in the red dash circle have disappeared, while an adsorbate in the green circle appears. From Panel (b) to Panel (c) (The interval between the two scan start time is 9 min), the two adsorbates in the red dash circles have diffused to the green circles in upper area. From Panel (c) to Panel (d) (The interval between two scan start times is 5min), the previous adsorbates are intact, while several new adsorbates appear in the green circles.

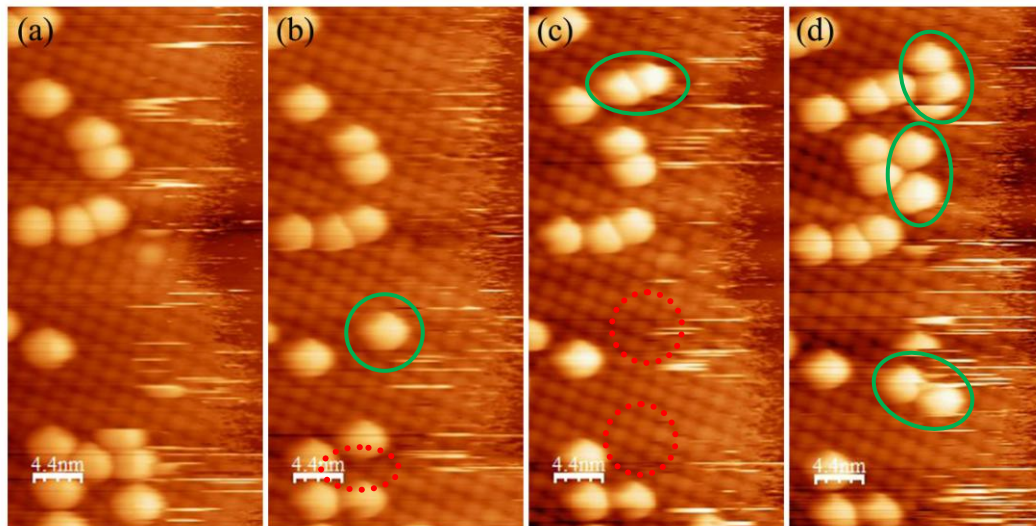


Figure 6.4 Zoomed $22\text{nm} \times 45\text{nm}$ STM image of the single molecular layer with adsorbed molecules. (a) Tunneling condition: $V=-2.0\text{V}$, $I=0.15\text{nA}$; (b) After 5min, Tunneling condition: $V=-1.8\text{V}$, $I=0.15\text{nA}$; (c) After 9min, Tunneling condition: $V=-1.8\text{V}$, $I=0.15\text{nA}$; (d) After 5min, Tunneling condition: $V=-1.8\text{V}$, $I=0.15\text{nA}$.

There are two possibilities for the evolution of the adsorbates on top of the molecular network: one is the result of the manipulation by STM tip, the other one is the diffusion of the adsorbates. During scanning, the high bias voltages (-2.0V and -1.8V) and small tunneling current (0.15nA) were used, the tip is quite far away (1~2 nm), so that make the attachment of the adsorbates to the apex might be reduced. If we

consider the possibility that one of the adsorbates was attached at the apex of the tip, only the contours of the adsorbates would be visible in the STM image before the attached adsorbates become detached, because of the larger size of the adsorbates than the single molecules in the molecular network. Whereas, every molecule in the molecular network can be seen in both Panel (b) and (c). Therefore, the possibility of the manipulation by STM tip can be ruled out. The adsorbates evolution from Panel (a) to (d) is the result of molecular diffusion at room temperature, which indicates the weak out-of-plane molecule-molecule interaction. The adsorbed molecules do not have the preferential adsorption sites on top of the molecular network, but for some timeframe, the molecules have a temporary fixed position on surface.

To better study the properties of the molecular adsorbates on top of the single layer FeTPP molecular network, the adsorption sites and directions were analyzed statistically. The typical molecular adsorbates STM images are shown in Figure 6.5. The profile along the black dotted line in Panel (a) indicates the square-like adsorbates height on top of the molecular network is 5.0\AA ($\pm 0.3\text{\AA}$), with a half-height width of 2.82nm ($\pm 0.07\text{nm}$). From this, the best description is that the adsorbates form an aggregate of four molecules in a (2×2) square. The reason is that the maximum size of the single FeTPP molecule in the diagonal direction is about 1.5nm if the phenyl groups are in the same plane as the porphyrin plane, while the dihedral angle between phenyl groups and porphyrin plane results in a smaller molecular size. The half-height width of the adsorbed molecules is about double that of the single FeTPP molecular size. Compared with the molecular lattice constants in the well-ordered molecular layer, the measured square-like four-molecular aggregate area is about 86% of the former one, indicating a stronger in-plane intermolecular interaction. The molecular aggregation between metal porphyrin is often observed in solution[8]. In our experiment, the four-molecule aggregate is the only adsorbate type we observed on top of the single molecular network. The diffusion of the four-molecular aggregates on top of the molecular network implies

that the in-plane molecule-molecule interaction is stronger than the out-of-plane molecular interaction. In addition, in the derivative STM image in Panel (c), it is interesting to see that all the adsorbed molecular aggregates show the same orientation, the average rotation angle with respect to the molecular lattice is 45° ($\pm 3^\circ$) in the anti-clockwise direction. It is different from the molecular orientation in the well-ordered molecular network, which is rotated 14° ($\pm 2^\circ$) compared to the molecular lattice in the clockwise direction. For the adsorption sites of the molecular aggregates, they are not fixed. From the STM image in Figure 6.4, some adsorbed molecular centers are in the space between the underlying molecules, some are on top of the underlying molecules. In the STM image in Figure 6.5, a majority of the adsorbed molecular centers are in the space between the adjacent molecules, while a minority are on top of the molecules in the well-ordered molecular network.

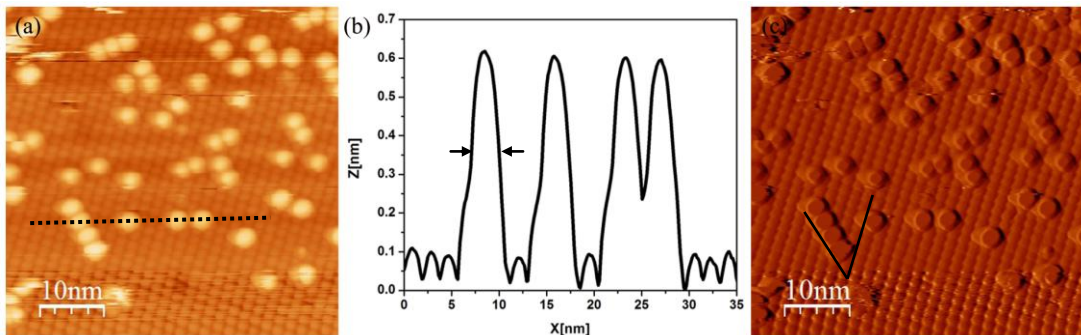


Figure 6.5 (a) $50\text{nm} \times 50\text{nm}$ STM image of the adsorbed molecules on top of the single-layer molecular network, tunneling condition: $V=-2.5\text{V}$, $I=0.15\text{nA}$; (b) The profile along the black dotted line in Panel (a), the adsorbed molecular height is 5.0\AA ($\pm 0.3\text{\AA}$). The half-height width is 2.82nm ($\pm 0.07\text{nm}$); (c) The derivative of the STM image in Panel (a).

Generally, physisorbed species do not experience strongly directional interactions. They are more tenuously bound to specific sites and experience an attraction interaction with the surface that is uniform across the surface. But in this case, the adsorbed molecules show a specific direction, with no specific adsorption sites.

6.4 Double-Layer FeTPP Molecular Network on Graphene/ SiC (0001)

After the deposition of Fe(TPP)Cl molecules on graphene at 195°C for 30s, a double-layer molecular network on graphene was obtained. Figure 6.6 (a) shows a 50nm×40nm STM image of both the bottom and top molecular layers on graphene. Because of the dissociation of Cl atoms during the molecular deposition, the molecules in the molecular network might be FeTPP molecules. From the line profile shown in Panel (b), the measured distance between the bottom (black arrow) and top molecular layer (red arrow) is 6.13Å ($\pm 0.80\text{\AA}$). This is a little larger than the distance between PtTPP molecular layers. The higher interlayer spacing might be caused by the larger dihedral angle of phenyl groups compared to the porphyrin backbone in FeTPP molecule.

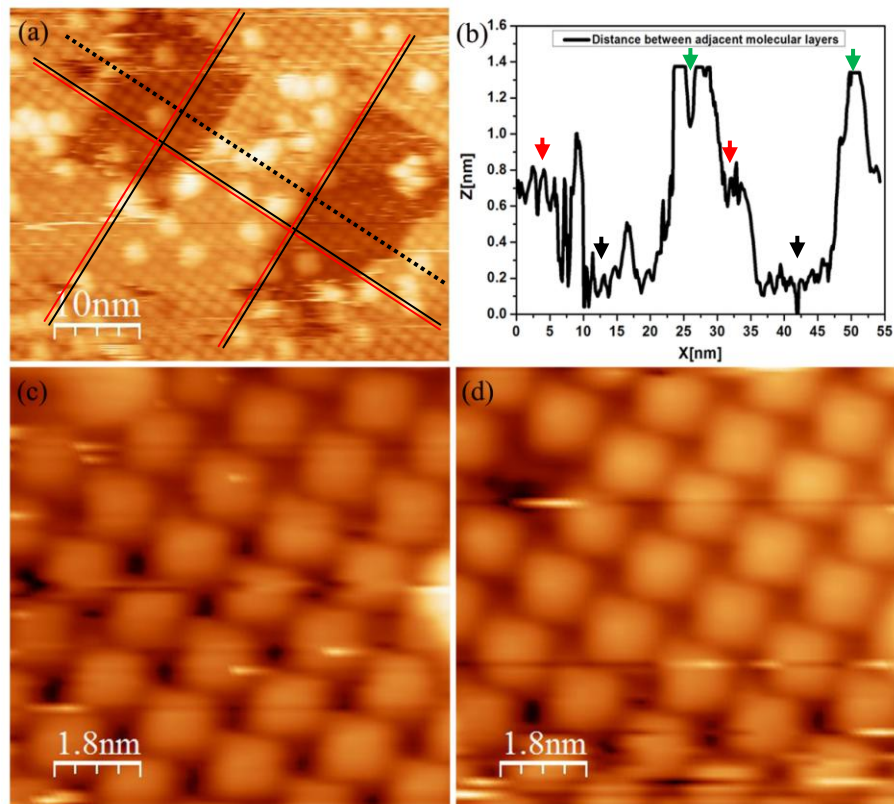


Figure 6.6 Double-layer FeTPP molecular network on graphene/ SiC (0001). (a) 50nm×40nm STM image of double-layer molecular network on graphene/ SiC (0001), tunneling condition: V=-3.5V, I=0.15nA; (b) The distance between adjacent molecular layers is 6.13Å ($\pm 0.80\text{\AA}$), the height of the adsorbed molecules on well-ordered molecular network is 6.09Å ($\pm 0.87\text{\AA}$). The black, red and green arrows indicate the height of the single, double molecular layer and adsorbed molecules, respectively; (c) Zoomed 9nm×9nm STM image of the bottom molecular layer in the left part; (d) Zoomed 9nm×9nm STM image of the top molecular layer.

From the STM image in Panel (a), it can be seen that molecules in both bottom and top layers form a square lattice network with the same molecular lattice directions. The measured average lattice parameters for the top molecular layer are 1.42nm ($\pm 0.08\text{nm}$) × 1.31nm ($\pm 0.05\text{nm}$) with an angle of 92 ° (± 2 °), similar to the molecular lattice of the bottom molecular layer (1.42nm×1.37nm with an angle of 93 °). When the bottom molecular layer in the left part is zoomed (see Panel (c)), it can be seen that the angle between molecular orientation and molecular lattice direction is about

20° ($\pm 5^\circ$). From the zoomed top molecular layer in Panel (d), the angle between molecular orientation and lattice in the top molecular layer is 23 ($\pm 4^\circ$). This indicates the FeTPP molecules in both bottom and top layer show the same orientation and at the same time, they form the same molecular lattice direction. When we focus on the edges of the molecular layers, the molecular positions in the bottom molecular layer (black solid lines) and top molecular layers (red solid lines) have a small offset in both molecular array directions: 6.6 Å (± 1.1 Å) (vertical line) and 5.5 Å (± 1.1 Å) (horizontal line), respectively.

Because of the delocalized π states of aromatic molecules, the molecular stacking is generally via the electrostatic π - π interactions. The molecular stacking modes are described as face to face, offset-face to face, and edge to face. Among these, the π - π repulsion dominates in the face-to-face π stacked geometry, while in offset-face to face stacking, the intermolecular interaction is dominated by the π - σ [9]. In the crystal structure of kekulene[10] and (18) annulene, the π systems are parallel, stacked, and offset so that the π system of one molecule lies over the π -cavity at the center of its nearest neighbour, while in the other direction, the molecules are aligned to give perpendicular, edge-on interactions with their neighbours[11]. The stacked zinc porphyrin-zinc porphyrin geometry in solution has a shift in both X and Y directions with an interplanar separation of 3.4 Å. The pyrrole group of one molecule is directly above the π -cavity at the center of the other. Such an arrangement minimizes π - π repulsion, while at the same time, maximizes the attraction between the σ -framework around the inner edge of the π -cavity of one porphyrin with the π electrons of the pyrrole ring immediately above[8]. The molecular position offsets in both directions are in accordance with the FeTPP molecular layer stacking mode in our experiment. However, the separation between the FeTPP molecular layers is 6.13 Å, which is larger than the reported π - π stacking interaction (3.3 Å-3.8 Å)[7, 12]. This might arise from the opposite tilting directions of the phenyl rings in FeTPP molecules in the adjacent molecular layers or the

repulsion force between H atoms in the adjacent phenyl rings. As a whole, the double FeTPP molecular layers can be deduced as the offset face-to-face stacking via the weak Van der Waals force, the stacking model of the double FeTPP molecular layers is shown in Figure 6.7.

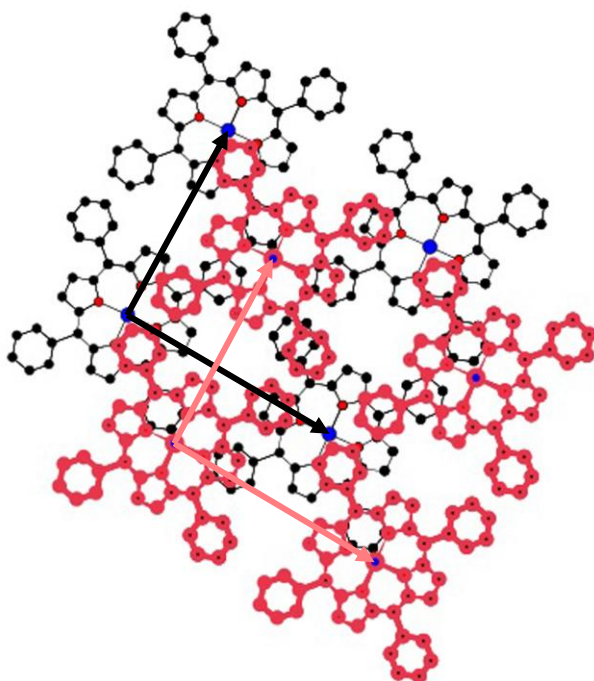


Figure 6.7 The offset-face to face stacking model of the double FeTPP molecular layers/ graphene/ SiC (0001). The molecular orientation is rotated 18° with respect to the molecular lattice. The molecules in pink are in the top layer, the molecules in black are in the bottom layer. The tilting and bending of the pyrrole rings and phenyl groups are not considered. The H atoms are excluded for clarity.

Figure 6.8 shows a $50\text{nm} \times 50\text{nm}$ STM image of the single molecular layer with some adsorbates, in which the molecules in the well-ordered molecular network with a intramolecular contrast can be clearly seen, especially in the derivative image in Panel (c). Similar to the molecules in the single-layer molecular network, two types of molecules in the double molecular network also can be seen. Most of the molecules shows a depression in the center, which can be ascribed to the FeTPP

molecules. Several molecules (in the black circles) show a higher DOS. The profile along the red line in Panel (b) shows the bright molecules is higher than the normal molecules by 2.3\AA ($\pm 0.5\text{\AA}$) (see Panel (b)), indicating the presence of the Fe-Cl bond. The height difference between the two molecular topographies clearly suggests that the majority of Fe(TPP)Cl molecules are transformed to FeTPP molecules during the evaporation. The minority Fe(TPP)Cl molecules are randomly mixed in the well-ordered FeTPP molecular network.

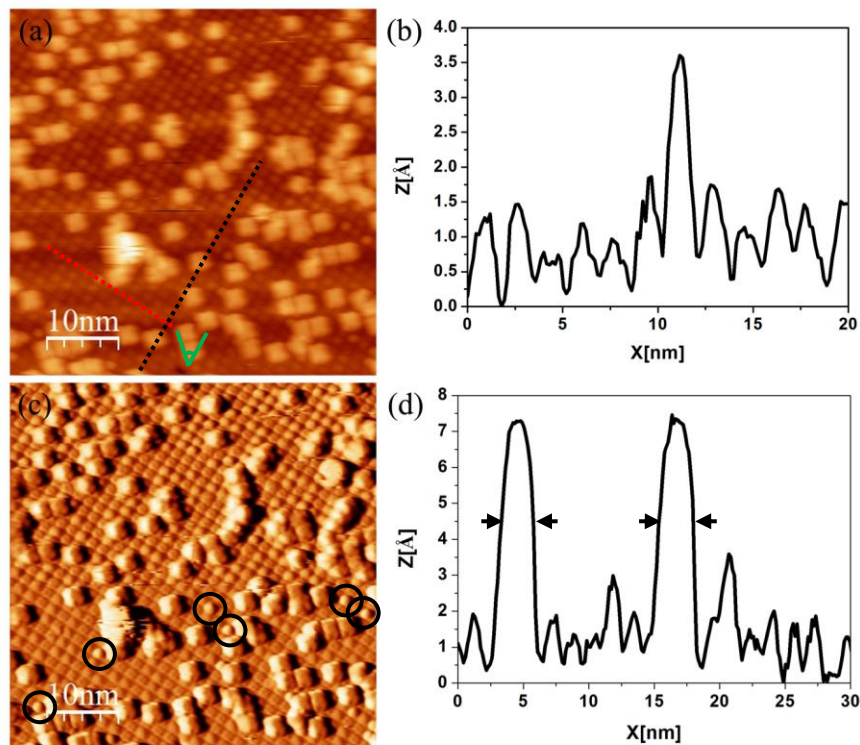


Figure 6.8 (a) The ($50\text{nm} \times 50\text{nm}$) STM image of double-layer FeTPP molecules with the adsorbed molecules on the top of molecular network. The tunneling condition: $V=-3.5\text{V}$, $I=0.15\text{nA}$; (b) The line profile along the red line in Panel (a), the Fe(TPP)Cl molecular is higher 2.3\AA ($\pm 0.5\text{\AA}$); (c) The derivate of the STM image in Panel (a); (d) The line profile along the black line in Panel (a). The adsorbed molecular height on top of the molecular network is 5.7\AA , the half-height width is 2.48nm ($\pm 0.23\text{nm}$).

In Figure 6.6, several adsorbed molecules on top of the molecular network can be seen in the STM image. In the line profile in Panel (b), the green arrows and red arrows indicate that the adsorbed molecular height is 6.1 \AA ($\pm 0.9\text{ \AA}$). It is very similar to the interplanar separation between the molecular layers (6.1 \AA). In addition, the adsorbed molecules on top of both the single and double molecular network show a similar orientation compared to the molecular lattice direction. In Figure 6.8, tens of molecules adsorbed on top of the molecular network are also observed. The line profile in Panel (d) indicates an adsorbed molecular height of 5.73 \AA , agreeing quite well with the measured height in Figure 6.6. The half-height width is 2.48 nm ($\pm 0.23\text{ nm}$), indicates the formation of four-molecular aggregates in (2×2) lattice on the molecular network, in the same way as the adsorbates on top of the single FeTPP molecular layer. For the topography of the adsorbed molecules, the majority of the adsorbed four-molecular aggregates appear domed with a high DOS in the center, from the derivative STM image shown in Panel (c). Though this might be an artifact induced by derivative procedure, it might be the result of the phenyl groups tilting in each molecules in the aggregate. For the adsorption sites of the four-molecular aggregates on the double layer molecular network, similar to that on the single FeTPP molecular layer, they are not fixed, either. The majority of the centers of the adsorbed molecules are on top of the molecules in the well-ordered molecular network, a minority are in the space between the molecules. Moreover, all the adsorbed four-molecular aggregates in Figure 6.8 are oriented in the same direction, the average angle of the adsorbed molecular aggregate direction with respect to the molecular lattice is 51° ($\pm 7^\circ$), as marked by the green angle in Figure 6.8 (a).

It was reported that for the neutral porphyrin-porphyrin stacking, no rotation of one porphyrin relative to the other was observed, the rotation always leads to a less favorable interaction energy[9]. Whereas, for the interactions between π systems polarized by heteroatoms, the presence of strongly polarizing atoms has a major influence on the electrostatic interaction. For the neutral π -system molecules, the

molecular position offset is favorable, whereas the molecular rotation is not. For the polarized molecules, the rotation of the molecules is favorable. In the crystal structure of the μ -O-(FeTCPP)₂ ·16DMF, two FeTCPP rings are bonded together by a bridging O atom in a Fe-O-Fe bond system. The macrocycle rings are parallel to each other, the relative orientations of the two porphyrin rings make an average N_p-Fe-Fe'-N_p dihedral angle of 33.6° with respect to the peripheral carboxylic groups[6]. The geometry of the nearest neighbor intermolecular interaction in the crystal structure of tetramethyl p-benzoquinone also shows a rotation between the stacked molecules[13]. In our experiment, the stacking mode of the FeTPP molecules in the top and bottom molecular layer is offset face to face without rotation. The rotation of the adsorbed molecular aggregates on top of the molecular lattice indicates the polarization of the adsorbed molecules. The polarization might come from the stronger intermolecular interactions in the molecular aggregates. The measured height of the four-molecular aggregates on top of the well-ordered molecular network (6.1 Å) is identical to the interplanar separation of the well-ordered FeTPP molecular layers (6.1 Å), therefore, the possibility of Fe(TPP)Cl molecular aggregates is ruled out. For the adsorbed molecular aggregates, the intermolecular interaction is stronger than the molecules in the well-ordered molecular network, and it is asymmetric in the sense that the inside and outside of each aggregate does not have the same environment; while for the molecules in the molecular network, the intermolecular interactions are homogeneous. It is the non-equivalent in-plane intermolecular interactions that causes the polarization and induces the rotations of the adsorbed molecules. The model of the four-molecular aggregates on top of the well-ordered FeTPP molecular network is shown in Figure 6.9, in which the molecular aggregate adsorption site is arbitrarily chosen. The molecular aggregate direction is rotated 50° with respect to the molecular lattice direction.

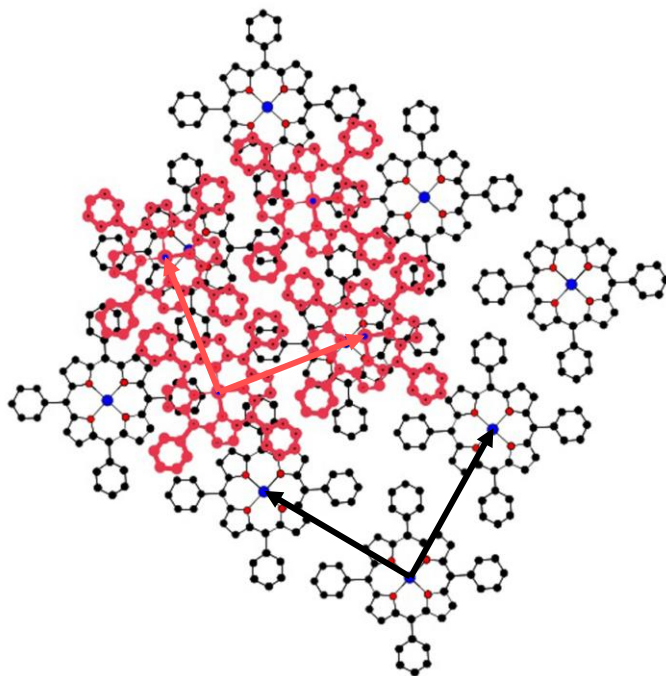


Figure 6.9 The model of the four-molecular aggregates on top of the well-ordered FeTPP molecular network. The molecular orientation is rotated 18° with respect to the molecular lattice. The distance between the adjacent molecules is about 86% of the molecular lattice constants. The molecular aggregation direction is rotated 50° with respect to the molecular lattice direction (The adsorption site is arbitrarily chosen).

6.5 Self-Assembled FeTPP Molecules on Graphene/ SiC (000-1)

After the deposition of Fe(TPP)Cl molecular powder at 195°C for 30s, a double molecular layer was obtained on the graphene/ SiC (000-1) substrate, as shown in Figure 6.10 (a). In the same way as for the double molecular layer on graphene/ SiC (0001), the FeTPP molecules on graphene/ SiC (000-1) also form a near-square lattice, with lattice constants of $1.45\text{nm} (\pm 0.07\text{nm}) \times 1.31\text{nm} (\pm 0.09\text{nm})$ and an angle of $93^\circ \pm 5^\circ$. Two types of molecular topographies in the double-layer molecular network are also observed: normal and bright molecules in the occupied states at -3.5eV

compared to the Fermi level. The measured height difference between the bright and normal molecules in the molecular network is 3.2\AA ($\pm 1.3\text{\AA}$) (see Panel (b)), similar to the normal molecules and bright molecules in both single and double molecular network on both graphene/ SiC (0001) and graphene/ SiC (000-1). After the deposition of Fe(TPP)Cl molecules, the percentage of the bright molecules in the molecular network is about 9.8%. When the sample was post-annealed at between 120°C and 150°C for 30min, the percentage of the bright molecules decreases to about 3.7%, when the sample was annealed a second time at the same temperature for 110min, the percentage decreased to 1.2%. The decreasing proportion of bright molecules confirms that the normal molecules in the molecular network are FeTPP, while, the others are Fe(TPP)Cl molecules. With the annealing, the Fe(TPP)Cl molecules are transformed to FeTPP, due to the dissociation of the Cl atoms.

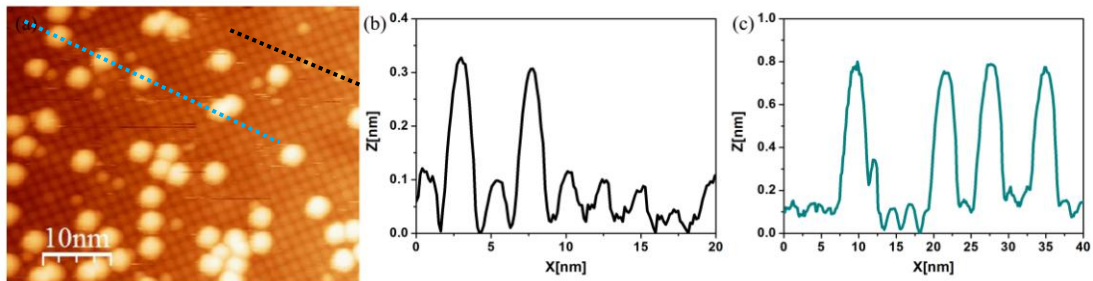


Figure 6.10 (a) A $50\text{nm} \times 50\text{nm}$ STM image of double Fe(TPP)Cl molecules on graphene/ SiC (000-1), Tunneling condition: $V=-3.5\text{V}$, $I=0.15\text{nA}$; (b) The height difference between the normal molecules and bright molecules in the molecular network, $3.2\text{\AA} \pm 1.3\text{\AA}$; (c) The adsorbed molecular height on top of the double Fe(TPP)Cl molecular layer, 5.9\AA ($\pm 0.2\text{\AA}$), the half-height width is 2.78nm ($\pm 0.08\text{nm}$).

Similar to the adsorbed molecules on top of the single and double molecular network on graphene/ SiC (0001), the majority of the adsorbed molecules on top of the double molecular network on graphene/ SiC (000-1) show a height of 5.9\AA ($\pm 0.2\text{\AA}$) with a half-height width of 2.78nm ($\pm 0.08\text{nm}$) (see Panel (c)), indicating that the adsorbed molecules are also the four-FeTPP molecule aggregates. The four-molecular aggregates also show form a preferential direction on top of the molecular network,

the angle difference between the four-molecule aggregate and molecular lattice in the molecular network is $48^\circ (\pm 2^\circ)$. In addition to the four-molecular aggregates on top of the molecular network on graphene/ SiC (000-1), tens of ‘smaller’ adsorbates are also observed, as shown in Figure 6.11. These are different from the adsorbed molecules on top of the molecular network on graphene/ SiC (0001). The line profile in Panel (b) indicates the height of the ‘smaller’ adsorbates on top of the double-layer molecular network is 6.2\AA ($\pm 0.4\text{\AA}$), with a half-height width of 1.61nm ($\pm 0.16\text{nm}$), which means the adsorbates are most likely isolated molecules instead of four-molecular aggregates.

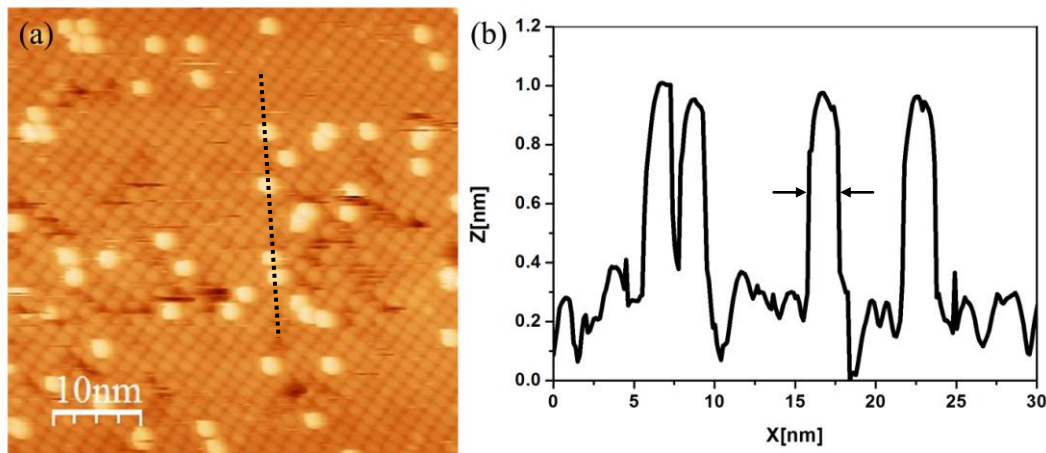


Figure 6.11 (a) ($50\text{nm} \times 50\text{nm}$) STM image of single molecular adsorbates on top of the double-layer molecular network; tunneling condition: $V=-2.5\text{V}$, $I=0.15\text{nA}$; (b) The height of the adsorbed single molecule on top of the double-layer molecular network is 6.2\AA ($\pm 0.4\text{\AA}$) with a half-height width of 1.61nm ($\pm 0.16\text{nm}$).

6.6 STS of FeTPP Molecules on both Graphene/ SiC (0001) and Graphene/ SiC (000-1)

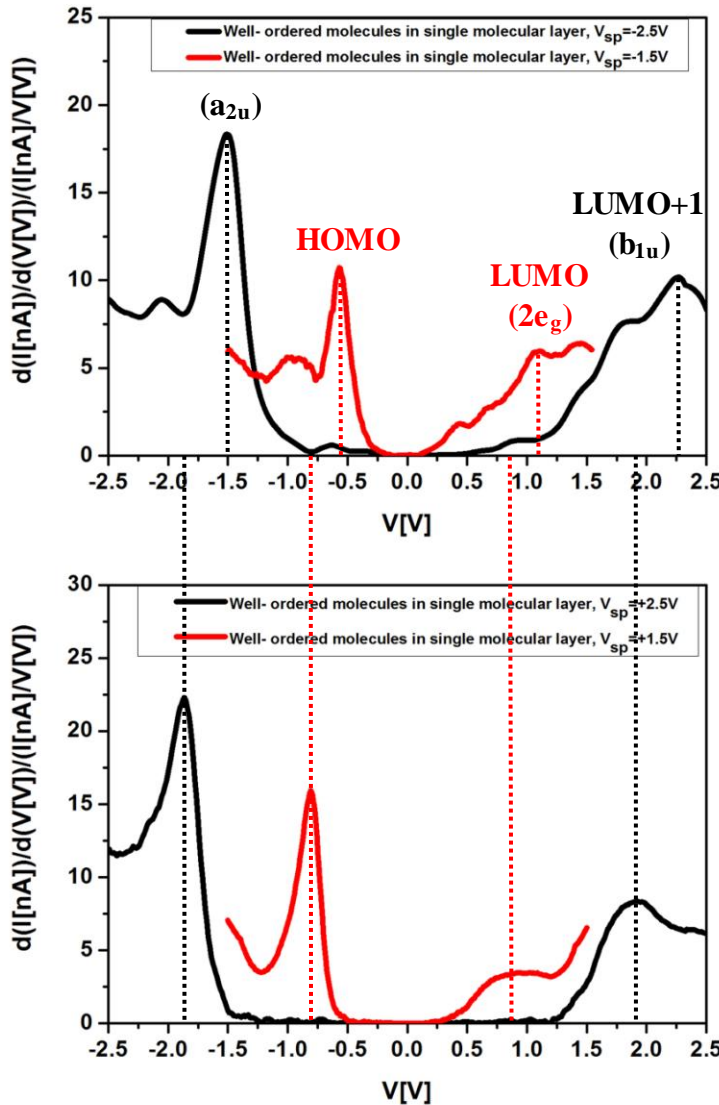


Figure 6.12 The NDC curves for the molecules in the well-ordered single FeTPP molecular network/graphene/ SiC (0001) at the negative ($V_{sp}=-1.5V$; $-2.5V$) and positive ($V_{sp}=+1.5V$; $+2.5V$) set-point bias voltages.

To study the electronic interactions between FeTPP molecules and graphene, the STS measurements were carried out. Figure 6.12 shows the NDC curves for the molecules in the well-ordered single molecular layer on graphene/ SiC (0001) at both positive

and negative set-point bias voltages. For the tip/ molecular layer/ graphene system, the electron tunneling conductance path is from the tip Fermi level to the molecular orbitals, and then to the graphene Fermi level or in the opposite direction. The molecular orbitals after adsorption dominate the STS features, known as orbital mediated tunneling spectroscopy (OMTS). For the molecules in the single-layer well-ordered molecular network, in Panel (a), when the set-point bias voltage is -2.5V, there are two resonance peaks at -1.51eV and +2.29eV. When the set-point bias voltage is decreased to -1.5V, the molecular resonance peaks are detected at -0.56eV and +1.08eV.

The electronic structure of free base tetraphenylporphyrin molecule (H_2TPP) in gas phase in the study by M. S. Liao showed the HOMO and LUMO of the outer porphyrin ring orbitals have the a_{2u} and $2e_g$ symmetries, respectively and the gap is 1.94eV. The Fe(II) in the FeTPP molecule is expected to have a d₆ configuration and it makes the outer-porphyrin ring (a_{2u}) orbital decreases 0.64eV and LUMO orbital ($2e_g$) increases 0.12eV than those in the H_2TPP molecule. In addition, the four occupied 3d-like orbitals b_{2g} (d_{xy}), a_{1g} (d_{z^2}) and $1e_g$ (d_{xz} and d_{yz}) all lie above the porphyrin a_{2u} orbital, in which, the b_{2g} is higher than a_{2u} orbital by 0.45eV. The d_{z^2} orbital and $d\pi$ (d_{xz} and d_{yz}) are weakly antibonding, and their energy levels are higher than the nonbonding d_{xy} orbital by 0.39eV and 0.49eV, respectively. Therefore, for the single FeTPP molecule in gas phase, the HOMO is mainly contributed by d_{z^2} orbital or $d\pi$ orbital, the LUMO shows the same symmetry with that of H_2TPP molecule ($2e_g$), which giving the HOMO-LUMO gap of 1.86eV. When the Fe(II)TPP molecule receive an electron, it would transform to $Fe(I)TPP^{-1}$, and the HOMO-LUMO gap of single $Fe(I)TPP^{-1}$ molecule in gas phase would shrink to 1.58eV[14].

Based on the DFT calculation, for the STS curves in Figure 6.12, when the set-point bias voltage is -1.5V, the detected occupied states at -0.56eV can be assigned to the

HOMO of the FeTPP molecules, the unoccupied resonance peak at +1.08eV is the LUMO ($2e_g$). The HOMO-LUMO gap measured in the STS (1.64eV) is a little bit narrower than the calculated FeTPP gap in the gas phase (1.86eV), and wider than the calculated Fe(I)TPP⁻¹ gap (1.58eV). This indicates that the electronic coupling between FeTPP molecules and graphene causes a little metallization of the molecules, in other words, the electronic coupling between FeTPP molecules and graphene is weak, whereas, there is a small charge transfer from n-doped graphene to the unoccupied states of FeTPP molecules.

The energy level alignment at metal-organic semiconductor interfaces have been reported[15, 16]. In the gas phase, the Fermi level of the organic molecules is arbitrary. After deposition on metal substrate, the charge neutrality level (CNL) represents an effective Fermi level of the organic molecules at the interface. If the organic CNL is higher than metal work function (ϕ_M), the electrons will be transferred from the organic molecules to the metal, which gives rise to an electrostatic dipole at the interface. This shifts the relative position of both the organic molecules and the metal substrate in the direction of aligning the organic molecular CNL and the metal Fermi level. The interface states caused by the hybridization of half-filled d_{z^2} Fe orbitals and metal states near the Fermi level was widely reported in the adsorption studies of Fe(II)Pc molecules on metal substrates[6, 17-21]. On graphene substrate, theoretical predication for Fe adsorption on graphene suggests a strong charge transfer with a strong variation of the electronic structure (both the filled and empty states) and with a reduction of the magnetic moment[14]. However, no hybridization between the Fe- d_{z^2} orbital and π states was detected in the adsorption study of Fe(II)Pc molecules on highly oriented pyrolytic graphite (HOPG). A weak van der Waals force between the FePc molecules and HOPG, and between the molecular layers were suggested [22]. In addition, a negligible electronic interaction between FePc molecules and graphene/Ir was also reported, with the charge transfer from FePc molecules to the graphene/Ir

Ir measured at 80meV[23]. The weak electronic coupling between FeTPP molecules and graphene/ SiC (0001) in this experiment is similar to the FePc on graphene/ Ir, however, the charge transfer direction is the opposite, because of the n-doping of graphene on SiC (0001).

In Figure 6.12, at a set-point bias voltage of -2.5V, the occupied and unoccupied molecular resonance peaks are at -1.51eV and +2.29eV, respectively. The measured gap in STS is 2.16eV wider than the gap at a set-point bias voltage of -1.5V. Both the shape of occupied and unoccupied resonance peaks are similar to those at the set-point bias voltage of -1.5V, implying the molecular resonance peaks measured at a bias voltage of -2.5V maybe caused by the shift of the molecular orbitals due to the different tip-sample separation, as discussed in Chapter 4. However, the molecular orbital shift caused by the molecular polarization in different tip-sample separation is within several tenths of a volt. In this experiment, the measured occupied resonance peak shifts 0.95eV and unoccupied resonance peak shifts 1.11eV, which are much larger than the molecular orbital shift caused by the molecular charging in the different tip-sample separation. Therefore, the peaks at a set-point bias voltage of -2.5V likely arise from the lower occupied state than HOMO and higher unoccupied state than LUMO. For the calculated isolated FeTPP molecular orbitals in gas phase by M.-S. Liao, the energy difference between the HOMO and the outer porphyrin ring orbital (a_{2u}) are 0.84eV. The energy difference between the LUMO ($2e_g$) and LUMO+1 (b_{1u}) is 1.03eV. The measured occupied and unoccupied peak shifts agree with the corresponding energy differences, confirming the measured molecular resonance peaks are a_{2u} and b_{1u} orbitals. Because the d-states in Fe(II)TPP are localized in the inner hole of tetraphenylporphyrin ring, while the π states are delocalized in the whole tetraphenylporphyrin ring. The d-states can be detected at a small tip-sample separation, while at high tip-sample separation, the delocalized π states are more prominent than the d states of Fe(II).

In Figure 6.12, for the NDC curves of the molecules in the well-ordered single molecular layer on graphene/ SiC (0001), when the positive set-point bias voltages were used, all the molecular resonance peaks shift to lower energy compared with the negative set-point bias voltages. Specifically, at a set-point bias voltage of +2.5V, the occupied and unoccupied molecular resonance peaks shift 0.36eV and 0.35eV, respectively to the lower energy compared to those at a set-point bias voltage of -2.5V. Comparing to the set-point bias voltage of -1.5V, the HOMO and LUMO molecular orbital peaks shift 0.24eV and 0.16eV, respectively to lower energy at a set-point bias voltage of +1.5V. For the positive and negative set-point bias voltages with the same value, the tip-sample separation are similar, as deduced from the Z-V curve shown in Figure 6.13. The difference is the voltage ramp direction. For the negative set-point bias voltage, the voltage ramp is from the negative potential to the positive, which is equivalent to moving from the ionized molecular level to the affinity energy level. For the negative bias voltage, the voltage ramps from positive to the negative, which is equivalent to moving from the affinity molecular level to the ionized molecular level. An experiment reported two molecular conformation states could be obtained by ramping the voltage from opposite directions during the spectroscopy measurement[24], but this seems different from our case, since no energy state jumps were observed in our NDC curve. The shift of occupied or unoccupied energy as a function of bias voltage is symmetrical and is lower for the lower set-point bias. This suggests that the electric field in the tunnel junction is important.

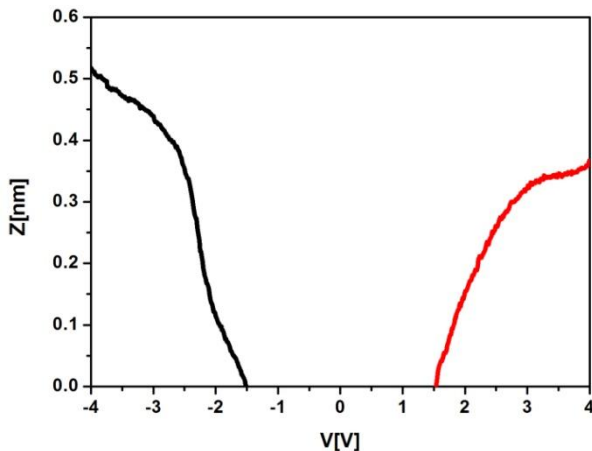


Figure 6.13 Z-V spectroscopy for the single layer FeTPP molecules/ graphene/ SiC (0001), $V_{sp}=\pm 1.5$ V, $I=0.15$ nA.

Figure 6.14 shows the NDC curves for the molecules in both well-ordered single molecular layer and double molecular layer on graphene/ SiC (0001) at a set-point bias voltage of -2.0V. For the molecules in the single molecular layer (red curve), the occupied and unoccupied molecular resonance peaks are at -0.87eV and +1.48eV. The resonance peaks shift to -0.96eV and +1.63eV, respectively, for the molecules in the double molecular layer (black curve). The gap is 0.24eV wider than that in the single molecular layer/ graphene/ SiC (0001). Previous studies of TCNQ molecular thin film on graphene[25, 26] and double-layer PtTPP(CO_2Me)₄ molecules on graphene in last chapter corroborated that the charge transfer only occurs at the molecule/ graphene interface. No charge transfer happens in the bulk molecular film. In this experiment, the wider occupied and unoccupied molecular energy gap for double layer molecular network on graphene also indicates that there is a charge transfer from graphene/SiC (0001) to FeTPP molecular layer, and the charge transfer mainly occurs at the FeTPP/graphene interface. For the double-layer molecular network on graphene/SiC (0001), the molecules in the top layer are less affected by the graphene.

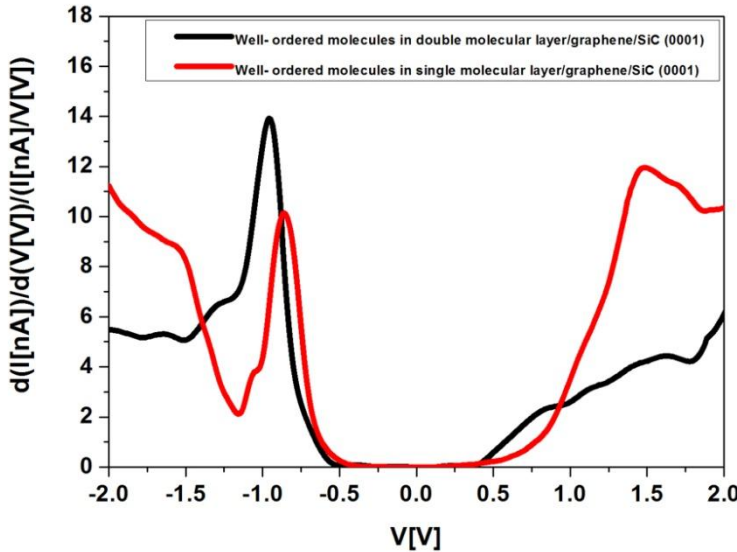


Figure 6.14 NDC curves for the molecules in both well-ordered single molecular layer and double molecular layer on graphene/ SiC (0001). Tunneling condition: $V_{sp}=-2.0\text{V}$, $I=0.15\text{nA}$.

Similar to the spectroscopy feature of the double layer molecular network on graphene/ SiC (0001), the energy gaps of the molecular aggregates on top of both single and double layer molecular networks are wider than the molecules in the well-ordered molecular network, as shown in Figure 6.15. In panel (a), at a set-point bias voltage of -2.5V, the detected molecular energy gap of the molecules in the well-ordered single molecular layer on graphene/ SiC (0001) is 3.75eV, the energy gap of the adsorbed molecular aggregates is 4.17eV. At the set-point bias voltage of -1.5V, the energy gap of the well-ordered single molecular layer is 1.65eV, the gap of the adsorbed molecular aggregates increases to 1.81eV. In Panel (b), The occupied and unoccupied peaks of the molecules in the well-ordered double molecular layer are -2.15eV and +2.6eV, while for the adsorbed molecular aggregates on top of the double molecular network, the peaks shift to -2.3V and +2.9V, respectively, giving rise to a wider energy gap.

The wider molecular energy gap for the adsorbed molecular aggregates compared to the well-ordered molecules can also be explained by the weak out-of plane

molecule-molecule interaction between the adsorbed molecules and molecules in the molecular network. There is small charge transfer from graphene to the adjacent molecular layer, whereas, the adsorbed molecules are less affected by the charge transfer.

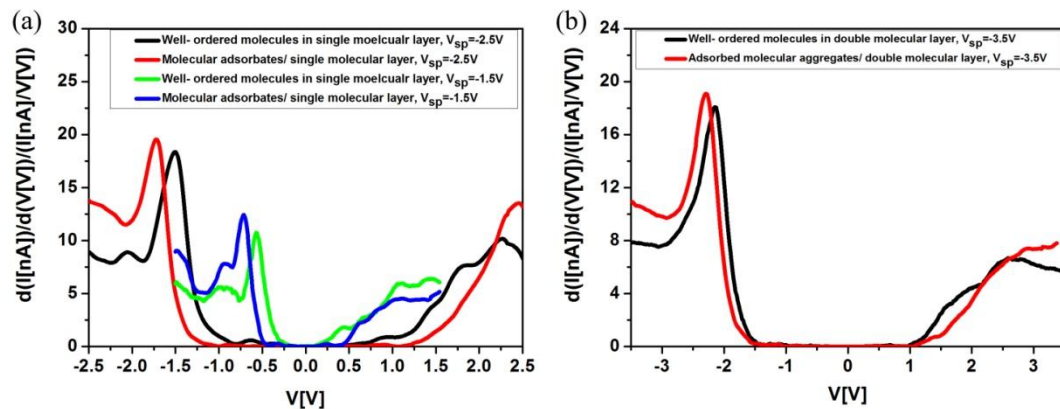


Figure 6.15 (a) NDC for the molecules in both the well-ordered single molecular layer and molecular aggregates on top of the single molecular network on graphene/ SiC (0001), tunneling condition: $V_{sp}=-2.5V$ and $V_{sp}=-1.5V$, $I=0.15nA$; (b) NDC for the molecules in both the well-ordered double molecular layer and molecular aggregates on top of the double-layer molecular network on graphene/ SiC (0001), tunneling condition: $V_{sp}=-3.5V$, $I=0.15nA$.

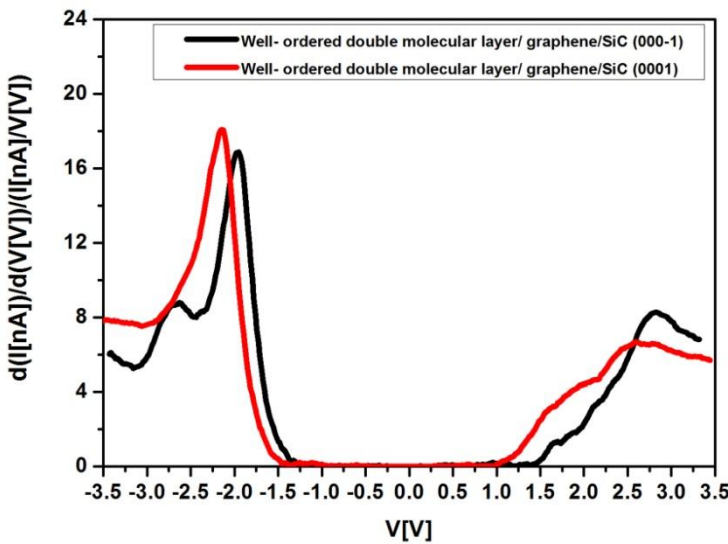


Figure 6.16 NDC curves for the well-ordered FeTPP molecules in double molecular network on both graphene/ SiC (0001) and graphene/ SiC (000-1). Tunneling condition: $V_{sp}=-3.5V$, $I=0.15nA$.

Figure 6.16 shows the NDC curves for the well-ordered FeTPP molecules in the double molecular network on both graphene/ SiC (0001) and graphene/ SiC (000-1). At the bias voltage of -3.5V, the outer porphyrin ring orbital (a_{1u}) and LUMO+1 (b_{1u}) molecular resonance peaks are detected. For the molecules on graphene/ SiC (000-1) (black curve), two resonance peaks are at -1.96eV and +2.82eV, respectively. For the molecules on graphene/ SiC (0001) (red curve), the occupied and unoccupied molecular resonance peaks shift 0.08eV and 0.24eV to the lower energy, respectively.

From the previous STS results in this experiment, it is deduced that the charge transfer direction is from graphene/ SiC (0001) to the single FeTPP molecular layer, and that the intermolecular interaction between molecular layers is due to the weak van der Waals force, the electronic properties on the top molecular layer would be less affected by the graphene. In other words, the charge transfer to the top molecular layer will be much smaller. In addition, the charge transfer from graphene to the FeTPP molecular layer on SiC (0001) should be higher than that on SiC

(000-1) substrate, because of the n-doping of the graphene. This is correlated to the lower energy level of LUMO molecular orbital for molecules/ graphene/ SiC (0001), and is in accordance with the experimental results shown in Figure 6.16, thus further confirming the charge transfer from graphene to the FeTPP molecular layer.

6.7 Conclusions

In this chapter, the FeTPP molecular topography and electronic properties were studied on both graphene/ SiC (0001) and graphene/ SiC (000-1). After the deposition of Fe(TPP)Cl molecules on graphene at 195°C, the Fe(TPP)Cl molecules transformed to FeTPP molecules due to the dissociation of the Cl atoms. In the same way as the NiPc and PtTPP molecules, FeTPP molecules also form a well-ordered near square lattice on graphene. The double molecular layers show an offset-face-to-face stacking mode, and the intermolecular interactions are dominated by the van der Waals force. The adsorbed four-molecular aggregates on top of the molecular network indicate that the in-plane molecule-molecule interaction is stronger than out-of-plane intermolecular interaction. In addition, the adsorbed four-molecular aggregates have a rotation angle of 50° with respect to the molecular lattice directions, due to the molecular polarization induced by the non-equivalent intermolecular interactions in the molecular aggregates and the molecular network.

The FeTPP molecules are adsorbed on graphene via the electrostatic interaction. The electronic interaction between FeTPP molecules and graphene is stronger than that of NiPc and PtTPP molecules with graphene. A charge transfer is suggested from graphene to the FeTPP molecules, and it mainly occurs at the FeTPP/ graphene interface.

6.8 Bibliography

- [1] Q. Z. Lu, Y. Lu and J. J. Wang. DFT Study of Iron Tetraphenylporphyrin Chloride and Iron Pentafluorophenylporphyrin ChlorideChin. . J. Chem. Phys., 19: 227-232 (2006).
- [2] J. P. Collman, T. N. Sorrell and B. M. Hoffman. Models for cytochrome P-450. J. Am. Chem. Soc., 97: 913-914 (1975).
- [3] C. D. Silva, K. Czarnecki and M. D. Ryan. Visible and resonance Raman spectra of low valent iron porphyrins. Inorg. Chim. Acta., 287: 21-26 (1999).
- [4] J. L. Hoard, G. H. Cohen and M. D. Glick. The Stereochemistry of the Coordination Group in an Iron(III) Derivative of Tetraphenylporphine. J. Am. Chem. Soc., 89: 1992-1996 (1967).
- [5] M. M. E.-. Nahass, H. S. Metwally, *et al.* Electrical conductivity and dielectric relaxation of bulk iron (III) chloride tetraphenylporphyrin. J. Mater. Chem., 133: 649-654 (2012).
- [6] A. F. Marijuan, G. Barandika, *et al.* Heterogeneous catalytic properties of unprecedented μ -O-[FeTCPP]2 dimers (H2TCPP= meso-tetra (4-carboxyphenyl) porphyrin): an unusual superhyperfine EPR structure. Dalton Trans., 44: 213-222 (2015).
- [7] S. Alvarez. A cartography of the van der Waals territories. Dalton Trans., 42: 8617-8636 (2013).
- [8] M. Ratner. A brief history of molecular electronics. Nature Nanotech., 8: 377-381 (2013).
- [9] C. A. Hunter and J. K. M. Sanders. The nature of π - π interactions. J. Am. Chem. Soc., 112: 5525-5534 (1990).
- [10] B. Q. Xu and N. J. Tao. Measurement of single-molecule resistance by repeated formation of molecular junctions. Science., 301: 1221 (2003).

- [11] S. E. Shaheen, D. S. Ginley and G. E. Jabbour. Organic-based photovoltaics: toward low-cost power generation. *MRS BULLETIN.*, 30 10-19 (2005).
- [12] C. Janiak. A critical account on stacking in metal complexes with aromatic nitrogen-containing ligands. *J. Chem. Soc., Dalton Trans.*, 3: 3885-3896 (2000).
- [13] B. Q. Xu, X. Y. Xiao, *et al.* Large gate modulation in the current of a room temperature single molecule transistor. *J. Am. Chem. Soc.*, 127: 2386-2387 (2005).
- [14] M. S. Liao and S. Scheiner. Electronic structure and bonding in metal porphyrins, metal= Fe, Co, Ni, Cu, Zn. *J. Chem. Phys.*, 117: 205-219 (2002).
- [15] A. J. Samuels and J. D. Carey. Molecular doping and band-gap opening of bilayer graphene. *ACS Nano.*, 7: 2790-2799 (2013).
- [16] Arramel, A. C. Gomez and B. J. v. Wees. Band gap opening of graphene by noncovalent π - π interaction with porphyrins. *Graphene.*, 2: 102-108 (2013).
- [17] A. Reina, X. T. Jia, *et al.* Large area, few-layer graphene films on arbitrary substrates by chemical vapor deposition. *Nano Lett.*, 9: 30-35 (2009).
- [18] A. Candini, S. Klyatskaya, *et al.* Graphene spintronic devices with molecular nanomagnets. *Nano Lett.*, 11: 2634-2639 (2011).
- [19] X. Y. Zhang, E. H. Huisman, *et al.* Supramolecular chemistry on graphene field-effect transistors. *Small.*, 10: 1735-1740 (2014).
- [20] M. G. Betti, P. Gargiani, *et al.* Formation of Hybrid Electronic States in FePc Chains Mediated by the Au(110) Surface. *J. Phys. Chem. C.*, 116: 8657-8663 (2012).
- [21] P. G. Collins and P. Avouris. Nanotubes for electronics. *Sci Am.*, 283: (2000).
- [22] S. C. Mathur and J. Singh. Molecular electronic structure of metal phthalocyanines *Int. J. Quantum Chem.*, 1: 57-82 (1972).
- [23] T. Akasaka and F. W. S. Nagase. Chemistry of nanocarbons. Wiley (2010).
- [24] X. H. Qiu, G. V. Nazin and W. Ho. Mechanisms of Reversible Conformational Transitions in a Single Molecule. *Phys. Rev. Lett.*, 93: 196806 (2004).

- [25] W. Chen, S. Chen, *et al.* Surface transfer p-type doping of epitaxial graphene. *J. Am. Chem. Soc.*, 129: 10418-10422 (2007).
- [26] C. Coletti, C. Riedl, *et al.* Charge neutrality and band-gap tuning of epitaxial graphene on SiC by molecular doping. *Phys. Rev. B.*, 81: 235401 (2010).

Conclusions and Perspectives

Graphene has extraordinary properties because of its linear band structure and zero band gap. However, the lack of a band gap hinders the implementation of graphene in electronics; tuning the band gap of graphene would enable a precise control of the charge carriers. One of the promising solutions is to manipulate graphene by organic molecular building blocks. The organic molecules with a metal ion (metal-porphyrin, metal-phthalocyanines) are potential candidates, because of their robust structure and their charge and spin properties can be tuned.

In this thesis, graphene was prepared by sublimating Si atoms from both Si and C-terminated SiC substrates in ultra-high vacuum. Three molecules were used in an effort to functionalize graphene: they are Ni-phthalocyanine (NiPc), Pt-tetraphenylporphyrin ($\text{PtTPP}(\text{CO}_2\text{Me})_4$) and Tetraphenyl-21*H*,23*H*-porphine iron(III) chloride ($\text{Fe}(\text{TPP})\text{Cl}$). All of these three molecules form a well-ordered near square lattice molecular network on graphene, the molecular lattice directions are dominated by the molecular symmetry, graphene terrace direction and graphene symmetry, while the molecular orientations within each molecular lattice depend on the molecule-molecule interactions. The electronic couplings between all of three molecules and graphene are via the electrostatic interactions, which gives rise to the capacitive molecular-layer/ graphene interfaces. For the filled d-state organometallic molecules (NiPc and PtTPP), the heavy metal ion (Pt) enhances the electronic coupling between molecules and substrate. The unfilled d-state organometallic molecules (FeTPP) bring the magnetic moment on graphene by non-covalent bonding, and the electronic coupling is stronger than that between filled-d state molecules and graphene.

For the future, more studies are required to better interpret the molecular orbitals and the electronic couplings between FeTPP molecules and graphene. Here, the DFT

calculations are expected to be conducted in the near future. In addition, the angle-resolved photoemission spectroscopy (ARPES) would be helpful to understand the energy level alignment at the molecule/ graphene interface. The magnetic measurements at the atomic scale based on Kondo effect is able to establish the link between magnetic and electronic properties of organic molecules on graphene. Moreover, new studies of the electronic properties of graphene functionalized with different metal-porphyrin or metal-phthalocyanine molecules in conjunction with Hallbas magnetic measurements in a prototype device configuration have potential to pave the way for the application of the organometallic molecules/graphene interface in the spintronic devices.

Titre : Propriétés Électroniques du Graphène Fonctionnalisé par des Assemblages Moléculaires Bidimensionnels

Mots clés : Propriétés électroniques, Graphène, Assemblages moléculaires bidimensionnels

Résumé : Le graphène a des propriétés électroniques et mécaniques extraordinaires en raison de sa structure de bande linéaire. Toutefois, l'absence d'une bande interdite limite l'utilisation du graphène dans les dispositifs électroniques. Ajuster la bande interdite de graphène permettrait un contrôle précis des porteurs de charge. Une solution prometteuse consiste à modifier le graphène par des briques élémentaires de molécules organiques. Les molécules organiques avec un ion métallique (métal-porphyrine et métal-phtalocyanine) sont des candidats potentiels en raison de leur structure robuste et de leurs propriétés de charge et de spin qui peuvent être modulées.

Dans cette thèse, le graphène a été préparé par la sublimation d'atomes de Si sur les faces de Si et de C- du substrat SiC. Trois molécules qui transportent l'information de spin différents ont été étudiés avec le STM. À travers des collaborateurs les calculs DFT, nous apportons des informations complémentaires.

La première molécule utilisée dans notre expérience est la phtalocyanine de Ni (NiPc). L'ion Ni²⁺ a une configuration d'électrons 3d₈ avec un état de spin de 0. La seconde molécule est la téraphénylporphyrine de Pt (PtTPP (CO₂Me)₄). L'ion Pt²⁺ montre également une configuration d'électrons 3d₈ à un état de spin de zéro. Cependant, l'atome Pt est plus lourd que celui du Ni. Promettant des effets spin orbite plus importants. La troisième molécule est téraphénylporphyrine de fer (III) chlorure (FeTPPCl). Le Fe³⁺ est dans l'état haut spin ($S = 5/2$).

Chacune de ces trois molécules forment un réseau moléculaire carré bien ordonné sur le graphène. Les directions de réseau moléculaires sont dominées par la symétrie du graphène, tandis que les orientations moléculaires dépendent des interactions intermoléculaires. Les couplages électroniques entre chaque molécules et le graphène sont transmis par les interactions électrostatiques, qui donne lieu à des interfaces capacitifs entre la couche moléculaire et graphene. Les interactions électroniques entre les molécules FeTPP et graphène sont plus fortes que celles entre PtTPP ou NiPc et le graphène. Les études des molécules organiques avec adsorbées sur le graphène des spins différents a le potentiel d'ouvrir la voie à l'application de l'interface organométallique molécules/graphène dans les dispositifs de spintronique.



Title: Electronic Properties of Graphene Functionalized with 2D Molecular Assemblies

Keywords: Electronic properties, Graphene, 2D molecular assemblies

Abstract: Graphene has extraordinary properties because of its linear band structure and zero band gap. However, the lack of a band gap hinders the implementation of graphene in electronics; tuning the band gap of graphene would enable a precise control of the charge carriers. One of the promising solutions is to modify graphene with organic molecular building blocks. Organic molecules with a metal ion (metal- porphyrin, metal-phthalocyanine) are potential candidates, because of their robust structure and the fact that their charge and spin properties can be tuned.

In this thesis, graphene was prepared by sublimating Si atoms from both Si and C-terminated SiC substrates. Three molecules which carry different spin information were studied by STM experiments. Through collaborations, DFT calculations were used to improve our understanding of the molecule-graphene interaction.

The first molecule used in our experiment is Ni- phthalocyanine (NiPc). The Ni^{2+} ion has a $3d^8$ electron configuration, giving a spin- state of 0. The second molecule is Pt-tetraphenylporphyrin ($\text{PtTPP}(\text{CO}_2\text{Me})_4$). The Pt^{2+} ion also shows a d^8 electron configuration with a spin state of zero. However, the Pt atom is heavier than Ni, which should increase the spin- orbit effects. The third molecule is tetraphenylporphyrin iron(III) chloride ($\text{Fe}(\text{TPP})\text{Cl}$). The Fe^{3+} in $\text{Fe}(\text{TPP})\text{Cl}$ is stable in the high spin state ($S=5/2$).

These three molecules each form well-ordered nearly square lattice molecular networks on graphene. The molecular lattice directions are dominated by the graphene symmetry, while the molecular orientations depend on the molecule- molecule interactions. The electronic couplings between each of three molecules and graphene are via the electrostatic interactions, which gives rise to the capacitive molecular layer/graphene interfaces. The electronic interactions between FeTPP molecules and graphene are stronger than those between PtTPP or NiPc molecules and graphene. The studies of the organic molecules with different spin information on the graphene has the potential to pave the way for the application of organometallic molecules/graphene interface in spintronic devices.

